MEASUREMENTS OF NEAR SURFACE OCEAN CURRENTS USING H F RADAR

A Dissertation
Presented to
The Academic Faculty

By

Kenneth Laws

In partial satisfaction
of the requirements of the degree of
Doctor of Philosophy in Physics

University of California
Santa Cruz
June 2001

UNIVERSITY of CALIFORNIA
SANTA CRUZ

MEASUREMENTS OF NEAR SURFACE OCEAN CURRENTS USING H F RADAR

A dissertation submitted in partial satisfaction of the
requirements for the degree of

DOCTOR OF PHILOSOPHY

in

PHYSICS

by

Kenneth Laws

June 2001

The dissertation of Kenneth Laws is approved:

Professor John F. Vesecky, Chair

Professor Stanley M. Flatte

Professor Frank G. Bridges

Professor Jeffery D. Paduan

Professor Daniel M. Fernandez

Vice Provost and Dean of Graduate Studies

Table of Contents

List of Figures

List of Tables

Abstract

Measurements of Near Surface Ocean Currents Using H F Radar

by

Kenneth Laws

High Frequency (HF) radar is unique both in its ability to probe the ocean currents within the top few meters below the surface and to provide synoptic current maps covering thousands of square kilometers.

This work focuses on the evaluation of ocean current measurement techniques, using the multi-frequency coastal radar (MCR), a system that operates on four frequencies (4.8, 6.8, 13.4 and 21.8 MHz) concurrently. Two methods of data processing, traditional beam forming and a direction finding approach, MUltiple SIgnal Characterization (MUSIC), are compared.

Simulations and comparisons using real data are used to evaluate the application of MUSIC to the MCR and to design modifications to improve its performance. Uncertainties in the radar measurements as a function of radar operating frequency, sea state parameters and data processing method are estimated. Results show MUSIC to be applicable to the MCR and to outperform beam forming, particularly for the lower frequencies, over most of the real and simulated experiments examined.

High resolution ocean wave spectral energy measurements are used to estimate the effect of Stokes drift on MCR measurements. The effect is shown to be small in magnitude relative to the expected errors in the MCR measurements and highly correlated with the wind.

Although results show a correlation between the MCR measurements and the expected Stokes drift effect, the correlations could be the result of wind stress-induced currents.

Using assumptions as to the form of the vertical current profile, estimates of the near-surface vertical shear are obtained from the MCR data. Analysis of the shear estimates casts doubt on the validity of a near-surface, logarithmic current profile for the open ocean. Further analysis of vertical shear estimates yields an estimate of the ocean current magnitude at the sea surface that is in agreement with the commonly accepted value of about 3 % of the wind speed.

Results of this work demonstrate a significant advantage to using MUSIC direction finding over conventional beam forming in limited aperture, multi-frequency radar applications and improve the MCR's shear measurement capability.

This work is dedicated to the principle of doing something simply because it is worth doing and the people in my life who have helped make it possible for me to do so: my grandfather Augie, my parents Dick and Julie and my wife Diane.

Acknowledgements

I would like to express my sincere appreciation to my committee members Professor Daniel M. Fernandez, Professor Jeffrey D. Paduan, Professor John F. Vesecky, Professor Stanley M. Flatte and Professor Frank G. Bridges. Professor Fernandez supervised my initial involvement in this project and provided invaluable guidance throughout. Professor Paduan contributed his oceanographic knowledge to the project and both he and Professor Fernandez provided financial support. I am indebted to Professor Vesecky for his enthusiastic support, guidance and funding provided through the University of Michigan.

I would like to thank both Dr. Calvin C. Teague and Dr. Donald E. Barrick for their generosity and willingness to share their extensive knowledge of HF radar throughout the work. I would also like to acknowledge Paul A. Fredrickson and the Boundary Layer studies Group at the Naval Postgraduate School in Monterey for providing data on wind and waves. I would also like to acknowledge Fred Bahr at the Monterey Bay Aquarium Research Institute for providing acoustic Doppler current profiler measurements.

Finally, I'd like to acknowledge my wonderful family, including my parents, Dick and Julie Laws, for their constant encouragement and support, my grandfather, Herbert (Augie) Augustadt, for his influence in sparking my interest in physics and engineering, my sister, Karen Laws Callaway, for her support and my wife, Diane Rose, for her constant love, and depth of patience, for bringing my life balance and the joy she carries within. And thanks to the waves themselves for both the natural laboratory and the diversion they provided.

This work was supported by the National Science Foundation through award number

9731704 to the Naval Postgraduate School and the Office of Naval Research through grant number N00014-97-1-0375, at the University of Michigan.

Chapter 1

Introduction, Objectives and Overview

1.1 Background of HF Radar

High Frequency (HF) radar ocean current systems (systems that operate in the HF band from 3 to 30 MHz) provide the ability to probe the near-surface ocean currents in the coastal region. The measurements provide synoptic current maps over a few to several thousand square kilometers of the ocean surface. The measurements are unique in their proximity to the surface and the extent of spatial coverage but the evaluation of the measurements is difficult because of the lack of relevant ground truth data for comparisons. In the work presented here we employ simulation methods to evaluate and compare data processing algorithms and estimate errors as a function of sea-state and radar operating parameters. We also examine comparisons of radar ocean current measurements from real data using different radar operating frequencies and processing methods and compare radar measurements to results obtained from an acoustic Doppler current profiler (ADCP).

HF radar systems use reflections of electromagnetic waves to probe the properties of the ocean surface. Although referred to by the term radar, they operate at much longer wavelengths than is typical for radar systems. The HF band wavelengths used by ocean radar systems typically range from 10 to 100 m. Through analysis of the Doppler spectrum, information can be extracted relating to:

- Near-surface currents
- Wind speed and direction
- Ocean wave directional spectrum
- Ship activity

The earliest recognition of resonant Bragg Scatter from the sea surface is attributed to Crombie (Crombie, 1955), while Barrick, Evans and Weber (Barrick et al., 1977) were among the first to exploit the phenomenon to sense oceanographic properties. A good general overview of HF radar systems and a selection of results in specific applications is found in the *Special Issue on High Frequency Radars for Coastal Oceanography* (The Oceanography Society, 1997).

Typically an HF radar system (including antennas, transmitter, receiver and control and data collection electronics) is installed at a site very near the coast. Such an installation makes measurements out to ranges of tens to a few hundred kilometers, depending on transmit power and frequency, using ground wave propagation. Since each radar installation measures only the radial component of the current, two sites, typically 20 to 30 km apart, are required to obtain vector currents. Typical parameters for HF, ground wave ocean radar systems are

summarized as follows:

- Radar operating frequency: 3 to 30 MHz
- Transmitted power: 12 to 25 W, average
- Radial range: typically 20 to 70 km depending on operating frequency, transmit power and sea state conditions, but ground wave radars operating in the lower region of the HF band can obtain ranges of 200 km or more.
- angular range: 90 degrees to a full 360 degrees depending on receive antenna geometry and data processing method.
- Antenna angular resolution: a few degrees to tens of degrees depending on receive antenna geometry and data processing method.
- Range resolution: dependent on pulse length for pulse range-gate radars. For the system used in the work described here, three kilometers is typical.
- Depth of current measurement: effectively a weighted average over depth that depends on the radar operating frequency used. Higher-frequency radars sample the current closer to the surface than lower-frequency radars. Effective depth of the measurement is generally within the top one or two meters below the surface.

Ocean radar systems have a long history of operation in Monterey Bay, and two different types of systems, the Multi-frequency Coastal Radar (MCR) and the SeaSonde, have been and are currently being deployed there. The present version of the MCR system, which

had its beginnings at Stanford in the early 1970s, was developed and built by a team from the University of Michigan, Stanford and ERIM International. MCR radar systems have been collecting data at Monterey Bay for over three years, starting in August, 1996, with a single-site deployment at Long Marine Lab in Santa Cruz. A second site was added in June, 1997 at Moss Landing Marine Lab in Moss Landing. The addition of the second site provided the ability to construct full vector current maps from the radial measurements obtained from each site. Deployment of a third MCR site at Granite Canyon Marine Lab took place in December, 1999 and further expanded the radar coverage area.

The SeaSonde is a commercial radar system and was designed and built by CODAR Ocean Systems of Los Altos, California. Three SeaSonde systems are currently deployed in Monterey Bay, located near the MCR sites at Moss Landing and Santa Cruz and at a third location at Point Pinos, near the Southern-most end of Monterey Bay. A fourth instrument was deployed in December, 1999 at Point Sur, which samples a region South of Monterey Bay in conjunction with the MCR at Granite Canyon. These instruments have compact, co-located antennas and operate on single frequencies near 12 and 25 MHz. A map of the Monterey Bay region showing the location of the radar sites, with the exception of the MCR site at Granite Canyon and the SeaSonde at Point Sur, is shown in Figure 1.1. Included in the figure is an example of a radial current map from the MCR system at Long Marine Laboratory and the locations of moorings in and near the radar coverage area. Also shown in the figure is the typical coverage area for each of the MCR systems. Where the regions overlap, excluding the region near the baseline connecting the two sites, full vector current measurements can be resolved.

Because of the antenna configuration and the data processing used, the SeaSonde system can resolve currents over the full 360° angular range. SeaSonde systems also have greater radial range because of higher average transmitted power. Typical coverage area for the SeaSonde systems is also shown for the system at point Pinos.

The Northern radar site located at Long Marine Laboratory is a good example of a desirable deployment site for an HF radar system. The transmit and receive elements for the MCR system are located at or near the edge of a small bluff overlooking Monterey Bay, about five meters above the ocean surface. The antennas are located very close to the shore and the site is relatively free of conductive structures, such as buildings or fences, in the near field that might distort the antenna patterns. The location of the antennas is shown in Figures 1.2 and 1.3. The quantity of radar systems, the combination of types of systems and the geometry of the deployment sites make Monterey Bay a powerful resource for analysis of HF radar system and algorithm performance and investigations into potential applications of the surface current measurements. Installations are part of the Innovative Coastal-Ocean Observing Network (ICON) program, which received funding from the National Oceanic Partnership Project (NOPP).

Of the types of information that can be extracted from the Doppler spectrum of the sea echo, near-surface ocean currents are the focus of this thesis. Most significant to the extraction of surface currents is the fact that the sea echo Doppler spectrum at HF is generally dominated by two very sharp peaks, shifted in frequency by about 0.5 Hz above and below the transmit frequency. It was deduced by Crombie (Crombie, 1955) that these peaks in the spectrum are due to Bragg scatter from ocean waves. If the radar system's antennas are effectively co-located

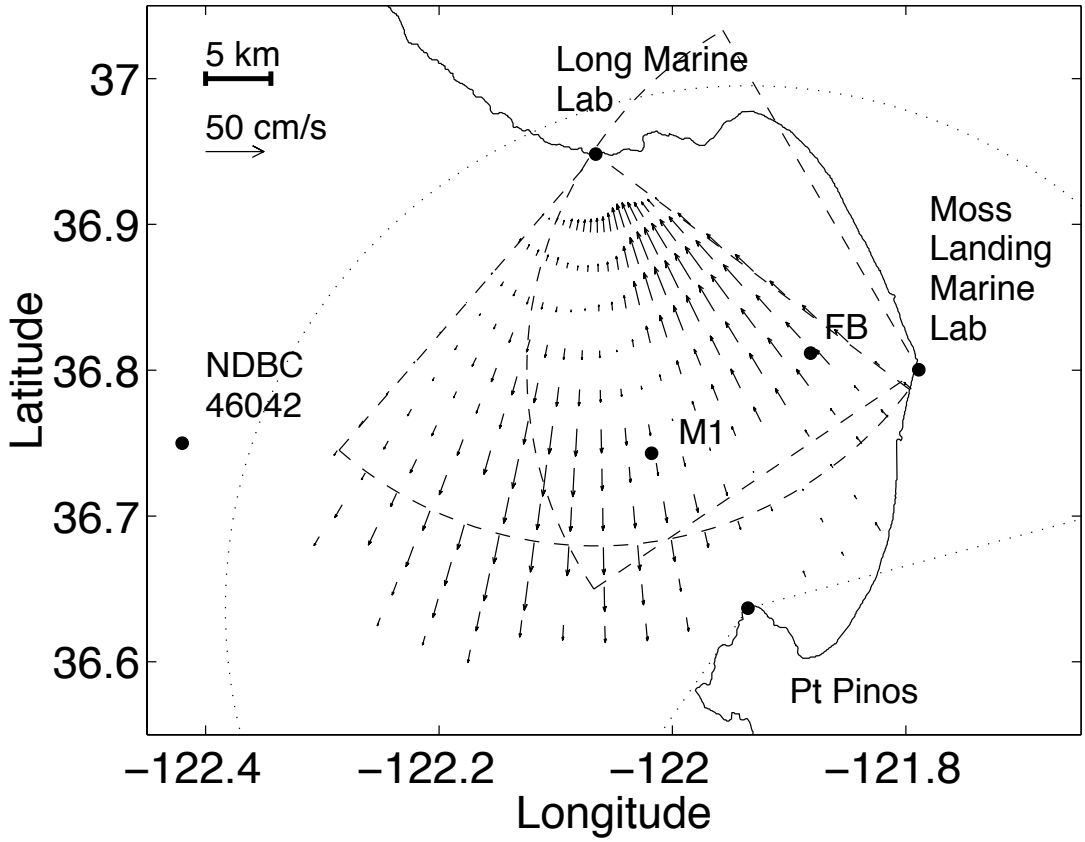

Figure 1.1: Area map of the Monterey Bay region showing locations of the HF radar sites and the mooring locations in and near the radar coverage area. The radar site locations are indicated by the solid circles along the shoreline at Long Marine Laboratory, Moss Landing and Point Pinos. The field of arrows is an example of a typical radial surface current map derived from data from the MCR at Long Marine Laboratory, on 15-Sep-1999 11:00 GMT, using an operating frequency of 21.8 MHz. The dashed lines show the typical coverage region for the two MCR sites at Long Marine Laboratory and Moss Landing. The dotted line shows typical coverage for the CODAR SeaSonde system at Point Pinos. There are both MCR and CODAR SeaSonde systems at Long Marine Laboratory and Moss Landing. At Point Pinos there is a SeaSonde system only.

Figure 1.2: Location of the MCR system antennas at the Long Marine Laboratory deployment site showing the low frequency transmit antenna in the foreground and four of the eight elements in the receive array directly behind. The high frequency transmit antenna is not clearly visible in the photo but was located on a small point of land, on the ocean side of the receive array and toward the north end of the array (toward the right side of the photo). Pelicans in flight appear for scale to the left of the low frequency transmit antenna. Data from this system was the primary source for experiments discussed in this thesis.

Figure 1.3: Loop elements of the MCR system's eight element receive array deployed at the Long Marine Laboratory site. The array pictured here is near the edge of a low bluff (about five meters above the sea surface) overlooking Monterey Bay.

(as is the case for the system deployments described in this work) then the Bragg resonant ocean waves are those having a wavelength of exactly half the radar wavelength and propagating directly toward and away from the radar. For the HF band, the corresponding wavelengths of the Bragg resonant ocean waves are 5 to 50 m. The range of Bragg resonant ocean wave frequencies is about 0.2 to 0.6 Hz, the period is roughly 2 to 6 seconds, and the phase speeds range from about 3 to 10 m/s. In many of the coastal marine environments where HF radar systems are deployed, these Bragg waves are propagating in all directions and have high enough amplitudes to result in a strong sea echo nearly continuously.

A typical sea echo spectrum is shown in Figure 1.4. In the figure a strong peak in the spectrum is seen at about positive 0.55 Hz. This peak is due to Bragg resonant waves propagating toward the radar. A weaker peak is barely visible above the noise at about -0.45 Hz and is due to Bragg resonant waves propagating away from the radar. The large ratio of the positive peak height to the negative peak height is indicative of a wind blowing toward the radar system generating larger wave heights propagating toward the radar than away from the radar.

The location of the Bragg peaks in the spectrum is determined by the phase speed of the resonant waves relative to the radar. The surface current measurement is made by estimating the difference between the measured frequency shift of the Bragg peaks and the expected Doppler shift due to the phase speed of the Bragg resonant wave traveling in still water. The still water phase speed of the Bragg resonant ocean waves, c_p, can be predicted by the dispersion relation for gravity waves on the ocean surface given by

$$c_p = \sqrt{\frac{2\pi g}{\lambda} \tanh(kH)} \tag{1.1}$$

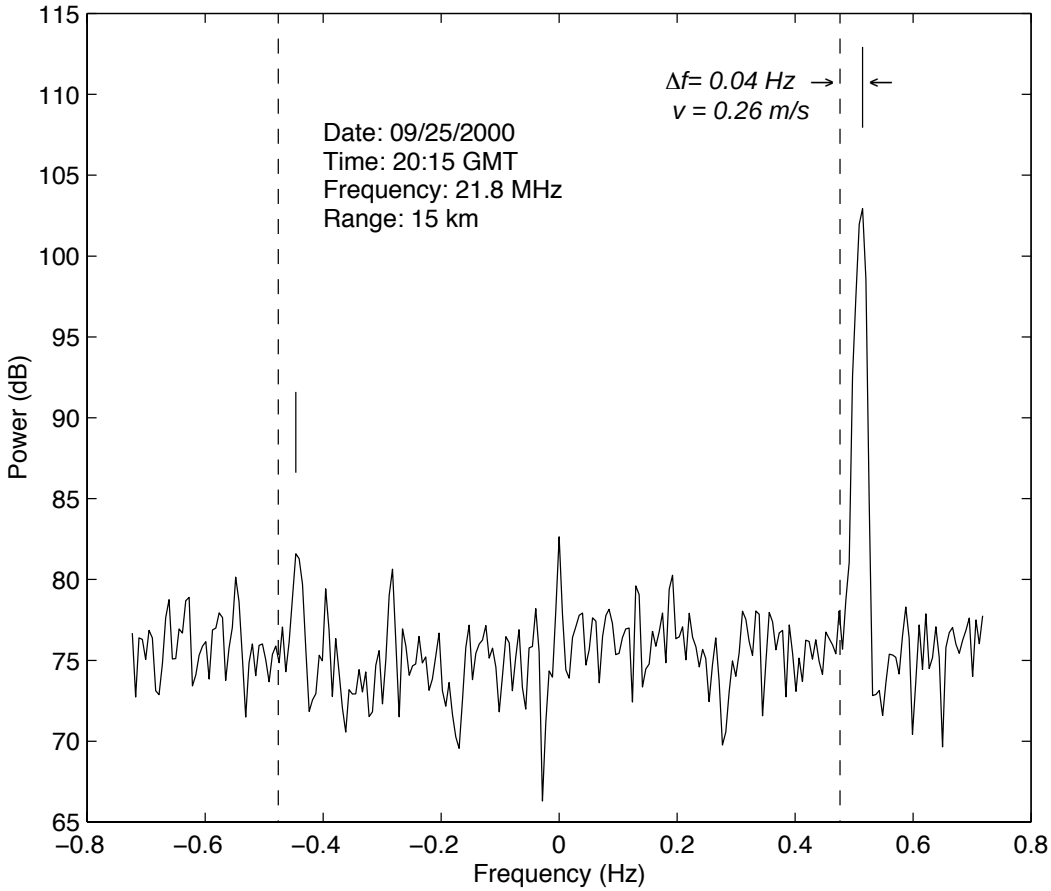

Figure 1.4: Typical sea echo spectrum at 21.8 MHz from the MCR system at Moss Landing. The prominent peak at approximately 0.5 Hz and the barely discernible peak at approximately -0.5 Hz are due to first order Bragg scatter. This example, collected at a range of 15 km from the radar, shows a signal-to-noise ratio of about 25 dB for the positively shifted Bragg peak. The frequency scale has been shifted so that the 21.8 MHz radar operating frequency corresponds to 0 Hz. The dashed lines at about $\pm.5$ Hz indicate the expected positions of the Bragg peaks in still water. The location of the peaks, estimated by a centroid calculation, is indicated by the solid vertical lines above each peak. The frequency shift of the positive Bragg peak from the expected still water value, Δf, and the corresponding radial surface current speed, v, are shown on the figure.

where λ is the wavelength of the ocean wave, g is the acceleration due to gravity k is the ocean wave wavenumber and H is the depth. For deep water, i.e., depths greater than about half the wavelength, as was the case for the experiments described here, $\tanh(kH) \approx 1$ and the phase speed is approximately independent of depth given by

$$c_p = \sqrt{\frac{g\lambda}{2\pi}}. \tag{1.2}$$

Since the wavelength of the Bragg resonant ocean waves is known to be half the radar wavelength, the still water phase speed of the waves and hence the expected Doppler shift of the Bragg peaks is known. Deviations from the expected Doppler shift can be attributed to the radial component of the surface current relative to the radar. This deviation in the expected Doppler shift is clearly visible in the sample spectrum shown in Figure 1.4.

If the transmit signal is strong enough and the sea state is high enough, which is often the case during strong winds or storms, a second set of broader peaks is visible in the spectrum. These second order peaks are due to multiple reflections from ocean waves and are typically 20 to 40 dB below the first order peaks in the spectrum. In the case of second order peaks, the sea echo is comprised of reflections from ocean waves of all wavelengths traveling in all directions. Details of the relationship between the second order region of the sea echo Doppler spectrum and the ocean wave directional spectrum have been worked out by Barrick (Barrick, 1972a) and (Barrick, 1972b). Methods of inversion to extract the ocean wave directional spectrum from the second order region of the sea echo have been described by Lipa (Lipa, 1978) and Wyatt (Wyatt, 1997).

The HF band is used for ocean radar systems because it allows for over the horizon

propagation and a suitable compromise between the advantages and disadvantages of higher and lower frequency operation. Operating at higher frequencies results in greater propagation loss and higher susceptibility to complications in spectral analysis due to higher order reflections. Operating at lower frequencies requires larger antennas and longer sampling times and results in lower spatial and temporal resolution. Under low wind conditions or over regions where there is limited fetch, weaker ocean echos are generally observed at lower frequencies due to lower energy in the corresponding region of the ocean wave spectrum.

In addition to the surface current information, the first order region can, in principle, be used to make measurements of the wind speed and direction. The measurement is based on the fact that the power in the Bragg peaks is proportional to the height squared of the Bragg waves. If the Bragg waves are in equilibrium with the local wind, the power in the Bragg peaks is determined by the wind speed. The ratio of the power in the approaching and receding Bragg peaks for a given radial radar look angle (usually determined by beam forming methods) is a function of the wind direction relative to the radar look angle. Investigations into wind mapping have been carried out by Fernandez (Fernandez, 1997) and others. The difference in the heights of the Bragg peaks in Figure 1.4 is an example of this effect. In this case the wind is directed toward the radar, resulting in the approaching Bragg peak being larger than the receding peak.

In addition to the oceanographic information contained in the sea echo, signals due to ships have been observed. Although HF radars are generally operated with a lower resolution than typical for surveillance radar systems, HF radars have excellent capability for monitoring ship activity in the coverage area.

1.2 Motivation

Ocean radar systems provide a unique capability to complement in-situ data sources in the coastal marine environment. The extent of the coverage area, the spatial resolution and the proximity of the measurement to the surface provide the ability to create near-surface current maps. These maps would be impossible to generate with any other methods currently available. These data provide valuable information for numerous practical applications, some of which are listed below:

- Environmental: two dimensional current vector maps can be used to predict the movement of contaminants, such as oil spills, and to coordinate containment operations.

- Sea rescue: current maps can be used to predict the movement of survivors adrift at sea and suggest directions to concentrate search and rescue operations. This can be extremely valuable at night, or in fog when visual search is very limited.

- Civil engineering: current maps can be used to estimate circulation patterns and thereby estimate the path of outflows and the holding time in bays and estuaries. Combined with wave information, current maps can help predict the stress due to currents and wave action on coastal and near-shore structures.

- Navigation: In situations where navigation is hazardous, such as in narrow channels or near hazardous reefs, current maps can help pilots compensate for strong currents, or avoid hazardous areas during times of high or variable currents.

- Ship detection: HF signals often carry signatures of ship echos and have potential for

monitoring coastal ship movement, in particular for evidence of illegal fishing activity.

- Oceanographic: Current maps can be used to estimate current fluxes at the mouths of rivers, bays, estuaries, etc. They can be used to identify areas of coastal upwelling and characterize circulations. Because of the proximity of the current measurement to the surface, HF radar data are useful in examining the dynamics of the air-sea interface. Further, the data show promise for assimilation with models which predict larger-scale circulation.

In addition to the wide range of applications for the data, HF radars have the advantage over in situ methods of being relatively inexpensive, e.g. there is no at sea deployment and recovery. The fact that they are shore-based makes them much easier to access for maintenance and repair and also enables them to be better protected from the damaging marine environment.

1.3 Objectives and Organization

Although HF radar has great potential for improving our ability to observe the coastal ocean environment, there is still much room for improvement in our understanding of the uncertainties and limitations of the measurements and the optimization of operating parameters and data processing algorithms. This work seeks to expand our understanding of both the limitations and the capabilities of HF radar systems. It focuses on:

- Comparison of two different data processing algorithms: direction finding and beam forming

- Improvement of a direction finding algorithm as applied to the MCR system
- Estimation of uncertainty in radar-derived surface current measurements
- Examination of the effect of wind stress on surface currents
- Examination of the effect of wave-induced currents (Stokes drift) on radar-derived surface current measurements.

The organization of this dissertation is as follows:

Chapter 1 gives an introduction to HF radar and in particular to the MCR radar system used to collect the data used in this work. It also lists the objectives and major contributions and describes the organization of the work.

Chapter 2 describes the properties of the ocean surface that are pertinent to HF radar and radar current measurements. It describes the first-order Bragg scatter process and the effect of the vertical profile of the horizontal near-surface current and non-linear wave interactions (i.e. Stokes drift) on the phase speed of deep water gravity waves.

Chapter 3 focuses on the experimental equipment and setup, expanding on the details of the MCR system and its design and configuration. The data available from moorings in or near the coverage area as well as the mooring instrumentation are also described.

Chapter 4 describes the simulation work that was done to evaluate and improve the adaptation of a direction finding algorithm, MUltiple SIgnal Characterization, (MUSIC) to the MCR system. The performance of conventional beam forming and MUSIC are compared using simulated data corresponding to the MCR system geometry. The performance of the two algorithms is evaluated as a function of sea state parameters such as horizontal current profile,

signal-to-noise ratio and wind direction and other sources of directional variation in radar cross section, for the four operating frequencies of the MCR system.

Chapter 5 compares radar-derived radial surface current measurements from the region near the Monterey Bay Aquarium Research Institute (MBARI) buoy, M1. Radar measurements are obtained using the MCR's four operating frequencies and processed using both beam forming and MUSIC algorithms. Measurements are compared both to each other and to the top bin of an ADCP located at the mooring. Results are used to compare current measurement performance as a function of operating frequency and data processing method and to roughly estimate the uncertainty in the radar-derived currents.

Chapter 6 examines the effects of wind stress and Stokes drift on the radar-derived radial surface current measurements from the region near a flux buoy deployed by the Naval Postgraduate School (NPS) in Monterey Bay. Wind measurements are obtained both from a propeller-vane anemometer and a three dimensional sonic anemometer located on the flux buoy. Wave measurements consist of high resolution, directional wave energy spectra obtained from the flux buoy motion sensors.

Chapter 7 summarizes the conclusions of this work and gives suggestions for further work.

1.4 Contributions

Major contributions of this work are listed below with the chapters involved:

- The first comprehensive comparison of beam forming and direction finding (MUSIC)

algorithms applied to HF radar data for the extraction of near-surface ocean currents (Chapters 4, 5, and 6)

- Improvement of the MUSIC algorithm for application to HF radar, particularly an objective method for suppressing erroneous currents (Chapter 4)

- Analysis of the relationship between model parameters describing the sea surface state and errors in estimation of currents from simulated data (Chapter 4)

- Estimation of errors in HF radar current measurements through inter-comparisons between currents measured using different radar operating frequencies and processing methods, and comparisons with ADCP current measurements (Chapter 5)

- Comparison between the predictions of a perturbation approach (Weber & Barrick, 1977) and an approach based on the formalism for Stokes drift in the estimation of corrections to the phase velocity of deep water gravity waves (Chapter 2)

- Estimation of the effect of Stokes drift on HF radar current measurements from numerical integrations of high resolution directional wave energy spectral measurements from a flux buoy located inside Monterey Bay (Chapters 6 and 2)

- Analysis of radar-derived ocean current measurements corresponding to different near-surface depths in order to estimate the shear and examine its relationship to wind and wave forcing (Chapter 6)

Chapter 2

Description of the Sea Surface State and its Effect on the Sea Echo at HF

2.1 Introduction

In this Chapter we briefly describe the scattering at HF of electromagnetic energy from the sea surface. We examine the effect of the vertical current profile on the Doppler shift of the Bragg peaks and the effect of wind on the directional dependence of the power in the sea echo. For this discussion we have assumed deep water relative to the wave height and wavelength, and small wave amplitude relative to wavelength. In the description of the dependence of the power in the sea echo as a function of position in the radar coverage region, we assume that the wind field is uniform and that equilibrium conditions exist. In the description of the effect of the vertical current profile we consider both wave-induced currents and currents due to

wind forcing. We describe how the effective depth of the radar measurement depends on both the vertical profile of the near-surface current and the radar operating frequency. Elements of the theory described here were used in the determination of the simulated sea echo in Chapter 4. The discussion of wave-induced currents focuses on the effect of Stokes drift (Stokes, 1847) and gives evidence that the effect is equivalent to a higher order correction to the dispersion relation for deep water gravity waves and that current measurements obtained using HF radar systems include the effect of Stokes drift. Examples of the expected effect of Stokes drift on the HF radar current measurements for an ideal wind-wave spectrum show that it is the higher frequency wave energy that dominates the Stokes drift effect. Investigation of the near-surface vertical current profile and its dependence on wind forcing and Stokes drift yields information concerning the depth of the HF radar current measurements. Conclusions of the discussion presented here are used to evaluate the results of the comparisons in Chapter 6 between wind and wave measurements and HF radar current measurements.

2.2 Bragg Scatter and the Dependence on Near-Surface Current and Wind

As mentioned in Chapter 1, the mechanism responsible for sea echo at HF was deduced (Crombie, 1955) to be Bragg scatter. If we assume that the receive and transmit antennas are in close enough proximity to each other to be considered co-located relative to the distance to the scattering patch, then the resonant scatterers are ocean waves propagating radially toward and away from the radar with a wavelength exactly half the radar wavelength. The sea sur-

face displacement, $\zeta(\mathbf{x}, t)$, can be described (Kenyon, 1969) by a Fourier series with random complex coefficients given by

$$\zeta(\mathbf{x}, t) = \sum_k \left[\eta_k e^{i(\mathbf{k}\cdot\mathbf{x} - \omega t)} + \eta_k^* e^{-i(\mathbf{k}\cdot\mathbf{x} - \omega t)} \right], \tag{2.1}$$

where $\mathbf{k}$ and $\mathbf{x}$ are the wavenumber and position vector, respectively, t is the time and η_k are the complex random Fourier amplitudes (η_k^* is the complex conjugate), which have the property

$$\langle \eta_{k_1} \eta_{k_2} \rangle = \langle \eta_{k_1} \eta_{k_2}^* \rangle = 0 \quad \text{for } \mathbf{k}_1 \neq \mathbf{k}_2, \tag{2.2}$$

where the angle brackets denote the ensemble average. It has been shown (Barrick & Snider, 1977) that the sea surface is best described by a Fourier series with random coefficients, that the Fourier coefficients are zero mean Gaussian random variables and that, to first order, the backscattered electric field can be expressed in terms of the complex random Fourier coefficients by

$$\mathcal{E} = \Lambda \eta_{\pm}(k_r) e^{[-i(\omega_r \mp \Delta\omega)t]}, \tag{2.3}$$

where Λ is a complex constant that depends on propagation loss to the scattering patch, the incidence angle to the antennas and other geometrical factors. The coefficients, $\eta_{\pm}(k_r)$, are the Fourier coefficients corresponding to the Bragg resonant waves propagating toward (+) and away (-) from the radar. The radian frequency, ω_r and the wave number k_r are that of the transmitted radar signal. The frequency shift of the backscatter, $\Delta\omega$, is given by the Doppler formula,

$$\Delta\omega = 2k_r c_p', \tag{2.4}$$

where c_p' is the phase speed of the Bragg waves relative to the radar. In general,

$$c_p' = c_p + \Delta v_{ph}, \tag{2.5}$$

where c_p is the still water phase speed of the Bragg waves and Δv_{ph} is a shift in the resonant waves phase velocity due to the motion of the water itself. This motion is the sum of the influences on the near-surface current, including geostrophic, wind-driven and wave-induced currents. The still water phase speed of the Bragg waves is determined by the dispersion relation for deep water gravity waves, given in terms of the ocean wave wavenumber, by

$$c_p = \sqrt{g/k}, \tag{2.6}$$

The shift in phase speed Δv_{ph}, has been shown by Stewart and Joy (Stewart & Joy, 1974) to be related to the horizontal current $\mathbf{U}(z)$ by

$$\Delta v_{ph} = 2k \int_{-\infty}^{0} U_x(z) e^{(2kz)} dz, \tag{2.7}$$

where $U_x(z)$ is the component of the horizontal current along the direction parallel to the propagation direction of the given wave train and z is the depth relative to the ocean surface, defined to be positive upward. From Equation 2.7, we see that the shift in the phase speed is a weighted average over depth of the horizontal current and that the weighting factor is determined by the wavenumber of the Bragg resonant wave. Since the radar operating frequency selects the wavenumber of the Bragg resonant waves, the depth of the radar current measurement is a function of the radar operating frequency used. It is precisely this property that makes near-surface current measurements over a range of depths possible with multi-frequency HF radar systems.

From Equation 2.3, we see that the average power in the sea echo is given by

$$P = \langle \mathcal{E}_{\pm} \mathcal{E}_{\pm}^{*} \rangle = \langle \Lambda \Lambda^{*} \eta_{\pm} \eta_{\pm}^{*} \rangle \,. \tag{2.8}$$

The power in the sea echo is therefore expected to be a function of whatever geometrical factors apply (e.g., antenna sensitivity patterns) and on the height of the Bragg resonant waves propagating parallel to the radar look angle. In general, the wave height of the Bragg resonant waves is a function of the position of the scattering patch within the radar coverage area, which is in turn, a function of the local wind speed, duration and fetch. The directional wind-wave spectra and the associated HF sea echo have been examined by (Tyler et al., 1974) and the experimental results show good agreement with the directional dependence of the HF sea echo power and the theoretical directional dependence of the wind-wave energy spectrum suggested by Longuet-Higgins, Cartwright and Smith (Longuet-Higgins et al., 1963) given by

$$g(\theta) = \alpha + (1 - \alpha) cos^{s}(\theta/2), \tag{2.9}$$

where the angle, θ, is defined relative to the mean wind and α is a small constant that accounts for wave energy propagating opposite the wind direction. The value of the exponent, s, is dependent on frequency, with a value ranging from near one at high frequencies to near ten for low frequencies.

2.3 Effect of Stokes Drift on the Phase Speed of Deep Water Gravity Waves

This section addresses the effect of non-linear wave interactions on the phase speed of the the Bragg resonant waves and the corresponding effect on current measurements. We examine this effect from the point of view that Stokes drift, a net transport of water that arises due to the fact that the path traced out by a parcel of water, influenced by the passage of a wave, is not closed but rather precesses, resulting in a net motion in the same direction as the propagation direction of the wave (Stokes, 1847), effectively generates a current that modifies the phase speed of the waves relative to a stationary observer. Since both the spatial and temporal averaging processes inherent in the HF radar measurements are large relative to the period and wavelength of the dominant waves, we expect an effect due to Stokes drift to be present in the data. The resulting shift of a wave's phase speed due to the Stokes drift generated by an arbitrary wave energy spectrum is in agreement with the expected shift in phase speed due to higher-order corrections to the dispersion relation calculated by Weber and Barrick (Weber & Barrick, 1977) from basic principles using a perturbation approach.

Weber and Barrick have shown that the first non-zero correction to the dispersion relation for deep water gravity waves arises in the third order hydrodynamic solution, obtained through perturbation analysis, for gravity waves on the ocean surface. They use the perturbation expansion of the radian frequency of a wave train, ω, given to second order by

$$\omega = \omega_0 + \omega_2, \tag{2.10}$$

(they show that $\omega_1 = 0$), along with the zeroth order dispersion relation given by

$$\omega = \sqrt{gk}, \tag{2.11}$$

to write the phase velocity of the wave train as

$$v_{ph}(\mathbf{k}) = \sqrt{\frac{g}{k}}\left(1 + \frac{\omega_2(\mathbf{k})}{\omega_0}\right). \tag{2.12}$$

They refer to the quantity $\omega_2(\mathbf{k})/\omega_0$ as the normalized correction to the phase velocity, Δv_{nph}. They state in a companion paper (Barrick & Weber, 1977) that it is clear that this correction is due to the presence of not only the wave itself but also the presence of all other waves.

In their derivation they simplify the equations of motion by assuming that the ocean is infinitely deep and unbounded on its surface and that the water is inviscid, incompressible, homogeneous and without surface tension. They also ignore the dynamics of energy transfer between the atmosphere and the ocean surface, between waves and due to viscous effects. They state that the solution is expected to be valid over spatial and temporal scales that are short relative to those over which energy transfer variations are important, but at the same time long relative to the wavelength and period of the dominant waves. In the case of the MCR system, sea echo spectra are collected over sampling times of about 12 minutes and the length scales relevant to the spatial resolution of the measurements are on the order of a few kilometers. Clearly the time and distance scales of HF radar measurements are much longer than the relevant wave periods of a few seconds and wavelengths of tens to hundreds of meters. HF radar measurement scales are also significantly shorter than the oceanographer's rule of thumb for changes in ocean wave conditions of half hour and 50 km. For example, Bowditch (Bowditch, 1982) gives

4.4 hours as the time for a 10 knot wind to raise 7 m waves (Bragg resonant at 21.8 MHz) of 2 feet significant wave height. Hence, we agree with Barrick (Barrick, 1986) that the perturbation estimates should be valid. Additionally, it is required for the validity of the perturbation approach that the slope of the surface of the waves is small, i.e.

$$\sum_{k,\omega} [\eta(\mathbf{k},\omega)] \cdot k < 1. \tag{2.13}$$

Barrick and Weber state that if the conditions on spatial and temporal scales are met, then the results of the perturbation analysis may be generalized to random surfaces and the sums may be converted to integrals (Barrick & Weber, 1977). Their result for the mean normalized correction to the phase velocity is given by

$$\left\langle \frac{\omega_2(k)}{\omega_0(k)} \right\rangle = \pm \frac{2k}{\omega_0} \int_0^k \omega_0' k' S_1(k') dk' \pm \frac{2k^2}{\omega_0} \int_k^\infty \omega_0' S_1(k') dk' \tag{2.14}$$

where $S_1(\mathbf{k})$ is the first order approximation to the wave height spectrum $S(\mathbf{k})$ defined in terms of the root-mean-square (rms) wave height, h, by

$$\int_{-\infty}^{\infty} \int_{-\infty}^{\infty} S(\mathbf{k}) d^2\mathbf{k} = \langle \zeta^2(\mathbf{r}, t) \rangle = h^2, \tag{2.15}$$

with $d^2\mathbf{k} = dk_x dk_y$. The actual correction to the phase velocity, Δv_{ph}, is related to the normalized correction to the phase velocity by

$$\Delta v_{ph} = \sqrt{\frac{g}{k}} \Delta v_{nph}. \tag{2.16}$$

Barrick points out (Barrick, 1986) that their result for the mean correction to the phase velocity (Barrick & Weber, 1977) (given here for convenience in Equation 2.14) is nearly identical to the Stokes drift equation, that their result arises from a third order calculation, that

the Stokes drift is also a third order calculation and that the predicted shift in phase velocity and the Stokes drift are one and the same. He also points out that since the spatial and temporal scales relevant to HF radar current measurements satisfy the conditions for the validity of the perturbation expansion, the predicted modification to the dispersion relation should be present in HF radar current measurements and that since the modification to the dispersion relation is a real current (Stokes drift), its inclusion is not an error in the measurement but rather a desirable inclusion of a real affect.

We now demonstrate that the current predicted due to Stokes drift from a given wave height spectrum can be used to calculate the correction to the phase velocity of gravity waves in deep water and that, for collinear waves, the resulting shift approaches the form Barrick and Weber obtained for the mean normalized correction to the phase velocity. We show that the results of the two approaches converge for the two regimes $k' > k$ and $k' < k$ where k is the wavenumber of the wave train whose phase speed is being considered and k' refers to the wavenumbers of all other waves present. For completeness we also follow Barrick and Weber (Barrick & Weber, 1977) to show that the results obtained here agree with the values predicted by two classical results: the increase in phase velocity for a single wave train due to self interaction, predicted by Stokes (Stokes, 1847) and, in the two regimes of k and k' mentioned above, with the correction to the phase velocity of a wave train due to the existence of a single parallel wave train, as predicted by Longuet-Higgins and Phillips (Longuet-Higgins & Phillips, 1962).

The shift in the phase velocity of a wave train due to the Stokes drift induced by the

presence of an arbitrary wave spectrum is derived as follows. We begin with the expression for the Stokes current as a function of depth arising due to a two dimensional ocean wave energy spectrum given by Kenyon (Kenyon, 1969) as

$$\mathbf{U}(z) = \frac{1}{\rho} \int \int_{-\infty}^{\infty} F(\mathbf{k}') \frac{\mathbf{k}'}{\omega(k')} \left[\frac{2k' \cosh[2k'(z+h)]}{\sinh(2k'h)} \right] d^2\mathbf{k}', \tag{2.17}$$

where ρ is the density of water, ω is the ocean wave radian frequency and the depth, z, is defined to be positive upward relative to the surface. The wave height spectrum, $F(\mathbf{k}')$, is defined by

$$\int \int_{-\infty}^{\infty} F(\mathbf{k}') d^2\mathbf{k}' = 2\rho g \sum_{k'} \langle \eta_{k'} \eta_{k'}^* \rangle = \rho g \langle \zeta^2(\mathbf{x}, t) \rangle. \tag{2.18}$$

Neglecting higher-order corrections to the phase velocity, assumed small compared with ${\omega_0}'$, we use $\omega(k') \approx \omega_0(k') = \sqrt{gk'}$ and, assuming that the deep water limit ($k'h >> 1$) is valid for all wavenumbers that contribute significantly to the integral, we simplify Equation 2.17 to obtain

$$\mathbf{U}(z) = \frac{2}{\rho g} \int \int_{-\infty}^{\infty} F(\mathbf{k}') \mathbf{k}' \omega(k') e^{2k'z} d^2\mathbf{k}'. \tag{2.19}$$

This is the general expression for the current as a function of depth due to the Stokes drift from an arbitrary two dimensional wave energy spectrum in deep water. Inserting 2.19 into the expression for the shift in the phase speed of a wave train due to the presence of a parallel current (Equation 2.7), we obtain

$$\Delta v_{ph}(k) = \frac{4k}{\rho g} \int_{-\infty}^{0} dz \int \int_{-\infty}^{\infty} F(\mathbf{k}')(\mathbf{k}' \cdot \hat{\mathbf{x}}) \omega(k') e^{(k+k')2z} d^2\mathbf{k}'. \tag{2.20}$$

Interchanging the order of integration, the integral over z can be evaluated giving the result

$$\Delta v_{ph}(k) = \frac{2k}{\rho g} \int \int_{-\infty}^{\infty} F(\mathbf{k}') \frac{\mathbf{k}' \cdot \hat{\mathbf{x}}}{k + k'} \omega(k') d^2\mathbf{k}'. \tag{2.21}$$

In the case of the unidirectional spectrum aligned with the x axis, the above simplifies to

$$\Delta v_{ph}(k) = \pm\frac{2k}{\rho g}\int_0^\infty F(k')\frac{k'}{k+k'}\omega(k')dk', \tag{2.22}$$

where the positive sign is used when the wave spectrum is aligned in the same direction as the wave of interest, and the negative sign is used when the spectrum is aligned in the opposite direction. In comparing the above to Barrick and Weber's result for the mean normalized phase velocity shift (Equation 2.14), we examine the two regimes, $k << k'$ and $k >> k'$. Keeping only the first term of the series expansion,

$$\frac{1}{k+k'} = \begin{cases} \frac{1}{k}\left[1 - \frac{k'}{k} + \left(\frac{k'}{k}\right)^2 - \cdots\right] & \text{for } k' < k \\ \frac{1}{k'}\left[1 - \frac{k}{k'} + \left(\frac{k}{k'}\right)^2 - \cdots\right] & \text{for } k' > k, \end{cases} \tag{2.23}$$

we find

$$\Delta v_{ph}(k) \approx \pm\frac{2}{\rho g}\int_0^{k-\epsilon} F(k')k'\omega(k')dk' \pm \frac{2k}{\rho g}\int_{k+\epsilon}^\infty F(k')\omega(k')dk', \tag{2.24}$$

where ϵ is an infinitesimal constant. Noting that the spectra $F(\mathbf{k})$, defined by 2.18, and $S(\mathbf{k})$, defined by 2.15, differ by a factor of ρg and that the conversion to normalized phase velocity shift involves multiplying Δv_{ph} by $\sqrt{k/g}$, we see that the integrands in 2.24 approach Barrick and Weber's result (Equation 2.14) in the two regimes.

We now follow the path of Barrick and Weber to show that the results obtained here give the expected phase velocity shift for two special cases: the phase velocity increase due to a finite amplitude wave train interacting with itself, predicted by Stokes (Stokes, 1847), and the shift in phase velocity of a wave train due to mutual interaction with a single other wave train traveling parallel to the first, predicted by Longuett-Higgins and Phillips (Longuet-Higgins & Phillips, 1962). The comparisons made here are basically equivalent to the comparisons made

by Barrick and Weber except that they compare results derived directly from the ocean wave heights and not from the spectrum of the wave heights. In other words, they do not use their expression for the mean normalized phase velocity shift, but rather apply their perturbation results directly. The equations used here involve the spectrum and, hence, imply averages over temporal and spatial scales. Hence, the results obtained here for the two special cases mentioned above are expressed in terms of mean square wave height. In that temporal and spatial scales for energy transfer are long compared with those implied by the spectrum it is assumed that the square wave height and mean square wave height are equivalent.

An expression for a first order wave height spectrum that combines both of the special cases is given by

$$F_1(\mathbf{k}) = 2\rho g \cdot [\langle|\eta_1(\mathbf{k}')|^2\rangle\delta(\mathbf{k}' - \mathbf{k}) + \langle|\eta_1(\mathbf{k}')|^2\rangle\delta(\mathbf{k}' - \mathbf{k}''), \tag{2.25}$$

where $\delta(x)$ is the Dirac-delta function. The subscript, 1, denotes the first order wave spectrum. The first term describes the finite amplitude of the wave itself and gives rise to the self interaction. The second term describes the amplitude of a single parallel wave train of wavenumber k'' and gives rise to the mutual interaction. Inserting this spectrum into 2.22 and evaluating the integrals gives

$$\Delta v_{ph}(k) = 2\omega(k)k\langle|\eta_1(k)|^2\rangle + 4\omega(k'')\frac{kk''}{k+k''}\langle|\eta_1(k'')|^2\rangle. \tag{2.26}$$

The first term (self interaction) is seen, by multiplying by the normalization factor $\sqrt{k/g}$, to be equal to the result of Stokes (Stokes, 1847) for the normalized increase in phase velocity due to self interaction of the wave train given by

$$\Delta v_{nph} = 2k^2|\eta_1(\mathbf{k})|^2. \tag{2.27}$$

The second term of 2.26 is seen, for $(k'' << k)$ and $(k'' >> k)$, to approach the results of Longuett-Higgins and Phillips (Longuet-Higgins & Phillips, 1962) for the shift in phase velocity of a wave train due to mutual interaction with a single parallel wave train given by

$$\Delta v_{ph} = \begin{cases} 4\omega(k'')k''|\eta_1(\mathbf{k}'')|^2 & \text{for } k'' < k \\ 4\omega(k'')k|\eta_1(\mathbf{k}'')|^2 & \text{for } k'' > k. \end{cases} \tag{2.28}$$

For $k \approx k''$, the second term of 2.26 is a factor of two smaller than that of Equation 2.28.

In summary, Barrick and Weber have shown that a correction to the dispersion relation arises in the third order perturbation solution to the equations of motion governing gravity waves on the ocean surface. They state that this correction is due to the presence of all waves on the ocean surface including the wave itself, and that this effect is equivalent to the Stokes drift. We have shown here that if the predicted current due to Stokes drift from all waves on the ocean surface, including the wave train whose phase speed is being examined, is assumed to affect the phase speed of the given wave train as predicted by the expression given by Stewart and Joy (Stewart & Joy, 1974) for an arbitrary current parallel to the wave propagation direction (Equation 2.7), then the resulting modification to the wave's phase speed is consistent with the results of Stokes for the increase in phase speed due to self interaction of a single wave train and approaches the results of Barrick and Weber and Longuett-Higgins and Phillips for the modification of a wave's phase speed due to mutual interaction with a single parallel wave train in the regimes where the wavenumber of the interacting wave is much larger or much smaller than the wave under consideration.

We have also shown that the results obtained here agree with those of Barrick and

Weber for the modification of a wave's phase speed due to non-linear wave interactions with an arbitrary spectrum, in the regimes where the wavenumbers of the waves responsible for the mutual interactions are very different from the wavenumber of the particular wave train being examined.

2.4 Vertical Profile of the Wind and Wave-Induced Currents

While HF radar has a great capability to provide measurements critical for examining the near-surface dynamics in the open ocean, the ability to interpret the radar data relies, in part, on assumptions about the form of the vertical profile of the near-surface currents, the very thing that we are interested in studying! HF radars sense the current by measuring the shift in the phase speed of the Bragg resonant waves. The magnitude of the shift depends on the weighted average over depth of the near-surface current. Therefore, the depth at which the shift is equal to the current, i.e. the effective depth of the measurement, depends on the form of the vertical profile of the horizontal current.

The exact form of the vertical current profile is unknown and is, in itself, a subject of great interest. The validation and evolution of theories for prediction of current profiles in the open ocean has been hampered due to the lack of data for experimental confirmation. This is due, in part, to the fact that the orbital velocities of the waves are generally much larger than the mean drift velocity in the near-surface region, making measurement of the near-surface drift very difficult. The most generally accepted assumption for the vertical profile of the current is

that it is logarithmic. The logarithmic current profile can be expressed by

$$\mathbf{U}(z) = \mathbf{U}_0 - \mathbf{u}_{*w} \cdot \frac{1}{K} \ln\left(\frac{z}{z_o}\right), \tag{2.29}$$

where $\mathbf{U}_0$ is the surface drift velocity, $\mathbf{u}_{*w}$ is the friction velocity of the water and $K \simeq 0.4$ is von Kármán's constant. The length scale describing the roughness of the lower side of the air-sea interface, z_0, is a subject of some controversy and will be discussed later in this section. Experiments in wind-wave tanks by Shemdin (Shemdin, 1972) and Wu (Wu, 1975), have shown good agreement with the logarithmic profile. Shemdin measured the surface drift velocity to be about 3 % of the wind speed and estimated the contribution of wave-induced surface drift, or Stokes drift, to be about one-tenth of the surface drift. He noted that fetch limitations may have been responsible for the small contribution of the wave-induced surface drift. An example of a wind dominated logarithmic current profile similar to Shemdin's result for a 9.1 m/s wind speed is shown in figure 2.1, Panel (a). The contribution due to wave-induced currents was estimated for the plot by calculating the Stokes current resulting from an ideal wind-wave spectrum corresponding to a wind speed of 9.1 m/s and then scaling it so that the current due to the Stokes drift at the surface was about one tenth of that predicted for the wind.

Wu's results are similar to Shemdin's but he found a linear region within a few millimeters of the surface. Wu's results also indicate that the contribution due to Stokes drift, in the fetch limited conditions of his wind-wave tank experiments, is small, about 5 to 13 % of the total surface current. Wu reported the wind-driven surface drift to be $U_w = 0.53u_{*a}$ and the total surface drift to be $U_0 = 0.55u_{*a}$, where u_{*a} is the magnitude of the friction velocity of the air. Wu suggested that, due to the growth of wind-waves with fetch and the resulting increase

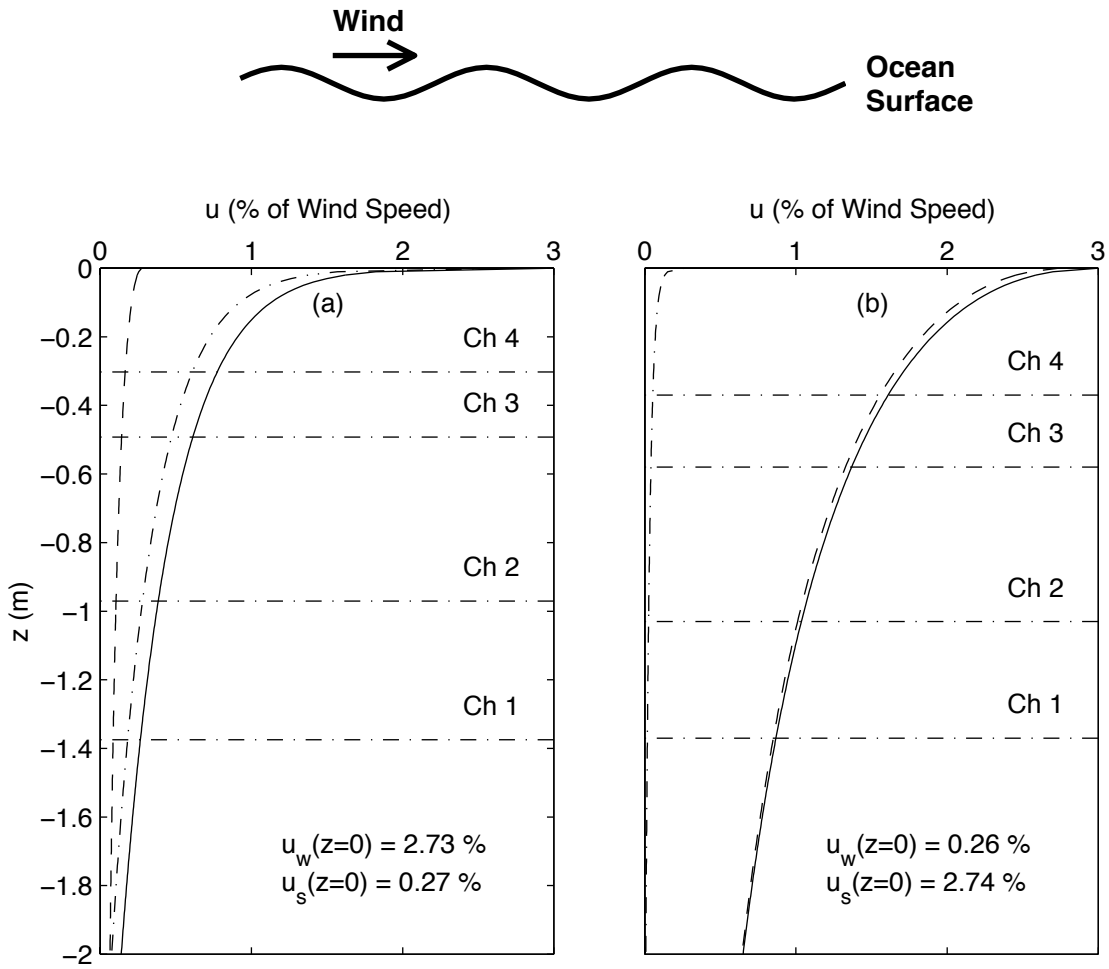

Figure 2.1: Examples of theoretical current profiles. Plot (a) shows a profile similar to those observed in wind-wave tank experiments, such as those of Wu (Wu, 1975) and Shemdin (Shemdin, 1972), dominated by wind-induced currents. Plot (b) shows a profile that might be expected for a case dominated by wave-induced currents, similar to that predicted by Kenyon (Kenyon, 1969) and Wu (Wu, 1983) for situations with effectively infinite fetch. The dashed line in the plots shows the wave-induced component, the dot-dashed line shows the wind-induced component and the solid line shows the total current. The horizontal dashed lines on the plots indicate the effective depths of the radar current measurement given the two profile assumptions, at the four radar operating frequencies, CH1(4.8 MHz), CH2(6.8 MHz), CH3(13.4 MHz) and CH4(21.8 MHz).

in the direct transfer of momentum from the wind to the waves and decrease in wind-induced shear, the ratio of the wind-induced surface drift to the wave-induced surface drift should decrease with increasing fetch, while the total surface current remains roughly constant at about 3.5 % of the wind speed. In a later paper (Wu, 1983), Wu estimated the wave-induced surface drift and the total surface drift, at very long fetches, to be about 2.7 % and 3.1 % of the wind speed, respectively. His results indicate a transition from the wind-induced dominated to wave-induced dominated surface drift for fetches of less than one km. This is in rough agreement with Kenyon (Kenyon, 1969) who concluded that for fully developed seas and a unidirectional spectrum, Stokes drift should account for a surface current of between 1.57 and 3.58 % of the wind speed, depending on the assumed form for the wind-wave spectrum. An example of a Stokes drift dominated current profile is shown in figure 2.1, Panel (b). The Stokes drift was calculated assuming an ideal wind-wave spectrum corresponding to a 9.1 m/s wind speed. The contribution of the wind-induced currents shown on the plot was estimated by assuming a logarithmic profile similar to that used in the wind-induced dominated case, shown in the same figure, scaled so that the sum of the wind-induced current and the Stokes drift at the surface is equal to the expected value of 3.1 % of the wind speed.

In later results, Wu (Wu, 1983) reported that, due to direct transfer of momentum from the wind to the waves, the wind stress is not continuous across the boundary, i.e. $\rho_w u_{*w}^2 < \rho_a u_{*a}^2$. This reduces the estimated size of u_{*w}. In the later results Wu gives a revised estimate of the total surface drift velocity as a function of wind friction velocity, $U_0 = 0.57 u_{*a}$. These later results are, however, based on wind-wave tank measurements and may not reflect the situation

in the open ocean.

In addition to the effect of Stokes drift, the influence of breaking waves on the near-surface current is thought to be an important factor leading to differences between current profiles measured in wind-wave tanks and current profiles expected in the open ocean. Experiments of Kitaigorodskii et al. (Kitaigorodskii et al., 1983) have indicated that a wave-affected layer of enhanced turbulence extends down to about ten times the wave amplitude. Craig and Banner (Craig & Banner, 1994) have employed techniques using a model to study the effect of breaking waves on vertical current profiles and energy dissipation below the surface and in the near-surface region. Their results indicate that within a near-surface layer dominated by wave-induced turbulence, the variation in current velocity is nearly linear and below the wave-enhanced layer, follows the standard logarithmic profile.

The roughness length z_0 is an important parameter in both the model used by Craig and Banner and the logarithmic profile. The appropriate value for the roughness length is a difficult quantity to estimate, requiring measurements of current velocity very close to the surface, and is therefore not well known. Charnock (Charnock, 1955) suggested, in analogy with the accepted form for the atmosphere, the formula

$$z_0 = \frac{au_*^2}{g}, \tag{2.30}$$

where a is a constant determined by experiment. Wu (Wu, 1975) obtained estimates of z_0 showing rough agreement with Charnock's relation, for wind speeds greater than 8 m/s, in that the data supported an increase in z_0 with wind speed. The values of z_0 Wu obtained in a laboratory tank ranged from 0.1 mm to about 1.2 mm for wind speeds from 8 to 14 m/s. The

open ocean model results of Craig and Banner (Craig & Banner, 1994) predict much larger values for z_0 due to wave breaking effects. Their results indicate that z_0 for the under side of the air sea interface may be much larger than that for above the interface and that z_0 may depend on the wave height or inverse wavenumber of the steepest waves and be similar in magnitude to the amplitude of the dominant waves. Using a model similar to that of Craig and Banner, Craig (Craig, 1996) made estimates of z_0 that do not support the dependence of z_0 on u_{*a}^2 but show that z_0 increases with both the wind friction velocity and the depth of the wave influence. He gives a rough estimate that z_0 may be about one-fifteenth of the wavelength of the dominant waves. He also found that, by choosing the appropriate value for z_0 in the logarithmic expression for the near-surface velocity, the full model solution and the logarithmic assumption are nearly indistinguishable. He gives as an example, for $u_{*w} = 0.0275$ m/s the result that the full model estimation of the current profile with the parameter $z_0 = 0.019$ m gives approximately the same prediction as a purely logarithmic profile with $z_0 = 0.059$ m. We note that the laboratory value obtained by Wu, $z_0 \approx 1$ mm, is far different from the open ocean predictions of Craig.

2.5 Vertical Profile of Stokes Drift Current Due to an Ideal Wind-Wave Spectrum and the Effect on HF Radar Current Measurements

We now examine an example of the effect of Stokes drift on the phase speed of deep water gravity waves, where we have assumed an ideal wind-wave spectrum, spread in direction by the function given in Equation 2.9. The purpose of this example is to acquire a feel for the magnitude of the Stokes current and the resulting shift in phase speed of a given wave in the presence of Stokes drift (which we will refer to as Stokes shift) that one might expect to measure for typical conditions observed during the course of the experiments discussed in Chapters 5 and 6, and to determine what frequencies of the ocean wave spectrum have the greatest influence on the Stokes shift.

Following Kenyon, we examine the idealized equilibrium wind-wave spectrum suggested by Pierson and Moskowitz (Pierson & Moskowitz, 1964). The spectrum has the form

$$f_n(\omega) = (\alpha_n \rho g^3/\omega^5) e^{-\beta_n (g/W\omega)^n}, \tag{2.31}$$

where

$$\begin{aligned} \alpha_n &= (f_o/2\pi)(2\pi\nu_o)^5 e^{5/n} \\ \beta_n &= (5/n)(2\pi\nu_o)^n \end{aligned} \tag{2.32}$$

and with values of the constants, $f_o = 2.75 \times 10^{-2}$ and $\nu_o = 0.140$. Pierson and Moskowitz examined spectra for $n = 2, 3, 4$ and found the value of $n = 4$ best fit their data. Kenyon

examined the Stokes drift for a unidirectional spectrum for the three values of n and showed that $n = 4$ gives the smallest Stokes drift for a given wind speed and $n = 2$ gives the largest. Kenyon plots the ideal wind-wave spectrum and the resulting Stokes current as a function of depth for $n = 2$, which can be worked out analytically. The method followed here is qualitatively similar to that of Kenyon, but here we retain the angular dependence of the spectrum. Using Kenyon's transformation (Kenyon, 1969)

$$kF(\mathbf{k}) = \left|\frac{d\omega}{dk}\right| f(\omega, \theta) \tag{2.33}$$

along with the substitution $\mathbf{k} = |k|\hat{\mathbf{k}}$ and the first order dispersion relation, the Stokes current from 2.19 can be written

$$\mathbf{U}^s(z) = \frac{2}{\rho g^2} \int_0^{2\pi} \hat{\mathbf{k}} d\theta \int_0^{\infty} f(\omega, \theta) \omega^3 e^{2\omega^2 z/g} d\omega, \tag{2.34}$$

where we have retained the angular dependence in $f(\omega, \theta)$. Using the substitutions, $f(\omega, \theta) = \rho g / 2\pi E(\nu, \theta)$ and $\omega = 2\pi\nu$, the expression becomes

$$\mathbf{U}^s(z) = \frac{16\pi^3}{g} \int_0^{2\pi} \hat{\mathbf{k}} d\theta \int_0^{\infty} E(\nu, \theta) \nu^3 e^{8\pi^2\nu^2 z/g} d\nu. \tag{2.35}$$

Noting that $\hat{\mathbf{k}} = \cos\theta\hat{\mathbf{x}} + \sin\theta\hat{\mathbf{y}}$ and orienting the x axis to lie parallel to the wind, the along-wind Stokes drift is given by

$$\mathbf{U}_x^s(z) = \frac{16\pi^3}{g} \int_0^{2\pi} \cos\theta d\theta \int_0^{\infty} E(\nu, \theta) \nu^3 e^{8\pi^2\nu^2 z/g} d\nu. \tag{2.36}$$

We evaluated this expression numerically for the ideal wind-wave energy spectrum given by

$$E(\nu, \theta) = (2\pi/\rho g) f_4(\omega, \theta) \cdot g(\theta), \tag{2.37}$$

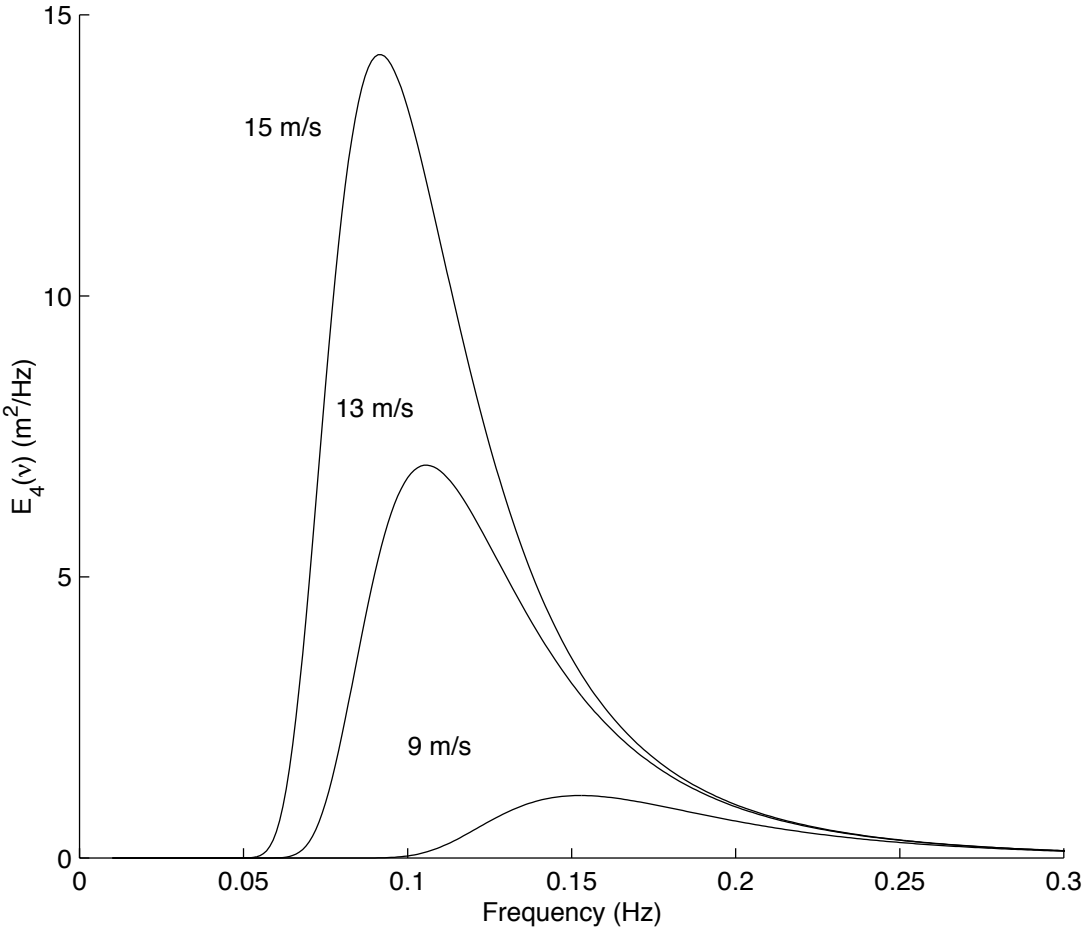

Figure 2.2: Theoretical (Pierson-Moskowitz) wind-wave energy spectrum for fully developed seas in equilibrium with 9, 13 and 15 m/s wind speeds.

where $g(\theta)$ is the spreading function given by Equation 2.9. Plots of the energy spectrum for wind speeds of 5, 10, and 15 m/s, evaluated for the along wind direction, $\theta = 0$, are shown in Figure 2.2 and plots of the Stokes currents corresponding to wind speeds of 9, 13 and 15 m/s are shown in Figure 2.3.

To investigate the relative contribution to the Stokes drift from each frequency component in the ocean wave spectrum, we repeated the numerical evaluation above, with a wind

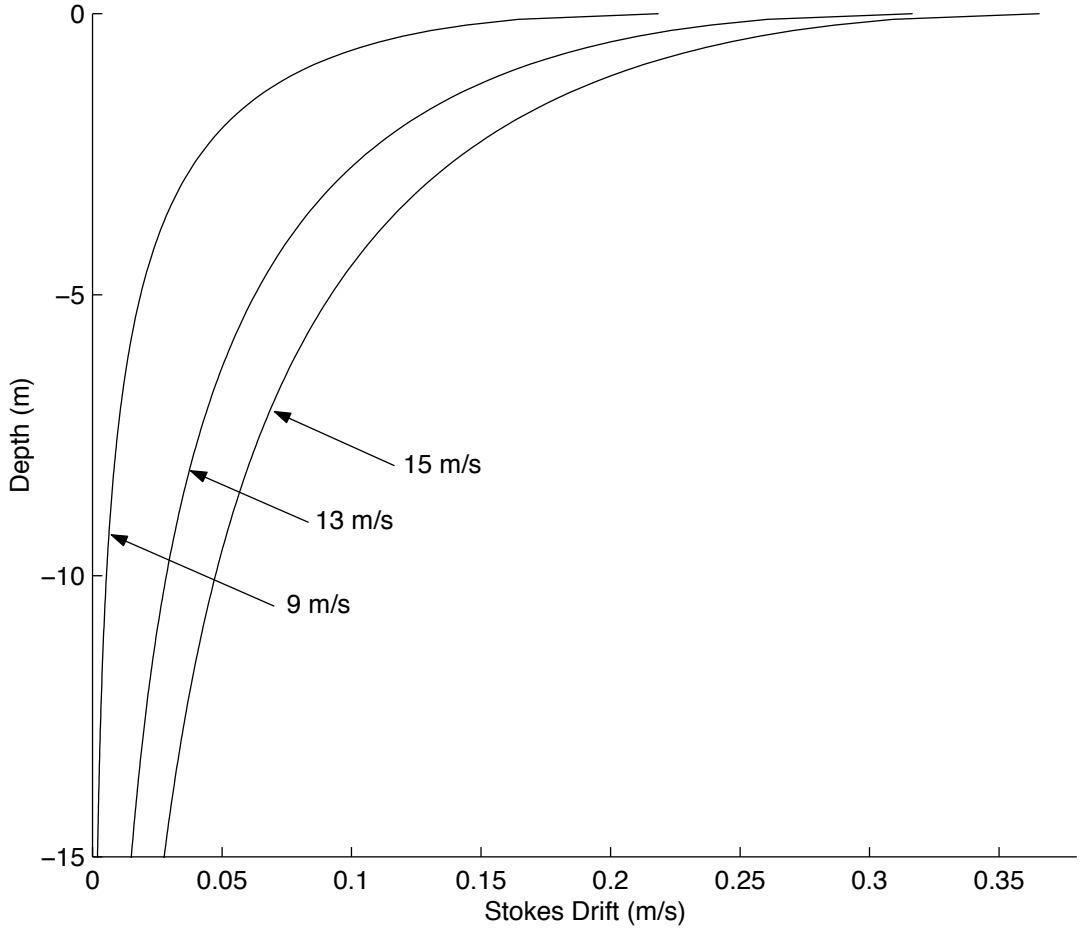

Figure 2.3: Plots of Stokes current as a function of depth for ideal wind-wave spectra corresponding to 9,13 and 15 m/s wind speeds.

speed of 15 m/s, but set the upper limit on the integral over ν to ν_c, where ν_c was varied from 0 to 0.5 Hz. The results are shown in Figure 2.4. It can be seen from the figure that the higher frequency waves account for the majority of the Stokes drift. The wind-wave spectrum used for this analysis peaks at less than 0.1 Hz and decays to half its peak value by about 0.15 Hz. However, the waves at frequencies below 0.15 Hz account for only about 60 % of the Stokes current at 2.0 m depth and only about 35 % of the current at the surface. As we will see in Chapter 6, the effect of wave energy at lower frequencies, such as that due to swell from distant storms, contributes little to the total Stokes drift current relative to the contribution due to wind-waves.

To compute the shift in a waves phase speed due to Stokes drift, Δv_{ph}^s, we insert 2.36 into 2.7, interchange the order of integration and evaluate the integral over z to find

$$\Delta v_{ph}^s(k) = \frac{16\pi^3 k}{g} \int_0^{2\pi} \cos\theta d\theta \int_0^{\infty} \left(\frac{\nu^3}{4\pi^2\nu^2/g + k} \right) E(\nu, \theta) d\nu. \tag{2.38}$$

We evaluated this expression numerically for the ideal wind-wave spectra given in Equation 2.37. The resulting phase velocity shift due to Stokes drift, as a function of wavenumber, is shown in Figure 2.5. The wavenumbers of the Bragg resonant waves corresponding to the MCR's four radar frequencies of operation are included in the figure.

2.6 Effect of Vertical Current Profile on the Depth of the Radar Measurement

It can be shown (Ha, 1979) that if the logarithmic form describes the current profile, then the HF radar current measurement, derived from the measured shift of the phase speed of

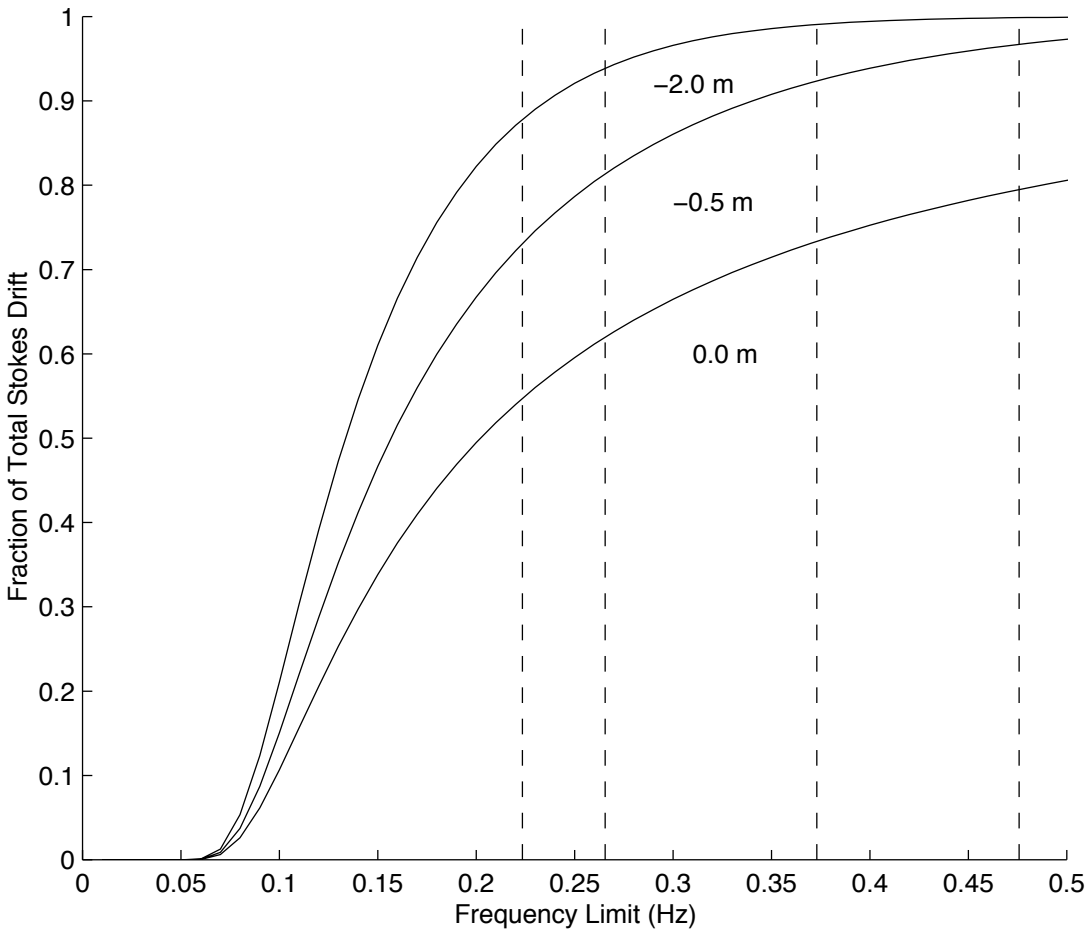

Figure 2.4: Fraction of total Stokes drift, computed by numerical integration, as a function of the upper frequency limit used in computation for 0, -0.5 and -2.0 m depths. The vertical lines on the plot at 0.223, 0.266, 0.372 and 0.476 Hz indicate, for reference, the frequencies of the Bragg resonant ocean waves corresponding to the four operating frequencies of the MCR system, from lowest to highest, respectively.

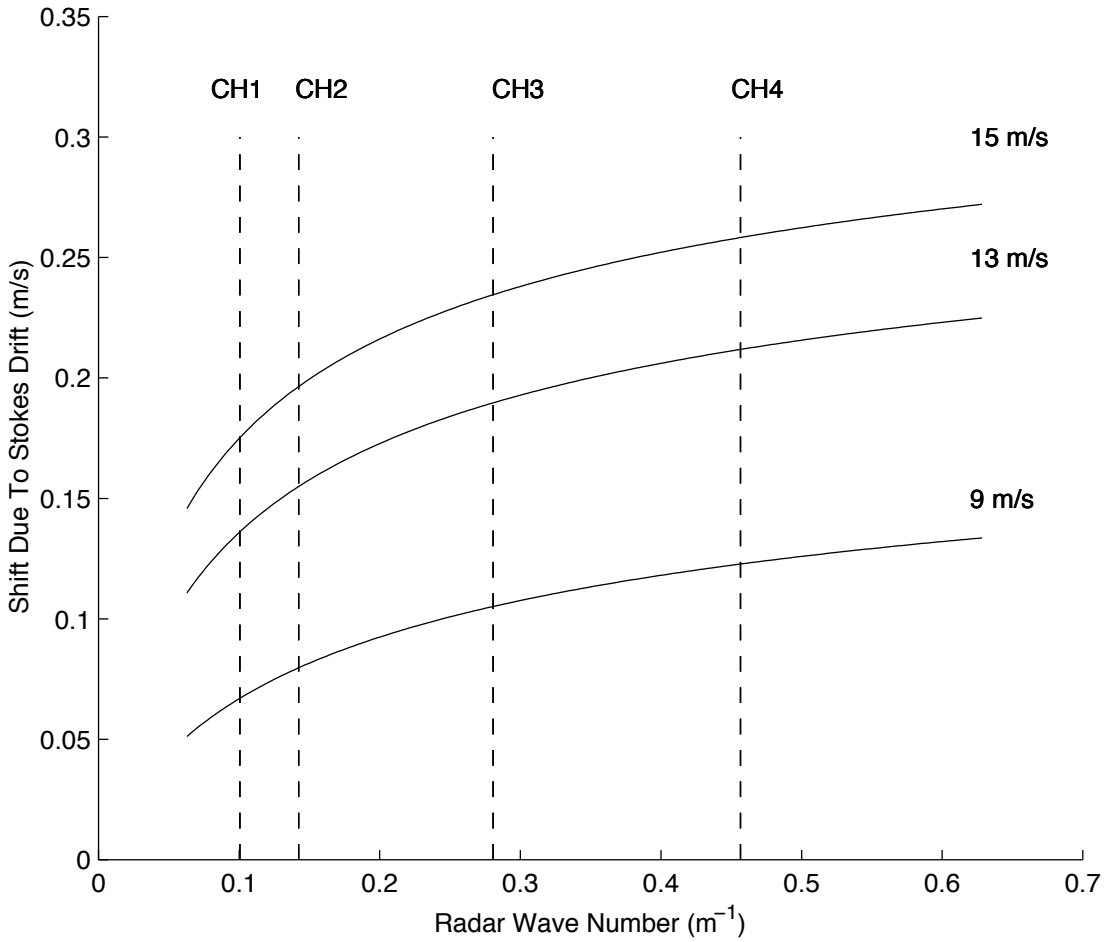

Figure 2.5: Shift in phase speed of Bragg resonant waves due to Stokes drift as a function of radar wave number for an ideal wind-wave spectrum corresponding to 9, 13 and 15 m/s wind speeds. The vertical dashed lines indicate the wave numbers corresponding to the four frequencies of operation for the MCR system: CH1(4.8 MHz), CH2(6.8 MHz), CH3(13.4 MHz) and CH4(21.8 MHz).

the resonant waves, is equal to the current at a depth of $z' = 0.045\lambda$, where λ is the wavelength of the ocean wave, or half the radar wavelength. If a linear profile, as suggested by Craig, is valid for the near-surface region, then the depth of the measurement can be shown (Fernandez, 1993) to be $z' = \lambda/4\pi$.

In the Stokes drift dominated case, the depth of the HF radar current measurement was estimated by setting the current as a function of depth, $U_x^s(z)$, given by Equation 2.36, equal to the shift in the Bragg resonant wave speed, $\Delta v_{ph}^s(k)$, given by Equation 2.38 and evaluating numerically to solve for the effective radar current measurement depth, $z'(k)$. The depth of the radar current measurement, as a function of radar wavelength over the HF band, is shown in figure 2.6 for the three current profile assumptions mentioned. In the case of the Stokes dominated profile, the depth is given for wind speeds of 9, 13, and 15 m/s, assuming the ideal wind-wave spectrum given in Equation 2.31 with the directional spreading function given by 2.9. As can be seen from the figure, the radar depths corresponding to the Stokes drift dominated case are between the depths corresponding to the linear and logarithmic profile cases for the range of wavelengths covered by the MCR's operating frequencies.

The depth of the current measurement in the Stokes drift dominated case, depends on the wind-wave spectrum and hence, on the wind speed. The deepest current measurement (at a given radar wavelength) corresponds to the largest wind speed and the greatest effect occurs for the longest radar wavelength. This is in contrast to both the linear and logarithmic profile assumption cases, where the depth of the current measurement depends only on the radar wavelength.

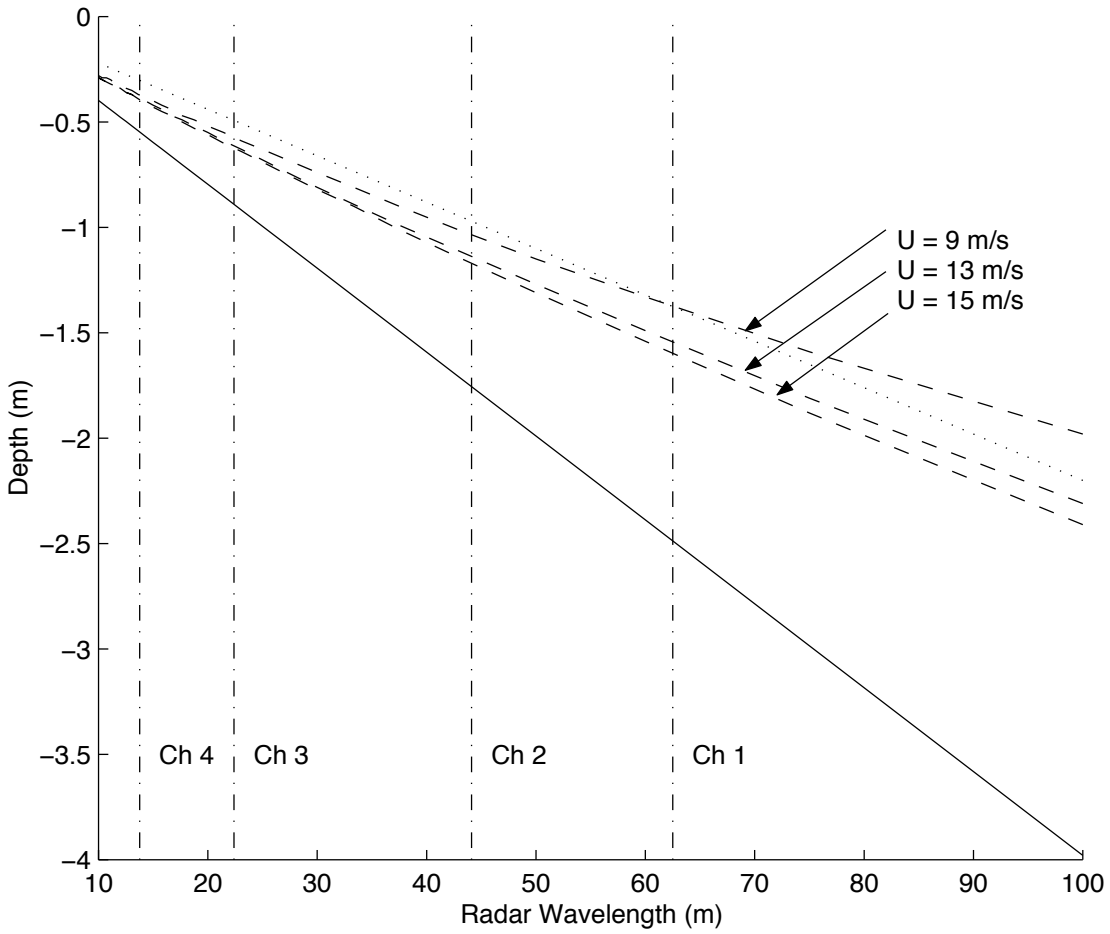

Figure 2.6: Plots of the effective depth of the HF radar current measurement as a function of radar wavelength over the HF band. Depths are shown for the linear (solid line), logarithmic (dotted) and Stokes drift (dashed) current profile assumptions. The vertical (dot-dash) lines indicate the wavelengths corresponding to the four frequencies of operation for the MCR system: CH1(4.8 MHz), CH2(6.8 MHz), CH3(13.4 MHz) and CH4(21.8 MHz).

Chapter 3

Experimental Setup

3.1 Radar System Description

The MCR system, described briefly in the previous chapter, and the interpretation of current measurements obtained from this system, is the focus of this thesis. The MCR system was used to collect the data used to generate the radar-derived ocean surface current measurements used in Chapters 5 and 6. The parameters used in generating the simulated data for the experiments described in Chapter 4 were modeled after this system. It has been used for numerous experiments at Monterey Bay, along the California coast (Ha, 1979), (Teague, 1986), (Fernandez, 1993) and elsewhere including deployments observing the Chesapeake outflow plume (COPE) (Teague et al., 2001) and fresh water experiments at Lake Michigan (Fernandez et al., 1999). It uses a pulse-range gate method for range resolution and operates on four frequencies in a pulse interleave mode so that measurements on the four frequencies are effectively simultaneous. The frequencies used for the work described here were 4.8, 6.8, 13.4 and 21.8 MHz. The

operating frequencies are generated using phase-locked loops and the same signals are used in the transmitter and receiver to ensure coherence. In-phase and quadrature signals are used to allow the separation of positive and negative frequencies in the Doppler spectrum, so that approaching and receding Bragg signals can be distinguished. The range resolution is determined by the width of the transmit pulse envelope, adjustable from 10 to 200μs. For the experiments discussed here, a 20 μs pulse width was used, corresponding to a 50 kHz bandwidth. The resulting range resolution was about 3 km. The first usable range bin was Range Bin two, centered approximately six kilometers from the radar.

The MCR system consists of the transmit and receive antennas, final stage transmit power amplifiers, a computer and a module rack containing the receiver, the transmitter, a digital signal generation and control unit and a power supply. A block diagram of the system is shown in Figure 3.1. The transmit and receive antennas located at the Long Marine Lab deployment site are shown in Figures 1.2 and 1.3 and the component rack and transmit amplifiers are shown in Figure 3.2.

3.1.1 Transmitter and Transmit Antennas

The transmitter is divided into high-band and low-band sections. For the experiments described here, the low-band section was operated at 4.8 and 6.8 MHz transmit frequencies and the high-band section was operated at 13.4 and 21.8 MHz frequencies. The power amplifier stage consists of two commercial wide-band amplifiers and produces a signal output power of about 50 W peak. Output power was recently increased to about 250 W peak by the addition of two Ameritron amplifiers, model ALS-600. The high-band and low-band amplifiers feed

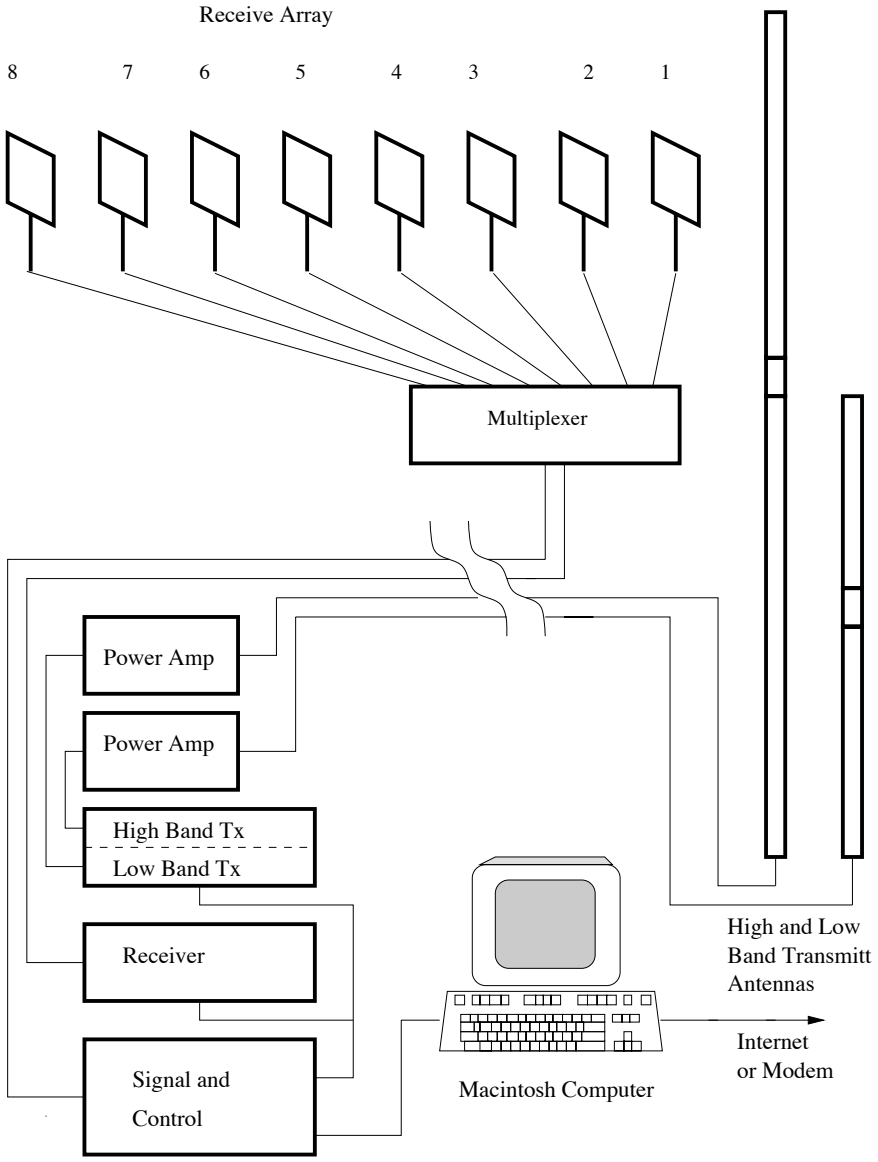

Figure 3.1: Block diagram of MCR ocean radar system. The high and low band antennas, the receive array and the multiplexer are generally located as close to the shore as possible and preferably where there are few conducting structures in the near field. The electronics rack containing the receiver, the transmitter and transmit power amplifiers, the control module and the power supply, along with the computer can be housed in a building or trailer located within roughly 100 m from the antennas. Remote access to the system via modem or internet connection greatly facilitates routine system checks and data retrieval for archiving and remote processing.

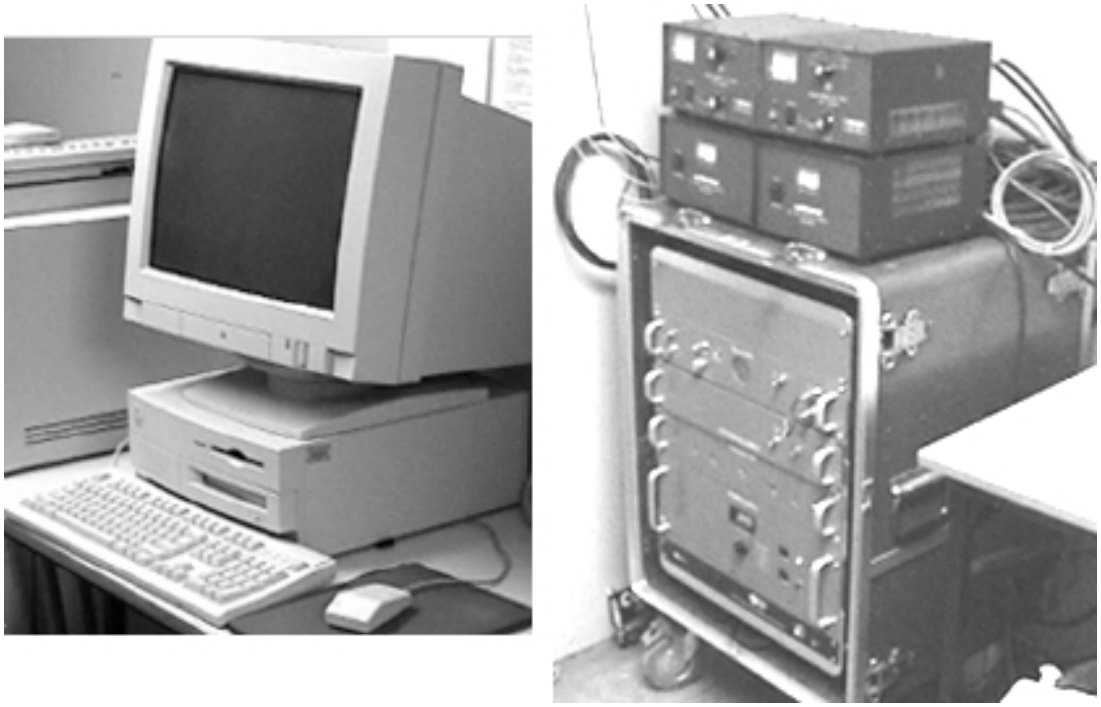

Figure 3.2: MCR system electronics (right photo) and computer for software control (left photo). The electronic hardware was developed and built by a team from the University of Michigan, Stanford, and ERIM International. The computer is a commercially available Macintosh 7200 and performs the functions of controlling the radar, data acquisition and storage and monitoring of system status.

separate half-wave vertical monopole antennas, each with a resonant filter located part way up the conducting element. The resonant filters, or traps, consist of a parallel resonant circuit tuned to the higher of the two radar frequencies for each antenna. Each trap presents a high impedance at the resonant frequency, thereby making the antenna effectively shorter at that frequency. At the lower frequency, the traps present a low impedance and the full length of each antenna conducts. The lengths of the antenna sections and the location of the traps are adjusted so that each antenna is resonant at two of the desired transmit frequencies. Ground plane conductivity was improved by laying 16 wires radially outward along the ground from the base of each transmit antenna.

3.1.2 Receiver and Receive Antennas

The receive antenna array consists of eight loop elements, spaced evenly, with inter-element separation equal to half the radar wavelength at 21.8 MHz (6.9 m). The loop elements are constructed of copper tubing and are supported at a height of about one meter above the ground by PVC pipe. A center support runs vertically from the top of the main support to the top of the loop element. This support is not part of the conductive element. Some of the loop elements in the array located at Long Marine Laboratory can be seen in Figure 1.3. The receive array is generally set up so that the axis of the array is oriented approximately parallel to the coast, and the plane defined by each of the loops is perpendicular to the sea surface and to the axis of the array. Thus, the maximum of each elements ideal sensitivity pattern (cosine pattern) is directed perpendicular to the array axis, i.e. parallel to the antenna array's broadside direction.

Each of the loop antennas is equipped with a separate pre-amplifier located inside the antenna housing. To avoid overdriving the pre-amplifiers, a blanking pulse is used to disable them for the duration of the transmit pulse. The signals from the pre-amplifiers are fed into a multiplexer and from there fed by a single coaxial cable to the receiver. The multiplexer is housed in a weather resistant enclosure and is located near the receive array. The two transmit cables, the multiplexer control cable and a cable carrying both the receive signal and multiplexer D.C. power connect the antennas to the transceiver which is usually located in a nearby building or trailer.

3.1.3 Operation and Data Processing

Data were collected once per hour at each of the sites. To produce an hourly data file, each radar system was active for approximately 12 minutes. The rest of the time the systems remained idle, except for a small fraction of the time used to transfer data to a remote computer for archiving and processing. The active periods for the radar systems at Long Marine Laboratory and Moss Landing Marine Laboratory were staggered to avoid interference. At the Long Marine Laboratory site, a CODAR SeaSonde radar system operating at a frequency close to one of the MCR frequencies was located in fairly close proximity. The SeaSonde was disabled during the active cycle of the MCR to avoid interference. System control and data acquisition and storage were accomplished using a Macintosh computer. An internet connection facilitated access for system status monitoring and the transfer of data to a remote computer for data archiving and processing, greatly reducing the need to physically access the site.

3.1.4 Site Locations

The deployment sites for the two MCR systems at Monterey Bay were Long Marine Lab in Santa Cruz, located at the northern end of the bay, and Moss Landing Marine Lab in Moss Landing, located near the eastern most point on the bay. The locations are shown in Figure 1.1. At Long Marine Lab, the antennas were located near the edge of a small cliff, about 5 m above sea level. The direction perpendicular to the receive array axis, or broadside direction, was 174 degrees true north. At the Moss Landing site, the antennas were located on low dunes, a few meters beyond the high water mark. The broadside direction at the Moss Landing site was about 283 degrees.

The uncertainty in full vector current measurements obtained by combining radial measurements from two sites is minimized when the radial directions of the two sites are orthoganal and increases as the angle between the radial directions become parallel. Where the radial directions are parallel (the baseline between radar systems) the full vector can no longer be resolved, but if signal levels from points along the baseline are sufficiently strong, comparison of the current measurements obtained can provide a consistency check between radar systems (Melton, 1995). In the configuration used at Monterey bay, the baseline between the two MCR systems coincided with a large steering angle for the Long Marine Lab system. Problems at large steering angles with the directivity of the antenna array, compounded by reduced sensitivity of the loop elements, make such measurements questionable in terms of their accuracy. For this reason, baseline measurements from the MCR systems at Monterey Bay were not considered useful for system evaluation. However, because the broadside directions of the two

systems were nearly perpendicular, the region for which the signals are strongest (near broadside direction) was also the region where the errors in combining radials to form full vector measurements are minimized (radial directions are near perpendicular). This makes the geometry of the systems at Monterey Bay nearly ideal for full vector coverage obtained using two radar systems. Unfortunately, due to equipment problems during the period of interest, sufficient data to generate full vector current measurements for the regions of interest were obtained a very small fraction of the time.

3.1.5 Calibration

The directional accuracy of radar system depends on the knowledge of the phase and amplitude characteristics of the receive antenna array components, including the individual loop elements, the pre-amps and the interconnecting cables. In terms of amplitude characteristics, a simple normalization was employed to compensate for gain variations in the individual antenna pre-amps. To determine the phase characteristics, a calibration procedure was performed at both of the Monterey Bay deployments. A transponder carried aboard a small boat was used to provide the calibration signal. Two methods of phase calibration were used. The first involved positioning the boat at a series of points covering as great a range of angles as the coastline allowed, and at an approximately constant range of roughly 1.5 km. Combined sea echo and transponder signal were then recorded while the boat remained approximately stationary at each of the points. The second calibration method involved driving the boat continuously at a low speed in an arc centered about the radar's receive array while the radar system continuously recorded time series data of the combined sea echo and transponder signal. A boat speed of

about 8 km/hr and a constant range of approximately 1.5 km was maintained during the course of the arc. It was found that a 64 point spectrum was sufficient to locate the position of the transponder peak in the data. Using this sample size, the time duration for a single spectrum was about 30 seconds. The change in angular position of the boat during the data collection was therefore about three degrees, and the error in treating the transponder signal as stationary and located at the midpoint of the boats position during collection of the spectrum was less than ± 1.5 degrees. For both procedures the position of the boat was measured using a global positioning system employing differential corrections (DGPS). In the case of the first method, the position and time were recorded manually. In the case of the second method, boat position measurements were automatically logged at 10 second intervals and stored in the memory of the DGPS unit. Of the two methods, the second was found to be much easier and less time consuming. After sufficient spectra were recorded, phase corrections were calculated to best fit, in a least squares sense, the radar's determination of the transponder signal to the known position of the boat. The individual antenna patterns of the receive elements were not measured. Ideal cosine patterns were assumed.

3.2 CODAR SeaSonde Radar Systems

In addition to the MCR systems, three SeaSonde radar systems, built by CODAR Ocean Sensors Inc., have been deployed at Monterey Bay. The SeaSonde system operates on single frequency and employs a compact co-located receive antenna geometry consisting of two crossed loops and a monopole. Signals from the antennas are processed using a direction

finding technique. The system uses a swept frequency transmit waveform to provide range resolution. This method results in a much higher transmit duty cycle compared with a pulse range gate method and thereby increases the average power output. The SeaSonde system achieves a nominal range of up to 70 km. The small size of the system has the advantage of requiring a fraction of near-shore coastal real estate required by the MCR system. The data from the SeaSonde systems at Monterey Bay was not the focus of this work but have been used in several other experiments in the past, such as the low frequency current motion investigations of Paduan and Rosenfeld (Paduan & Rosenfeld, 1996), Paduan and Cook (Paduan & Cook, 1996) and others.

3.3 Mooring Data

There were two moorings in the radar coverage area: a buoy deployed by the Monterey Bay Aquarium Research Institute (MBARI, M1) and a flux buoy deployed by the Boundary Layer Studies Group, Department of Meteorology, Naval Postgraduate School, Monterey Bay. The locations of the moorings is shown in Figure 1.1. Collectively, data from these buoys provided the following:

- Acoustic Doppler Current Profile (ADCP) current measurements at M1 used for ground truth comparisons with the radar-derived current measurements
- Wind speed and direction measurements from the flux buoy used to examine the relationship between wind speed and direction and near-surface, radar-derived current measurements from different radar frequencies

- High resolution ocean wave spectral energy measurements from the flux buoy used to estimate the current due to Stokes drift in order to evaluate its impact on the radar current measurements
- High frequency, three-dimensional wind velocity measurements from a sonic anemometer located on the flux buoy used to make direct calculations of the friction velocity in order to compare with radar-derived, near-surface current measurements

3.3.1 MBARI, M1

ADCP current data and standard meteorological data, including wind speed and direction, were collected at the MBARI buoy, M1. The meteorological data were available continuously over the time period of interest for the work described here, and the ADCP data were available for most of that time. A plot of the temporal coverage for the ADCP data can be seen in Chapter 5. The location of M1 was within the radar area of coverage, approximately equidistant from the two MCR sites, at a range of about 21 km and near the broadside direction relative to both radar systems. The location of the buoy can be seen in Figure 1.1. The top most bin of the ADCP data corresponded to a depth of 15.4 m below the surface. The ADCP data were not corrected for motions of the platform but in the past corrections due to platform motion have been small enough to be considered insignificant in the comparisons made here.

3.3.2 Flux Buoy

During the period of September 3, 1999 to November 11, 1999, a flux buoy, capable of high resolution directional wave spectral energy measurements and high frequency atmospheric

turbulence measurements, was deployed in Monterey Bay. The buoy was located within the coverage area of both MCR deployment sites, about 23 km from the northern radar site, and about 9 km from the southern site. The location of the buoy can be seen in Figure 1.1. The turbulence data system consisted of a three dimensional sonic anemometer and buoy platform motion sensors. Data were collected at a sampling rate of 10.5 Hz. From the sonic anemometer and buoy platform motion measurements, the motion corrected along stream, u, across stream, v, and vertical w wind components were obtained relative to the mean wind direction. Estimates of the wind friction velocity are given by

$$u_* = \sqrt{\frac{\tau}{\rho}} = \left[\langle -u'w' \rangle^{1/2} + \langle -v'w' \rangle^{1/2}\right]^{1/4}, \tag{3.1}$$

where $\langle u'w' \rangle$ and $\langle v'w' \rangle$ are the kinematic along-wind and across-wind momentum fluxes The prime indicates instantaneous turbulent fluctuations from the mean quantities.

High resolution directional ocean wave spectra were obtained by computing a 256 point FFT from every eighth platform motion measurement. The sampling rate was $10.58/8 = 1.3125$ Hz. Individual spectra produced about every 3 minutes were averaged to form 48 minute spectra. The frequency resolution of the spectra was $\Delta f = 10.5/(8 \cdot 256) = 0.0051$ Hz and the frequency range was from Δf to $(256 \cdot \Delta f)$ or 0.0051 to 0.66 Hz. The angular resolution was to one degree. A more complete description of the flux buoy instruments, measurements, data products and calculations is given in a data report by Fredrickson *et al*. (Frederickson et al., 2000).

Chapter 4

Simulation-Based Evaluations of HF Radar Ocean Current Algorithms

4.1 Overview

Simulation experiments have led to improved understanding of the relationship between errors in current estimation and model parameters that describe the state of the sea surface. They have also helped identify problems with the application of the MUSIC algorithm to the MCR radar system data and to design and test modifications to the algorithm to improve performance. A description of the simulation work presented here has been published by IEEE, Journal of Oceanic Engineering (Laws et al., 2000). In this Chapter we mathematically model the sea echo for a given set of parameters that describe the sea surface state, and thereby simulate the signals one would expect to receive for a given HF radar system. The parameters

describing the radar system were taken from the MCR system, described in Section 3.1.

In general, the methods used for range resolution of HF radar current measurement systems are well understood. More difficult to understand, and problematic in terms of error estimation, are the techniques for obtaining directional resolution (pointing techniques). There are two basic categories of pointing techniques. These are direction finding and beam forming. At present, HF radar systems can be divided into two types by the receive antenna geometries used; namely, compact co-located antennas and linear phased arrays. Typically, beam forming is used with phased arrays and, out of necessity, direction finding is used with co-located antenna geometries. When analyzing HF radar data, one would naturally like to use the best algorithm available. Therefore, the question arises: can direction finding techniques be applied to phased arrays with better results than beam forming? If so, the versatility of phased array systems could be increased by removing the requirement of very large receive arrays for operation in the lower region of the HF band and eliminating the limits on angular coverage. In order to investigate this, or any other question regarding the accuracy of HF radar algorithms, some measure of success or ground truth is required. Graber et al. (Graber et al., 1997), among others, have made substantial progress in estimating errors through comparison with in-situ measurements. However, inherent differences between measurement methods and uncertainties in the in-situ measurements themselves limit this method of estimating HF radar measurement errors. In this study we evaluate different radar algorithms using simulated backscatter data, which offers unique advantages compared with evaluations based on in-situ data. For simulations, for instance, the parameters of the sea surface state are known, and may be manipulated

so that the performance of processing algorithms can be compared over a range of conditions. Although not addressed in this study, simulation methods have also been applied to the compact co-located configuration of the SeaSonde radar systems (Barrick & Lipa, 1996).

In this analysis, we first briefly describe the two pointing algorithms under discussion: a direction finding approach developed by Schmidt (Schmidt, 1986) called MUltiple SIgnal Characterization (MUSIC), and conventional beam forming. We then describe the process by which the simulated sea echo is generated, as well as the various parameters that define the sea surface state. We describe modifications made to adapt the MUSIC algorithm for use with HF radar. We then show results that contrast the performance of the two pointing techniques as a function of sea surface state parameters. We examine the following:

- the dependence of error on signal-to-noise ratio (SNR) at different radar operating frequencies
- the effect of wind direction under the assumption of equilibrium conditions with a uniform wind
- the response of the algorithms in cases where part of the ocean surface is sheltered or blocked from Bragg resonant waves resulting in reduced sea echo power in that region
- the relationship between radar operating frequency and the radar's ability to resolve a sharp current feature
- the effect of averaging subsequent measurements given a statistically stationary sea state

4.2 Pointing Techniques

4.2.1 Beam Forming

Of the two techniques, beam forming is the more conventional approach. In beam forming, phase shifts are applied to signals from the individual antenna elements so that when the signals from all elements are summed, only those from a given direction will add in phase. In this way, the sensitivity of the receive array is effectively steered to the desired direction. Surface current measurements are then made using a centroid calculation over the region of each of the two Bragg peaks in the Doppler spectrum of the sea echo. The angular resolution is limited by the width of the formed beam, and the range of angular coverage is limited by side lobes which grow rapidly as the radar look angle approaches the direction parallel to the array axis. For a given receive array geometry, angular resolution and range of angular coverage are both reduced as the operating frequency is decreased. Side lobes of the formed beam are generally reduced, at the expense of beam width, by the application of an amplitude weighting window over the array elements. For the MCR, the amplitude weighting window was determined for each steering angle using a least squares comparison with an ideal beam pattern.

Figure 4.1 shows the resulting beam patterns using this method for the MCR's receive array geometry. For each radar frequency, beam patterns for zero and approximately -35 degree beam steering angles are shown. The beam patterns clearly illustrate the problem encountered when trying to use beam forming methods with a limited aperture array. For the lowest MCR frequency (4.8 MHz), the length of the array (48.3 m) is only .77 wavelengths. This restricted aperture results in a very broad beam and poor angular resolution. The angular resolution at

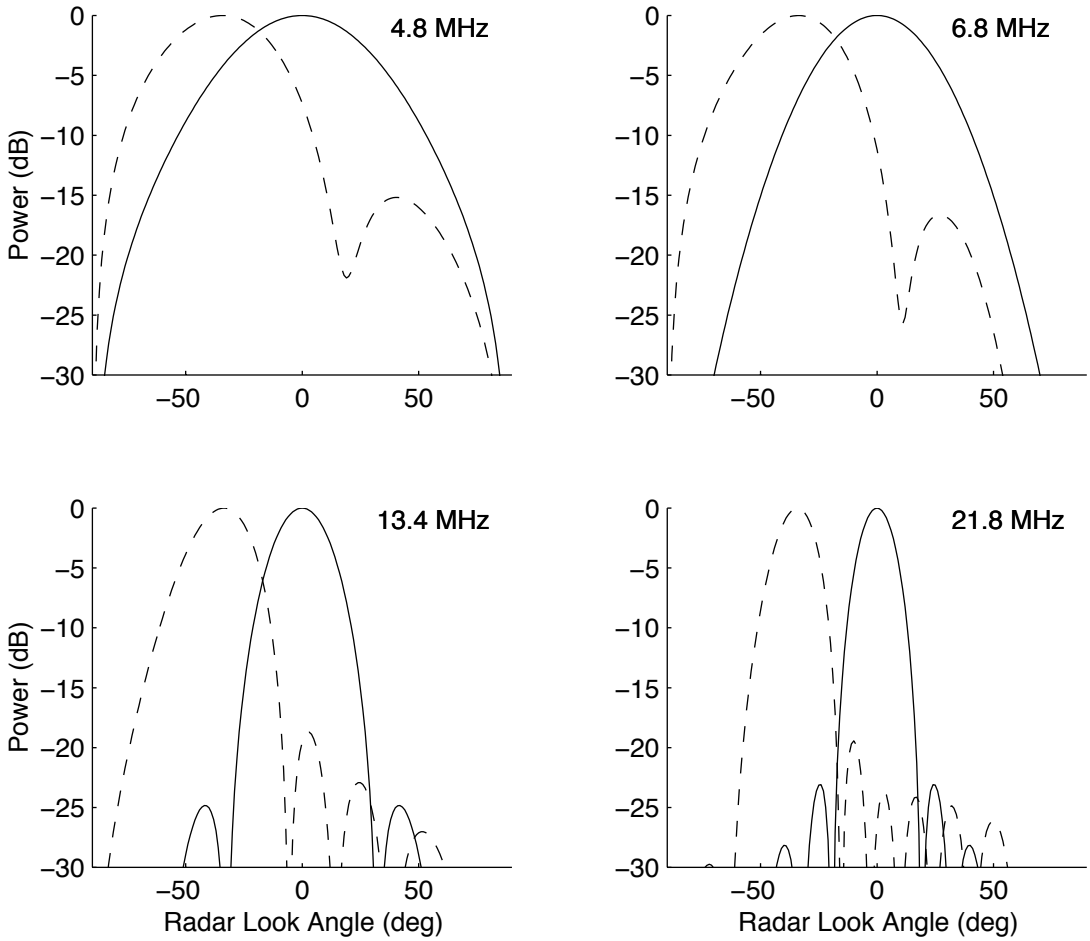

Figure 4.1: Beam patterns for the MCR's eight element receive antenna array at each of the four operating frequencies. Two beam steering angles, 0°, i.e., perpendicular to array axis (solid line) and near the limit of the arrays steering capability at approximately -36° (dashed line), are shown.

frequency	Steering Angle	Beam Centroid	Steering Error	Beam Width
Hz	Deg	Deg	Deg	Deg
4.8	0	0.0	0.0	56
4.8	-37	-33.7	3.3	47
6.8	0	0.0	0.0	44
6.8	-36	-35.4	0.7	40
13.4	0	0.0	0.0	24
13.4	-36	-35.5	0.3	25
21.8	0	0.0	0.0	14
21.8	-35	-34.8	0.5	17

Table 4.1: Beam width and steering error for MCR's receive antenna array at four radar frequencies for 0° and -36° radar look angles.

the lower frequencies could be improved by using a longer receive array, but the problems associated with site selection often make a longer array impractical. The error between the intended beam steering angle and the centroid of the beam pattern and the full width at half power are given for each frequency in table 4.2.1. Differences between the direction of the ideal beam pattern and the centroid of the formed beam are insignificant relative to the beam widths.

4.2.2 Direction Finding (MUSIC)

MUSIC can be employed with an arbitrary antenna geometry, including linear phased arrays and compact co-located configurations. In MUSIC direction finding, the algorithm processes each spectral point where Bragg energy is detected in the Fourier spectrum of the received signal and determines the direction toward the patches of the ocean surface which are reflecting the radar signal at that Doppler shift. This is equivalent to choosing a radial surface current magnitude, and then determining the bearings of patches of the ocean surface where that current magnitude is present. The number of directions that can be resolved for a single current

magnitude is limited to the lesser of $(n-1)$ and M, where n is the number of sensor elements in the receive array and M is the number of data segments averaged in the process of making the measurement. Without delving too deeply into the mathematics, which are covered in detail in the doctoral dissertation by Schmidt (Schmidt, 1981), MUSIC determines the locations of signal emitters through analysis of the sample-averaged antenna covariance matrix. The largest eigenvalues of this matrix are associated with signals and the others are associated with noise. The ability to determine direction of arrival (DOA) for each of the signal emitters is based on the fact that the signal eigenvectors are mutually perpendicular to each other and to the noise eigenvectors. Provided the above limit on the number of signal emitters is not exceeded, the directions of arrival for each of the emitters can, in principle, be completely resolved.

The angular resolution is set by a parameter in the MUSIC processing. For the MCR, 2 degrees was used, but in practice angular resolution is generally limited by the frequency resolution of the Fourier spectrum of a data segment. The frequency resolution translates directly to a velocity resolution and the velocity resolution is related to the angular resolution by the slope of the current profile as illustrated in Figure 4.2. This resolution limit, however, may not be the dominant factor contributing to errors in determination of DOA for a given signal. There are other sources of error that may affect MUSIC processed results that involve the ocean processes themselves. If the number of signal emitters is less than the number of sensor elements, the ensemble averaging is large enough in extent, and the noise and the signal variations due to randomness in the waves are both purely Gaussian, then MUSIC should resolve the DOA(s) for each emitter without error. These conditions are not all completely met in the case of applica-

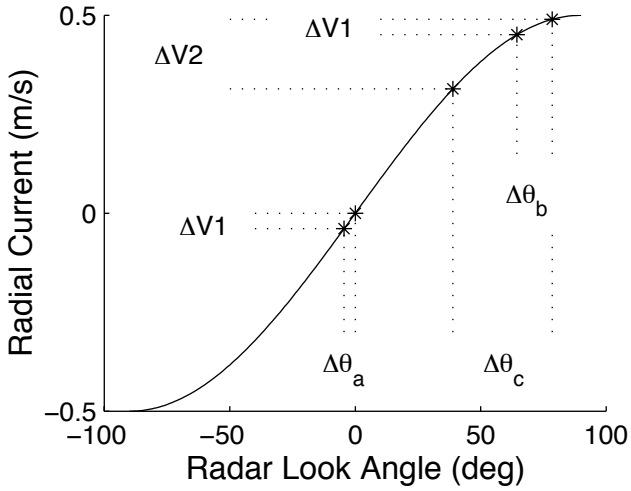

Figure 4.2: Relationship between velocity resolution, angular resolution, and current profile slope for a sample radial current profile. This is an ideal resolution limit based only on the frequency resolution of the Doppler spectrum and the characteristics of the current profile. The radial current profile shown results from a uniform current flowing parallel to a straight coastline. The radar look angle of 0 deg is perpendicular to the coast. Current velocities shown are ($\Delta V1 = 0.039$ m/s) for the 21.8 MHz frequency and ($\Delta V2 = 0.18$ m/s) for the 4.8 MHz frequency. In both cases, resolutions correspond to a 256 point FFT. The corresponding angular resolutions shown are $\Delta\theta_a = 4.5^o$ (21.8 MHz), $\Delta\theta_b = 14.1^o$ and $\Delta\theta_c = 39.6^o$ (4.8 MHz).

tion to oceanography. The signal variation due to randomness in the waves has been shown by Barrick and Snider (Barrick & Snider, 1977) to be best represented as a Gaussian random variable, but sample time is limited to less than the time scales of variation in the surface currents. The limited sample time leads to a restricted level of ensemble averaging and subsequently to errors in the determination of both the number of emitters and the corresponding DOA(s). Also, the number of signal emitters is not necessarily well defined. The signal emitters are distributed over regions of the ocean surface with dimensions of a range azimuth cell. These regions may contain significant variations in surface current magnitude. The effect of these variations on MUSIC processing has not been well characterized.

4.3 Radar System Parameters

4.3.1 Optimization Considerations

Excluding changes to antenna geometry and power output, the primary user controllable factors limiting the accuracy and resolution of any ocean radar system are operating frequency and sample time. With beam forming, accuracy improves with increased frequency via reduced side lobes and beam width until the limit of optimal receive array spacing, half wavelength, is reached. The accuracy of MUSIC and, to a lesser extent, beam forming improves with the velocity resolution of the Doppler spectrum which in turn improves with frequency. Accuracy improves with increased sample time either by increased spectral averaging or by increased resolution of the Doppler spectrum.

Problems associated with higher frequencies include increased propagation loss and

problems due to higher order reflections. Other considerations involving frequency depend on the nature of the experiments themselves. For example, experiments such as those of Fernandez et al. (Fernandez et al., 1996) that involve the ability of radar to measure shear, require a radar system that is capable of operating over a range of frequencies. Fresh water experiments such as those of Fernandez et al. (Fernandez et al., 1999) suffer from much greater propagation loss and may have limited Bragg wave energy in some portions of the HF band.

Limitations on increased sample time include reduced temporal resolution and the assumption that sea state parameters of interest remain constant over the duration of the measurement. Another factor that may limit sample time arises from the fact that two or more radar systems covering the same area from different angles are required in order to form a full vector current measurement. The need to share transmit time is therefore often an issue.

4.3.2 Radar Resolution

Resolution for any HF radar installation involves both angular resolution and frequency (velocity) resolution. The velocity resolution is determined by the segment length and the radar wavelength, and is given by

$$v_{res} = \lambda_r / 2 n_{seg} \Delta t, \tag{4.1}$$

where λ_r is the radar wavelength, n_{seg} is the number of samples in a data segment and Δt is the pulse repetition period, or sample rate. Additionally, for a fixed Δt, the Nyquist frequency sets the largest current velocity measurable at

$$v_{max} = \frac{\lambda_r}{4 \Delta t}. \tag{4.2}$$

Any current velocity larger than v_{max} will result in aliasing of the Bragg region. Since the radial current velocity may either add to or subtract from the still water phase speed of the Bragg resonant wave, Δt must be kept small enough so that the radial component of ocean surface currents (v_{rad}) in the radar coverage area satisfy the condition,

$$|v_{rad}| < v_{max} - c_p, \tag{4.3}$$

where c_p is the still water phase velocity of the resonant deep water gravity waves, given by

$$c_p = \sqrt{\frac{g\lambda_r}{4\pi}}. \tag{4.4}$$

With beam forming, angular resolution at a given frequency is dependent on the width of the formed beam, which is roughly λ_r/D radians, where D is the length of the receive array. To optimize a beam forming system for a desired resolution, one must either have enough space to deploy a long enough array or, alternatively, select a frequency high enough to obtain the desired resolution, given the length of array which may practically be deployed.

Resolution with MUSIC processing is more complicated. In order to form the sample averaged antenna covariance matrix, each data set comprising a single measurement must be divided into a number of data segments. The accuracy of MUSIC analysis improves with the number of segments (M) due to increased averaging, and with the number of points per segment (n_{seg}) by virtue of improved velocity resolution. For the MCR, data collection typically involves 1024 data points with a pulse repetition period (Δt) of 0.6912 seconds. The time required for a single measurement is therefore 707.8 seconds. Seven segments of 256 points each are obtained from the 1024 point data set by allowing a 50% overlap of the segments. A Hanning window is applied to each segment, which reduces the statistical dependence of the segments.

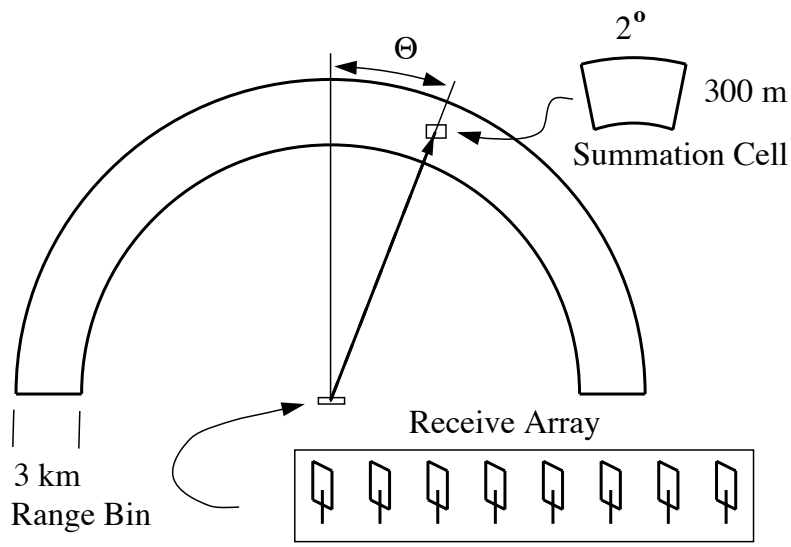

Figure 4.3: Geometry of the simulation. A single range bin 3 km wide covering 180 deg of azimuth is considered. The coastline is assumed to be straight and parallel to the axis of the receive array. The radar look angle, θ, is referenced perpendicular to the array axis, positive clockwise. Reflections from cells 2 deg by 300 m are summed to find the total sea echo for the range bin.

4.4 Generation of Simulated Sea Echo

The simulation generates the expected voltage-time series for each antenna element in the radar's receive array due to first order scatter from a single range bin of the ocean surface. The geometry is shown in Figure 4.3. The width of the range bin (Δr) is determined by the radar pulse length and given by $\Delta r = ct/2$, where t is the radar pulse length in seconds. For the MCR, this width is about 3 km. In order to calculate the time series data for a given antenna element, n, we compute the sum

$$\psi_n(t) = \sum_{j,k} \gamma_n(\theta_j) e^{i\phi_n(\theta_j)} \sigma(r_k, \theta_j, t) + e_{noise}(t), \tag{4.5}$$

where j and k denote the summation cells in the given range bin, i, is used to represent the square root of negative one and the notation (γ_n, ϕ_n, σ and e_{noise}) are defined below. The dimensions of a summation cell (2 degrees by 300 m) were selected so that the individual cell could be considered small in comparison with the 180 degree by 3 km section of ocean surface being simulated without unnecessarily increasing processing time. Using the above cell dimensions, the processing time to generate simulated time series data at a single frequency and process the data with both beam forming and MUSIC algorithms was 17 seconds using an Intel Pentium II processor running at 400 MHz. The effect of variations in cell dimensions about these values was examined and did not have a significant effect on the results. For simplicity, the noise voltage, $e_{noise}(t)$, is added to the voltage time series after computing the sum. The individual antenna patterns of the receive elements are described by $\gamma_n(\theta_j)$, which in this case were the ideal cosine patterns for the loop elements used in the MCR's receive array. The phase factor, $e^{i\phi_n(\theta_j)}$, describes the relative phase shifts between receive array elements. For the case of a linear phased array, with elements separated by a distance d and illuminated by plane waves of wavelength λ incident from an angle θ_j, the phase angle for the nth antenna element is given by

$$\phi_n(\theta_j) = \frac{2\pi}{\lambda} nd \cos(\theta_j). \tag{4.6}$$

The sea echo is dominated by Bragg resonant reflections from ocean wavefronts that have wavelengths of exactly half the radar transmit signal, and propagate directly toward and away from the radar (Crombie, 1955). The contribution from a given summation cell may therefore be expressed as the sum of two exponentials, due to the approaching and receding Bragg resonant

waves,

$$\sigma(r_i, \theta_j, t) = A_+ e^{[i(\omega_v + \omega_a)t]} + A_- e^{[i(-\omega_v + \omega_a)t]}, \tag{4.7}$$

where ω_v is the Doppler shift due to the still water phase velocity of the resonant waves and ω_a is the Doppler shift due to the average radial component of surface currents giving rise to advection of the given summation cell. These shifts are given by

$$\omega_v = 4\pi f_r \frac{v}{c} \tag{4.8}$$

$$\omega_a = 4\pi f_r \frac{u_a}{c}, \tag{4.9}$$

where u_a is the average radial component of the surface current and f_r is the radar frequency. Barrick and Snider have shown (Barrick & Snider, 1977) that the sea surface height, and hence the amplitude of the sea echo due to Bragg scatter, is best represented as a zero mean Gaussian random variable. The coefficients A_+ and A_- in Equation 4.7 must contain both the random nature of the ocean surface and the variation in reflected signal amplitude due to anisotropy in the average wind-wave height. The coefficients are therefore defined by

$$A_\pm = a_\pm + ib_\pm \tag{4.10}$$

$$\langle a_\pm \rangle = \langle b_\pm \rangle \equiv 0 \tag{4.11}$$

$$\langle a_\pm^2 \rangle = \langle b_\pm^2 \rangle \equiv \eta, \tag{4.12}$$

where the real and imaginary components of coefficients $A_\pm$ are zero mean Gaussian random variables with variance proportional to the ocean wave spectral energy at the Bragg frequency. For simplicity, we assume a fully developed sea and uniform wind, so that the wind direction and the spectral energy of the resonant waves, η, have the broad cardioid relationship, $g(\theta)$

given in Equation 2.9, where θ is the angle between the wind direction and the direction toward the given summation cell (parallel to the propagation of Bragg resonant waves). The small numerical constant, α, in 2.9 accounts for waves propagating anti-parallel to the wind direction (Tyler et al., 1974). Following Barrick and Lipa (Barrick & Lipa, 1996), the values $\alpha = 0.01$ and $s = 4$ were used.

4.5 MUSIC Algorithm Modifications

Problems with implementation of the MUSIC algorithm for HF radar current measurements using the MCR were made apparent by the number of physically unlikely solutions observed in real current measurements and the number of very large error current solutions observed with simulated data. Two modifications were made to the original MUSIC algorithm to adapt it for use with HF radar signals. The first modification deals with the determination of the number (K) of signal emitters present at a given Doppler shift, which corresponds to the number of directions where a radial current of a given magnitude is present. The second modification involves problems associated with limited sample time and weak currents.

The determination of the number of directions from which a given signal originated, refered to as directions of arrival (DOA), is important to the accuracy of the MUSIC direction finding algorithm. If it is determined that a given signal has multiple DOA's when this is in fact not the case, MUSIC will produce errant solutions. On the other hand, situations where a given signal does have multiple DOA's are physically plausible. An offshore jet or a current front are two examples that can result in radial current profiles that contain two or more locations in a

single range bin where the radial current magnitude is the same. In these situations a signal corresponding to a given radial current magnitude will have multiple DOA's and if the MUSIC algorithm is restricted to only one DOA for a given signal, sparse coverage will result.

In the original adaptation of MUSIC to the MCR, the algorithm determines the number of DOAs for a given frequency bin by a statistical approach, the validity of which is based on the assumption that the number of data segments (M) is large. Once the number of DOA's has been determined, the directions are then computed. To improve the performance of the algorithm, a cutoff based on comparing the power of the spectral point being processed with the overall background received power is employed to avoid processing currents from noise-dominated spectral points.

Analysis using simulated data showed that the cutoff was effective for rejecting high error solutions only when the overall SNR was low. The results of the analysis are shown in Figure 4.4. For the low SNR example shown, a cutoff of about 3 dB would be effective in rejecting most of the high error solutions, but for the high SNR case, a cutoff of almost 20 dB would be required to reject a similar percentage of the high error solutions. Such a high cutoff would reject too large a percentage of the low error solutions as well. The criterion was therefore ineffective in removing the high error solutions. Examination of results with simulated data revealed that the algorithm was too often selecting multiple DOA solutions, even when the current profile input to the simulation contained only a single angle solution for the radial current magnitude being processed. It was concluded that the value of M was insufficient for an accurate statistical determination of K. These observations, along with conversations with Don

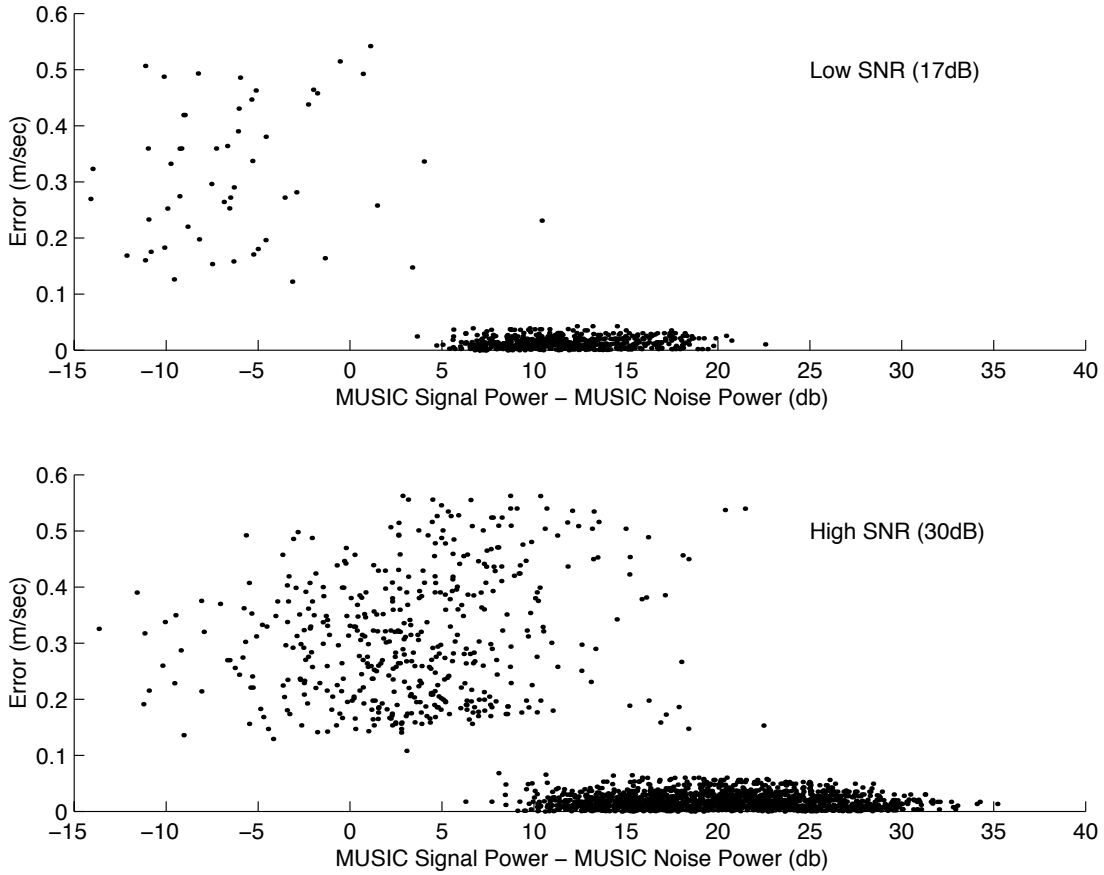

Figure 4.4: Error of individual MUSIC solutions as a function of power above noise level for high and low overall SNR.

Barrick of CODAR Ocean Sensors, Ltd., on Barrick and Lipa's implementation of MUSIC with the CODAR SeaSonde system (Barrick & Lipa, 1997), led to modifications that examine solutions from all K inversions to determine whether solutions from a particular inversion should be accepted or rejected.

Modifications were developed by examination of the algorithm's determination of DOA. Essentially, DOAs at a given Doppler shift are found by determining the locations of peaks in the DOA_K spectrum, defined by

$$DOA_k \equiv \frac{1}{\alpha^\dagger(\vartheta) E_{K^c}^\dagger E_{K^c} \alpha(\vartheta)}, \tag{4.13}$$

where $\alpha(\vartheta)$ is the matrix of model signal vectors, which describes the phase and amplitude characteristics of each receive array element, E_{K^c} is the matrix of signal null-space eigenvectors, i.e. noise eigenvectors, for a K signal emitter solution, and the † indicates the complex conjugate transpose operation. The location of peaks in a DOA_K spectrum correspond to the angles where the model signal eigenvectors are perpendicular to the noise eigenvectors and therefore correspond to solutions for the DOAs of the signal. If the determination of K is correct for the given radial current profile, and the noise has been sufficiently reduced by averaging, there should be exactly K peaks denoting angular locations on the sea surface with the current magnitude that corresponds to the Doppler frequency being processed. In analysis of simulated data using the original MUSIC algorithm, this was often not the case. That is, the algorithm often chose the wrong value for K and, hence, the wrong number of DOAs. For a given K inversion, it was also common to find a mismatch between the value of K and the actual number of peaks in the DOA_K spectrum. It was found that solutions with high error tended to originate

from DOA_K spectra for which the number of peaks found in the spectrum was greater than K, and from spectra that contained peaks at the edges. Since the edges of a DOA_K spectrum correspond to angles nearly coincident with the axis of the receive antenna, this latter effect may be unique to the MCR's receive antenna geometry, which uses loop elements with a null in sensitivity along the axis.

The first modification to the MUSIC algorithm abandons the statistical test to predetermine K, and instead cycles through a subset of the possible values for K. For the MCR, solutions for up to seven DOAs could be found for a single current magnitude. Given the current resolution limitations, however, it is physically unlikely that an ocean current profile would contain more than two or three resolvable DOAs for a single radial current magnitude. The value of K was therefore limited to a maximum of four. The value for K was not limited to a smaller value, say one, because this may exclude physically realizable solutions. For each value of K, the DOA_K spectra are evaluated. If the number of peaks in a DOA_K spectrum is found to be greater than K, or if the spectrum has peaks at the edges, the spectrum is rejected. Peaks in a spectrum are identified as follows: first all positive extrema in a spectrum are identified as possible peaks, next a histogram of the points within the spectrum is analyzed to separate peaks from noise by defining cutoffs where the number of points in a histogram bin has fallen by e^{-1} and by e^{-3} from the number of points in the first bin. Then, extrema that are greater than the first cutoff are categorized as peaks and extrema greater than the second cutoff are classified as significant peaks. A sample DOA_K spectrum and histogram are shown in Figure 4.5. All peaks are counted in determination of whether a spectrum is to be rejected, but only significant

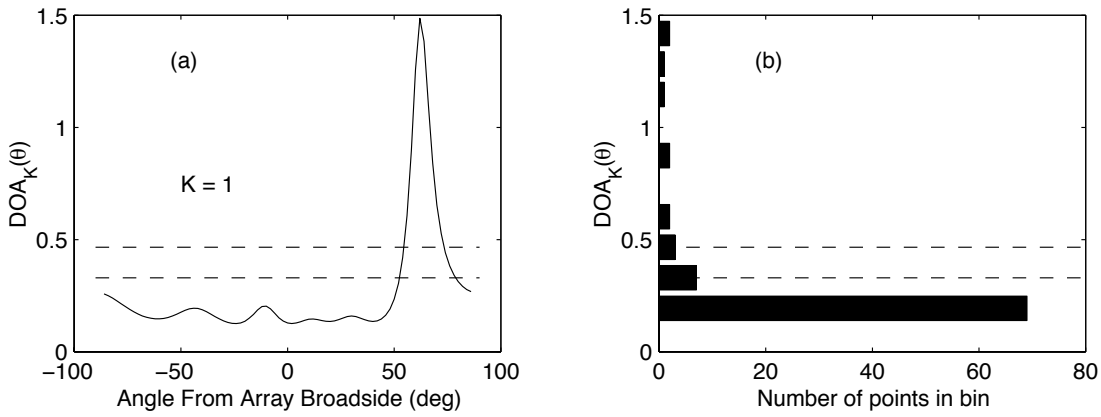

Figure 4.5: DOA_K spectrum for K = 1 (a), and its histogram (b). The dotted lines indicate the positions of cutoffs for classifying peaks.

peaks are processed to determine currents. Further optimization could certainly be done, but application of these criteria reduced the instances of large error solutions significantly. Figure 4.6 shows results that demonstrate typical improvement (for the 21.8 MHz frequency, at about 30 dB SNR) due to this modification.

The second problem illuminated through examination of simulated data involves large errors with generally weak currents. The errors result from the processing of frequency bins outside the Bragg region due to spreading of the Bragg peak. This causes the algorithm to try to determine DOAs for frequencies that correspond to currents that are greater in magnitude than any present in the given range bin. The errors caused by this problem are particularly significant for the lower MCR operating frequencies where the current resolution is poor. Figure 4.7, panel (a), illustrates the problem. The radial current input to the simulation varied in size from -0.10 to +0.20 m s^{-1} over the angular range, and the SNR of the Bragg signal was fairly high (about

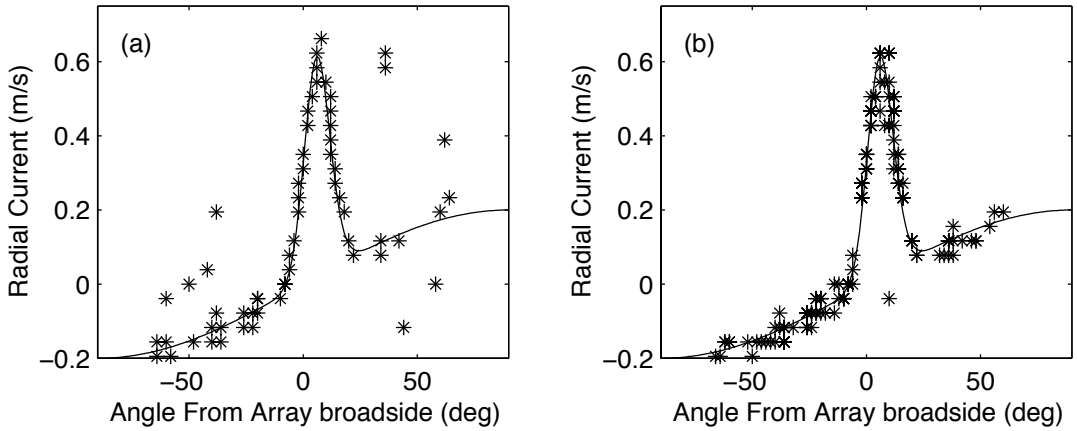

Figure 4.6: Improvement in MUSIC processed current measurement due to algorithm modifications. Current measurements made from simulated data using the original adaptation of the MUSIC algorithm (a) and the modified algorithm (b). The results shown are for the 21.8 MHz frequency, and relatively high SNR (30 dB). The solid line is the radial current input to the simulation.

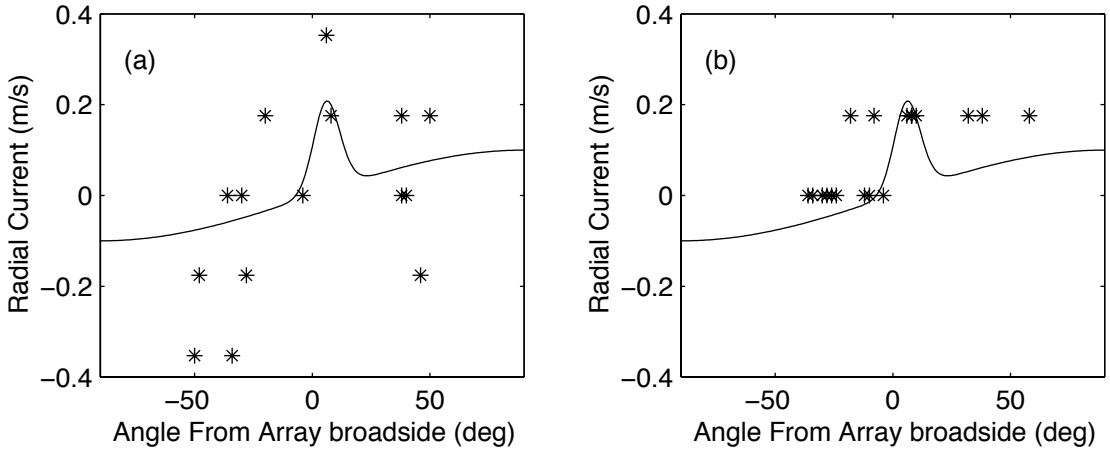

Figure 4.7: Reduction of errors for the case of a simulated weak radial current profile. The modified algorithm (b) still shows poor resolution for this frequency and sample time, however, results containing currents larger in magnitude than those input to the simulation, apparent in the original adaptation of the MUSIC algorithm (a), have been eliminated.

30 dB). At the 4.8 MHz frequency, where the current resolution is 0.18 m s^{-1}, five frequency bins in the 256 point fast Fourier transform (FFT) were found to have Bragg energy and were therefore processed. The current velocity that corresponds to the most negative frequency bin is -0.35 m s^{-1}. Since the most negative current input to the simulation was only -0.10 m s^{-1}, the resulting error due to processing the bin will be greater than 0.25 m s^{-1} no matter where MUSIC locates the signal source. To address this problem, the second modification to the MUSIC algorithm uses a single 1024 point FFT to define limits on the space spanned by the Bragg region before processing for currents takes place. Then direction finding analysis is performed using 256 point segments as normal, but only frequency bins within the more precisely defined Bragg region are processed. Results with the modified algorithm are shown in Figure 4.7, panel (b).

4.6 Results

In this section we report on simulations of the MCR under varying wave and current conditions. Performance of different algorithms are evaluated with the goal to develop better error characterization for real-world applications.

4.6.1 Signal-to-Noise Ratio

A uniform current flowing parallel to shore was used to investigate the effect of SNR on errors in current measurement. Wind speed, duration and fetch were assumed to be sufficient for fully developed Bragg resonant waves at all radar frequencies, so that power of the sea echo

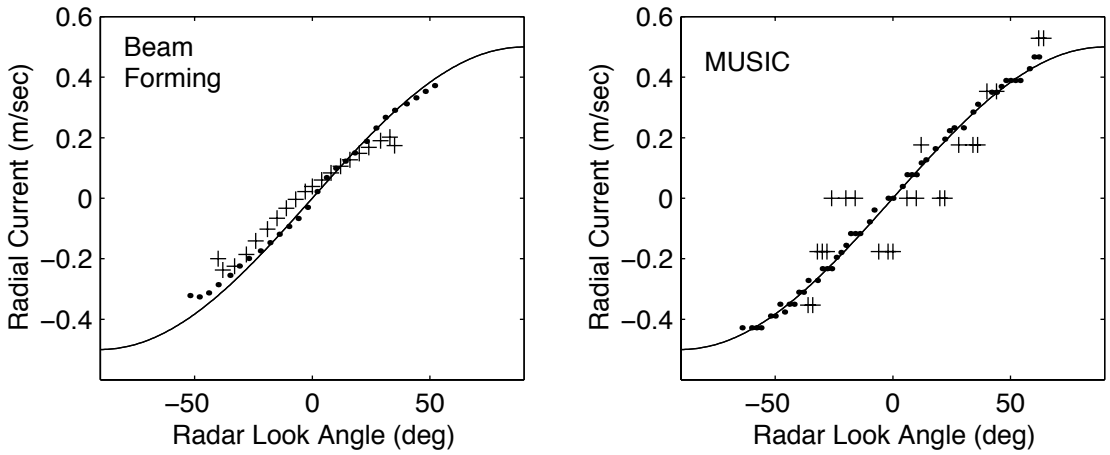

Figure 4.8: Simulated radial current profile due to a uniform current flowing parallel to shore (solid line) with measurements from beam forming and MUSIC processing at 4.8 MHz (plus) and 21.8 MHz (dot) operating frequencies. With MUSIC, the random nature of the errors is apparent, along with the dependence of error and current resolution on operating frequency. Errors with beam forming are lower than with MUSIC, particularly at the lower frequency, and can be seen to begin to increase with large look angle.

could be represented by the cardioid dependence on wind direction relative to radar look angle given by Equation 2.9. Angles are referenced relative to array broadside, i.e., perpendicular to array axis. The wind direction was set parallel to 60 degrees, propagating toward the radar, and held constant. Figure 4.8 shows an example of the shore-parallel current profile and measurements from both beam forming and MUSIC algorithms. The measurements shown are taken using the highest and lowest radar frequencies of operation, for a typical run of the simulation at 25 dB SNR measured using the signal strength of the formed beam. The SNR of a single element of the eight element antenna array can be estimated by subtracting 9 dB or one-eighth of the SNR of the formed beam. In the beam forming case, errors are fairly low even for the lowest frequency. This agrees with expectations since the dominant source of error is due to beam width and, for this smooth current profile, errors caused by averaging over beam width

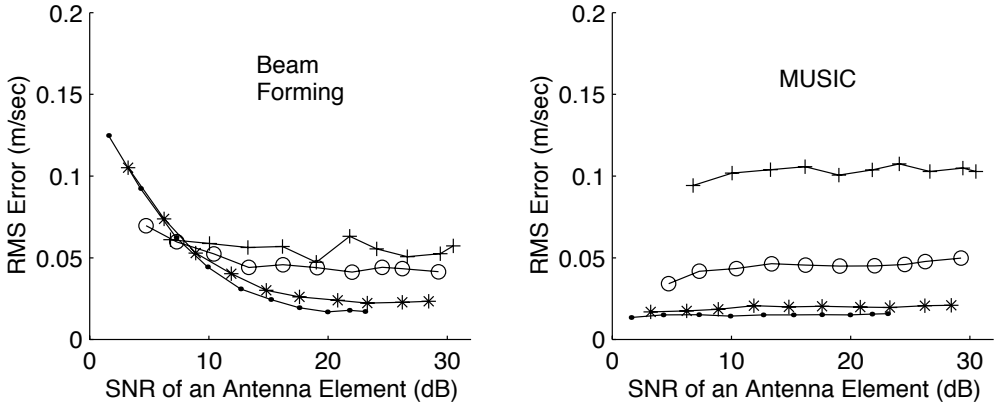

Figure 4.9: RMS error as a function of simulated input signal SNR. The dependence of RMS error on SNR is shown for 4.8 (plus), 6.8 (circle), 13.4 (star), and 21.8 (dot) MHz frequencies of operation with both beam forming and MUSIC processing. With beam forming, a clear SNR dependence is apparent, particularly for the higher frequencies, while errors with MUSIC are independent of SNR over this range.

are small even for a very broad beam. With MUSIC, errors at the lower frequency are larger than for beam forming and random in appearance. The coarseness of the current resolution is apparent in the low frequency results. To determine the dependence of error on SNR, the simulation was run repeatedly over a range of background noise levels, 30 times at each noise level. The RMS error was computed over angles and averaged over the 30 runs to reduce statistical variations.

Figure 4.9 shows the results from processing the simulated data with both MUSIC and beam forming over the range of SNR. Results show MUSIC measurements to have a lower RMS error for the two highest frequencies (21.8 and 13.4 MHz), comparable error for 6.8 MHz, and higher error for 4.8 MHz for values of SNR above 25 dB. Below 25 dB, errors in beam formed measurements show an approximately inverse relationship to SNR for the two higher

frequencies and a weaker dependence for the two lower frequencies. In contrast, errors in MUSIC measurements show practically no dependence on SNR for any of the four frequencies. As will be discussed in more detail in Section 4.6.3, simulation results indicate that limitations in MUSIC processing due to SNR have the effect of reducing the number of solutions obtained, resulting in sparser coverage, rather than increasing the error of the solutions that are obtained. Errors in the MUSIC processed results, and to a lesser extent, the beam forming results, show a strong dependence on operating frequency.

4.6.2 Wind Effects

The effect of wind direction was examined through simulations using a current profile that contained a Gaussian-shaped, offshore-directed current jet feature superimposed with a uniform parallel-to-shore current. The magnitude of the parallel-to-shore component was 0.20 m s^{-1} and the magnitude of the jet was 0.30 m s^{-1}. The SNR was approximately 15 dB. A typical example of the current profile and measurements with both beam forming and MUSIC at the highest (21.8 MHz) and second lowest (6.8 MHz) frequencies is shown in Figure 4.10. This profile was chosen both because of its physical interpretation as a current jet or plume, and because of its advantages for testing the weaknesses of the pointing techniques. The profile is challenging for beam forming because inherent averaging over beam width and the presence of side lobes lead to larger errors for profiles with sharp features. The profile is challenging for MUSIC both because it can contain, depending on jet amplitude, regions of single, double and triple DOAs, and because errors in directional determination lead to large errors in current magnitude determination.

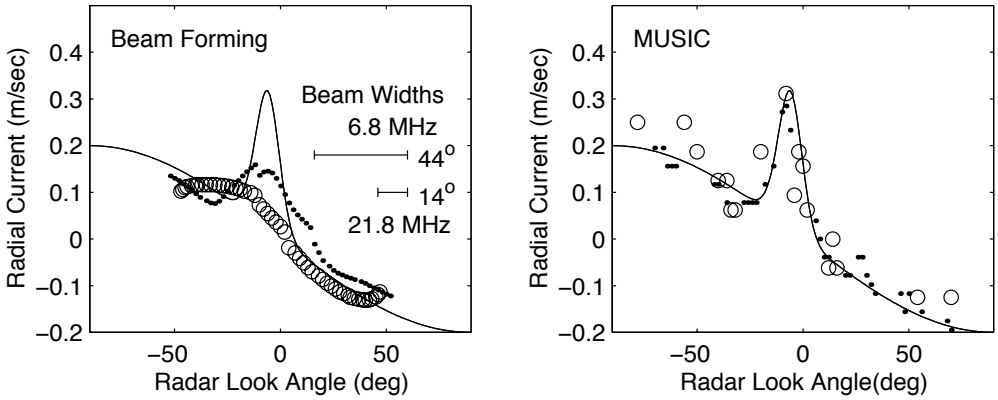

Figure 4.10: Plots of current measurements obtained from simulations using beam forming and MUSIC processing for the 6.8 MHz (circle) and 21.8 MHz (dot) frequencies, and the radial current profile input to the simulation (solid line). For both frequencies, beam forming measurements underestimate the current magnitude near the peak of the jet feature because of the 14° and 44° beam widths for the 12.8 and 6.8 MHz frequencies, respectively. MUSIC results show greater statistical uncertainty, particularly at the lower frequency, but do a better job of characterizing the jet because of the much better azimuthal resolution of the MUSIC technique for resolving sharp current features (see Figure 4.2).

The simulation was run for two different wind directions: wind parallel to 0° radar look angle and directed toward the radar, to simulate directly on-shore conditions, and wind directed parallel to a 90° radar look angle to simulate shore-parallel wind conditions. The shore-perpendicular case results in comparatively strong signals near 0° look angle while the shore-parallel case results in comparatively strong signals near the look angles with magnitude 90°. The simulation was repeated 30 times for each wind direction. The magnitude of the error found at each radar look angle was averaged over the 30 simulation runs to reduce statistical variations in the analysis. Wind speed, duration and fetch were assumed to be sufficient for fully developed Bragg resonant waves at all radar frequencies. In order to fairly compare beam forming and MUSIC, the MUSIC measurements were interpolated to a resolution of 2 degrees, and the beam formed measurements were obtained by steering the beam in 2 degree steps.

Error as a function of radar look angle, for the two wind direction cases, is shown in Figure 4.11. Since the highest radar operating frequency was the most sensitive to wind direction, results for that frequency are presented. Errors with beam forming are largest near the region of the jet as expected due to averaging over beam width. Differences in the results for the two wind direction cases show that the error is larger for look angles where the signal is relatively weaker. This was expected in the beam forming processed results due to the dependence of error on SNR.

With MUSIC, the variation in SNR due to wind direction affects primarily the likelihood of obtaining a solution at a given location, and not the error of the solutions that are obtained. Near the region of the jet feature, where current changes as a function of azimuth are

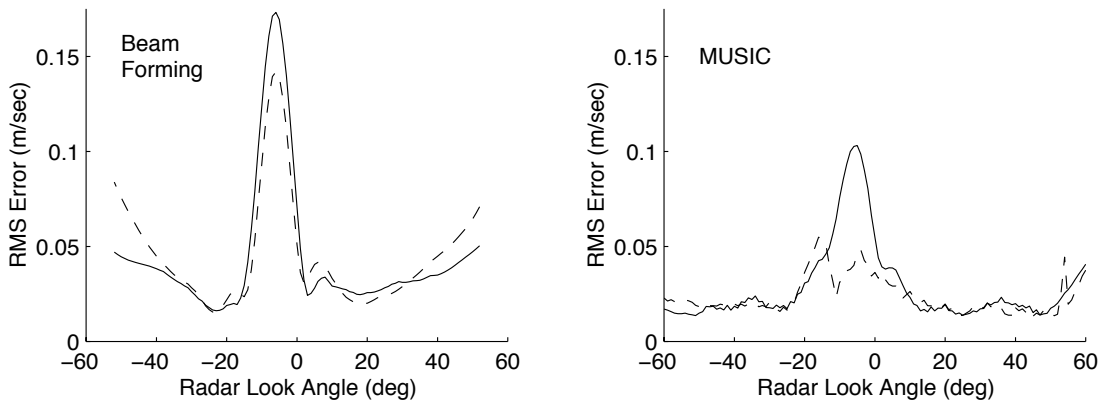

Figure 4.11: Error as a function of radar look angle demonstrating the effect of wind direction on current measurement accuracy. Results using two different simulated wind directions are shown in each plot. The two wind directions are: (1) directed parallel to a 90° radar look angle (solid line), equivalent to a shore-parallel wind and (2) directed parallel to a 0° radar look angle and toward the radar (dashed line), equivalent to a directly on-shore wind (0° is defined as parallel to antenna array bore-sight i.e., perpendicular to shore). Results with both beam forming (left panel) and MUSIC (right panel) at a radar frequency of 21.8 MHz are shown. The radial current input to the simulation contained a jet feature located at about -5° look angle. An increase in error can be seen where wind direction is nearly perpendicular to look angle, for both beam forming and MUSIC.

sharp, errors caused by interpolation over missing solutions are large. When the wind is directed perpendicular to broadside (shore-parallel case) the SNR is decreased near the jet region and an increase in error, relative to the wind parallel to broadside case, is observed. Away from the jet region, where changes of current are more gradual, errors caused by interpolation over missing solutions are smaller, and no significant dependence of error on the changes in SNR due to wind direction is observed.

4.6.3 Effect of Irregular Sea Echo Amplitude

We next investigate the effect of an ocean surface that has a more dramatic variation in the strength of the HF echo from one region to another. This may occur in actual applications due to the shadowing effect of land masses over regions of the ocean surface within the radar coverage area. A simulation experiment was performed where for radar look angles greater than 0 degrees the sea echo amplitude was reduced, simulating a land shadow over the positive angle region. Errors obtained from 6 and 12 dB levels of shadowing were compared with the normal 0 dB shadowing case. The current profile used was a uniform current flowing parallel to shore, similar to the one shown in Figure 4. Using a radar operating frequency of 21.8 MHz, the simulation was run 30 times and the RMS error at each angle was calculated.

Resulting error dependence is shown in Figure 4.12. With beam forming, errors in the shadowed region are seen to increase with level of signal reduction in a manner consistent with the SNR dependence observed in Figure 5. With MUSIC, no increase in error is observed in the 6 dB shadowing case, but in the 12 dB case an increase in error is observed. Examination of the angular coverage (Figure 4.13) shows the number of solutions obtained at each angle over the

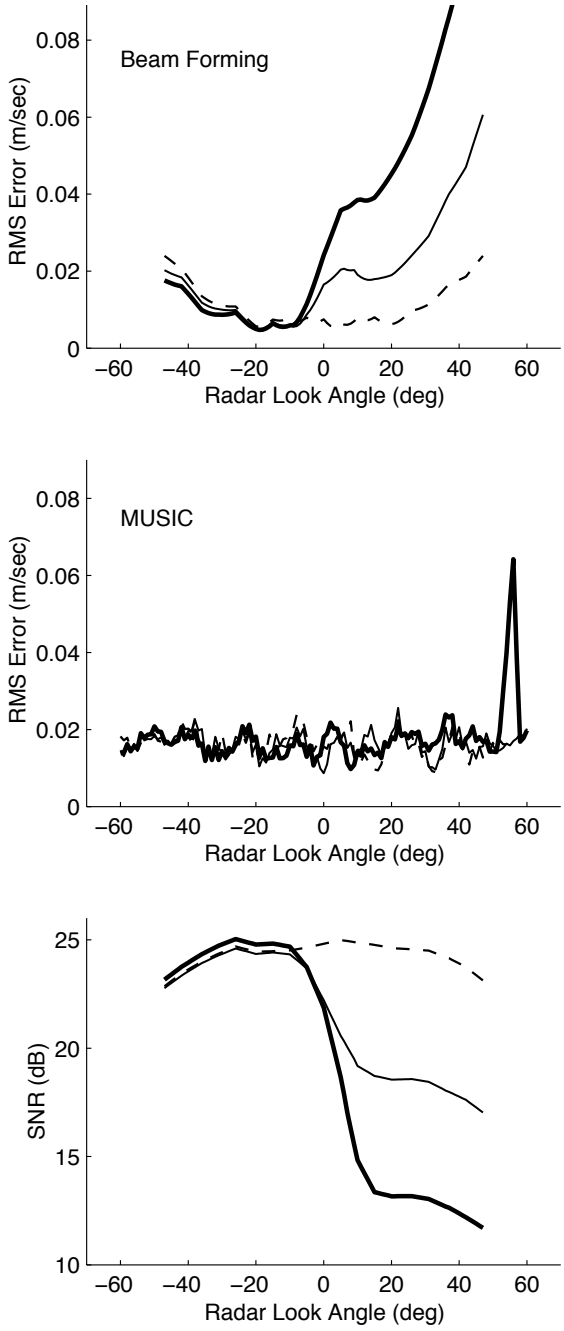

Figure 4.12: Error as a function of look angle for beam forming (top) and MUSIC (center) processed currents from 21.8 MHz data with an abrupt change in SNR over the coverage area, shown in the bottom panel. The sea echo was reduced over the positive look angle region by 12 dB (thick line), 6 dB (thin line) and no signal reduction (dashed line). (The large spike in error with MUSIC processing at about 55 degrees is present only in the 12 dB reduced signal case.)

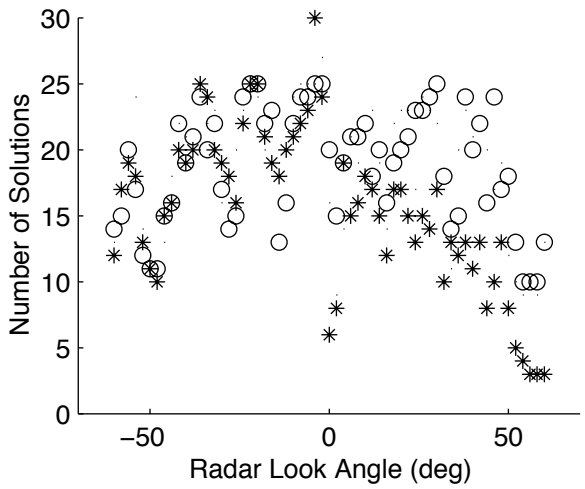

Figure 4.13: Number of solutions obtained using MUSIC processing as a function of look angle for the case of an abrupt change in SNR over the coverage region. Solutions at each angle were summed over 30 simulation runs for the 12 dB shadowing case (star) and 0 dB shadowing case (circle). The plot shows that lower coverage was obtained in the low SNR in region. The simulation used a radar operating frequency of 21.8 MHz.

30 simulation runs for the 0 and 12 dB shadowing cases. A decrease in the number of solutions over the shadowed region is observed in the 12 dB shadowing case.

4.6.4 Current Jet Analysis

The next effect investigated involves the dependence of error on the sharpness of changes in the radial current profile. A current profile similar to the one used to examine wind effect (Figure 4.10) was used, but here the jet width and magnitude were varied. The jet magnitude was varied from 0.05 to 0.64 m s^{-1} while the jet width was held constant at 12 degrees, then the jet magnitude was held constant at 0.45 m s^{-1} while the width was varied from 6 to

42 degrees. Since error was expected to be proportional to the sharpness of changes in the radial current profile, and inversely proportional to the radar operating frequency, the problem was simplified by examining algorithm performance in terms of a sharpness to resolution ratio defined by

$$\Gamma \equiv \frac{V}{Wf}, \tag{4.14}$$

where V is the jet magnitude in m s^{-1}, W is the width of the jet at half maximum in units of degrees, and f is the radar operating frequency in Hz. The RMS error over the region of the jet was averaged over 30 simulation runs to reduce statistical uncertainty and plotted against this parameter. Results, shown in Figure 4.14, clearly indicate a positive correlation between the parameter Γ and the RMS error, and therefore demonstrate the equivalence of current feature sharpness and radar operating frequency in the determination of current measurement error. Further, results show that errors with MUSIC are lower than those with beam forming over most of the range of current profile and frequency parameters investigated here.

4.6.5 Effect of Averaging Subsequent Measurements

We next examine the effect of averaging measurements. The same current profile used in the wind and current jet analysis sections (Figure 4.10) was used here. Since errors with beam forming are generally due to beam width and side lobes, no improvement is expected from averaging beam formed measurements. With MUSIC, however, we expect at least some component of the error to be random, and that the random component will be reduced by averaging. The simulation was run 60 times, and the data processed using both MUSIC and

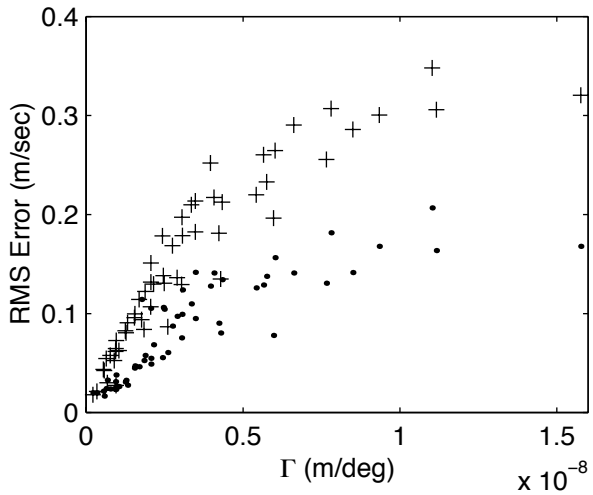

Figure 4.14: RMS error as a function of the ratio of current profile sharpness over radar operating frequency, Γ. RMS errors were computed over the region of the jet-like feature characterized by Γ for both beam forming (plus) and MUSIC (dot) processing. Errors are roughly proportional to Γ and are generally lower with MUSIC than with beam forming over most of the parameter space examined.

beam forming. Current measurements from N data sets were then averaged for values of N ranging from 1 to 60. As expected due to the systematic nature of the sources of error, no improvement was obtained by averaging beam formed measurements. Error in MUSIC processed measurements was found to decrease with averaging for small values of N. The results with MUSIC processing for the highest and lowest radar frequencies over the range of $N = 1$ to 15 are plotted in Figure 4.15. Error in MUSIC processed measurements is seen to follow the $1/\sqrt{N}$ dependence expected for purely random errors out to roughly $N = 3$ for 4.8 MHz, and $N = 6$ for 21.8 MHz, after which a systematic error component takes over, and little is gained by further averaging.

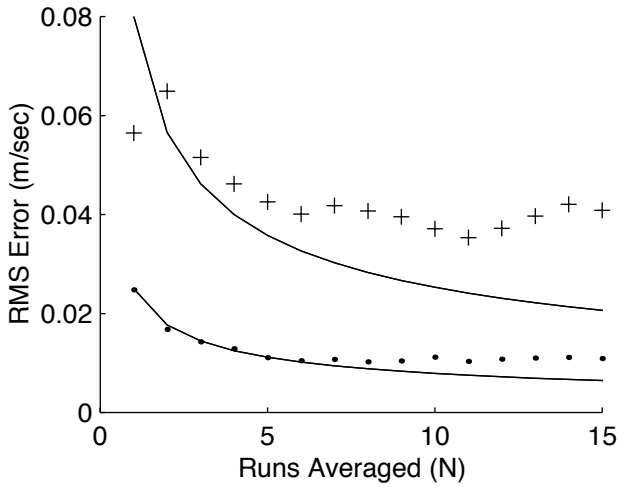

Figure 4.15: RMS error over the region of a jet-like feature as a function of the number of measurements averaged. Results for 21.8 MHz (dot) and 4.8 MHz (plus) are compared to the $1/\sqrt{N}$ dependence (solid lines) expected for purely random errors.

4.7 Conclusions

A simulation has been developed to compare the performance of beam forming and direction finding algorithms in the extraction of ocean surface currents from HF radar data. In this study the MUSIC direction finding algorithm was used. Algorithms were compared over variations in several ocean surface parameters including SNR levels, wind direction, irregular sea echo amplitude and relative sharpness of changes in the current profile. The effect of averaging of measurements was also investigated.

Investigations into the dependence of error on SNR show beam forming to have a greater dependence on SNR than MUSIC, particularly at the higher frequencies of operation, and give an estimate of the SNR required for a desired RMS error. Results show MUSIC errors to be independent of SNR for the current profile used and range of SNR covered in the

experiment. Investigations into the effect of wind direction, which is responsible for gradual variations in SNR as a function of look angle, showed (with beam forming) an increase in error when the wind is aligned perpendicular to the radar look angle. An increase in error for wind direction perpendicular to look angle was also observed with MUSIC, but the increase was not as pronounced. A more radical example of spatial variation in SNR was investigated with the simulation of a shadowing effect. This experiment revealed an increase in errors with beam forming over the shadowed (low SNR) region that was proportional to the degree of shadowing. With MUSIC, a reduction in the number of solutions obtained was observed in the shadowed region relative to the unshadowed region, leading to increased error in the extreme (12 dB) shadowing case.

Analyses of errors associated with a sharply varying current feature (simulating a current jet) involved combining the ocean parameters characterizing the jet with the radar operating frequency. Results show that the sharpness of changes in the radial current profile and the radar operating frequency are in some sense equivalent in their effect on errors in current measurement. Further, results show MUSIC to have lower errors over most of the frequency and current profile sharpness parameter space probed. Finally, investigations into the effect of averaging showed no improvement with beam forming analysis (as expected from the systematic nature of the errors) but did show that about a factor of two improvement can be obtained by averaging MUSIC results. Simulation methods presented here have been valuable in modifying the MUSIC algorithm for use with HF radar systems and understanding the sources of error in HF radar current measurements.

Chapter 5

HF Radar Observations of Surface Currents: Internal Consistency and Comparisons With In Situ Measurements

Due to the lack of relevant ground truth, it is difficult to estimate the accuracy of surface current measurements obtained from HF radar systems. We have addressed this problem through simulation analysis in Chapter 4 and in this Chapter we re-examine the problem using real data. First, we compare radar-derived ocean current measurements obtained using different radar operating frequencies and processing methods to evaluate the consistency of the results, estimate the magnitude of the random variations and investigate evidence of systematic

differences in the radar measurements. Second, we compare radar measurements with ADCP current measurements to evaluate the accuracy of the radar measurements for the MCR's four operating frequencies and the two different processing methods, beam forming and direction finding. Because of our interest in investigating the effect of wave interaction and wind forcing on near-surface ocean currents, we focus our attention on data from the time period overlapping the availability of high resolution directional wave energy spectral data and three dimensional wind turbulence measurements from the NPS Flux Buoy described in section 3.3.2.

5.1 Spatial and Temporal Coverage of the HF Radar-Derived Ocean Current Data

Time series of the sea echo at the MCR's four operating frequencies was recorded hourly at each of the two MCR sites (locations shown in Figure 1.1). The data was collected from the two sites and processed using both beam forming and MUSIC direction finding methods to produce radial current measurements. Gaps in the data set occurred for several reasons. There were times when the radar systems were shut down either for service, upgrades or repair, or because of power outages. Also, there were times when the radar systems were not operating or operating poorly due to component failure or problems with the operating software. Even when the system is operating optimally, the extent of the coverage area depends on the height of the Bragg resonant waves, the propagation loss over the ocean surface, the background noise level and the strength of interference signals. In the case of MUSIC processing, the coverage was, at times, sparse or patchy due to limited SNR, antenna pattern effects, or features of the

currents themselves. For instance, if the radial component of the current is nearly constant over large angular regions in a given range cell, then MUSIC will produce few angular solutions and the coverage will appear patchy. Since this effect is associated with nearly constant currents, little error would be introduced by interpolating to fill in gaps due to this effect. However, in our analysis we did not attempt to fill gaps by interpolation. Examples of the radar coverage obtained using beam forming and MUSIC processing for the month of September, 1999 and corresponding to the region surrounding the location of the ADCP at the MBARI mooring, M1, are shown in Figure 5.1 for the lowest frequency of operation, and in Figure 5.2 for the highest. The fraction of the time that current measurements were obtained over the coverage area was much higher with beam forming than with MUSIC processing, particularly at the lowest frequency, 4.8 MHz. It is apparent, however, that not all of the beam forming results are meaningful. For instance, at the lowest frequency, many current measurements appear over land. Beam forming processing produces a solution whenever the SNR for a given range and bearing is sufficient. At 4.8 MHz the beam width (see Figure 4.1) is about 50°. So, even when the centroid of the beam is directed over land, large areas of the ocean surface still contribute to the radar echo. At the highest radar frequency, 21.8 MHz, the width of the formed beam is about 15° and the number of solutions over land was greatly reduced. Interpreting the 4.8 MHz current measurements is difficult because of the large beam width. There are really only a couple of independent current measurements in each range bin. In the MUSIC results, relatively few currents appear over land, indicating that directional resolution is fairly good even at 4.8 MHz. In addition to the fact that the temporal coverage was lower with MUSIC than with beam forming,

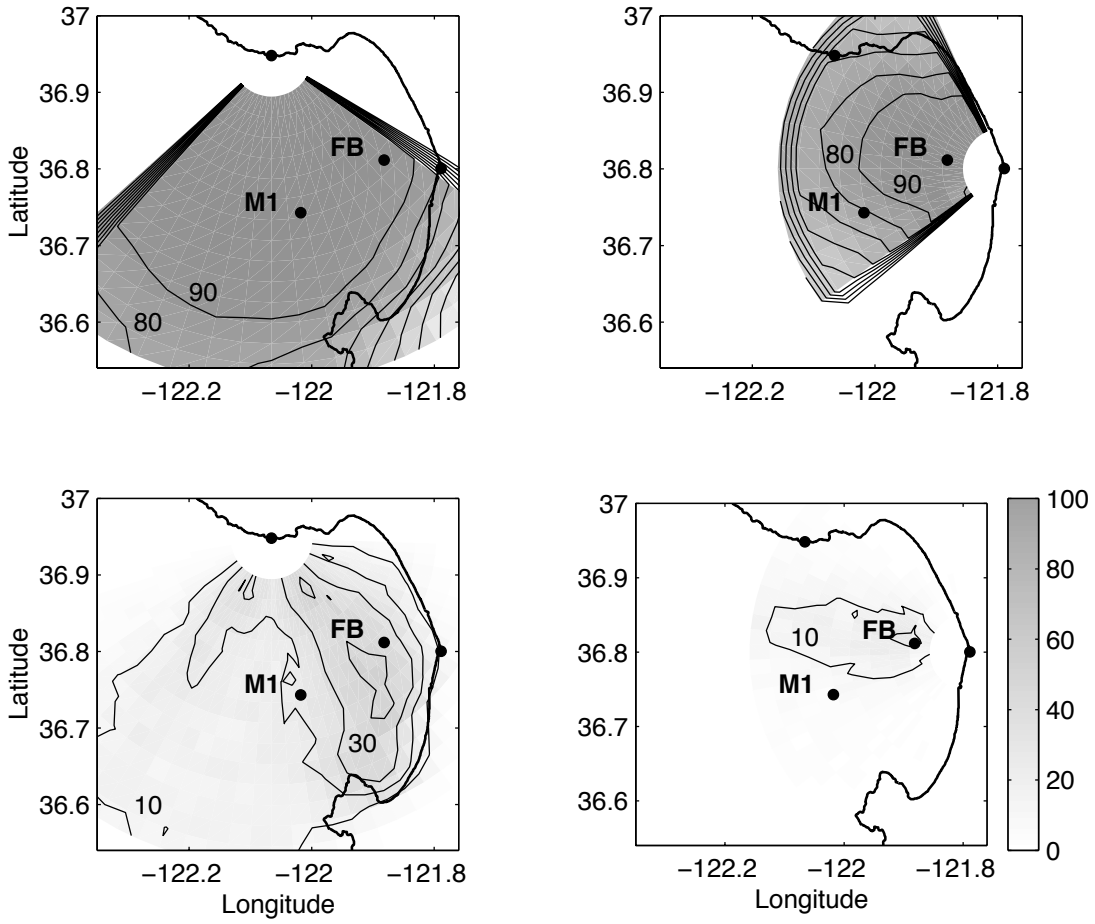

Figure 5.1: Plots of Monterey Bay showing the radar coverage obtained as a percentage of hours for which HF radar ocean current measurement data was available for the month of September 1999, for the lowest radar frequency of operation (4.8 MHz). Location of the moorings MBARI M1 (M1) and the Flux Buoy (FB) are indicated by the solid circles in the coverage area. Coverage for the northern site at Long Marine Lab (LML) is shown in the left column, and coverage from the southern site at Moss Landing Marine Lab (MLML) in the right column. The top two plots show the coverage obtained using beam forming processing and the bottom two plots show the coverage obtained using MUSIC. The site locations are indicated by the dots on the coastline. Percent coverage is indicated both by the shading and by contour lines at intervals of 10 %. Numbers placed near the contour lines denote the percent coverage indicated by the corresponding line.

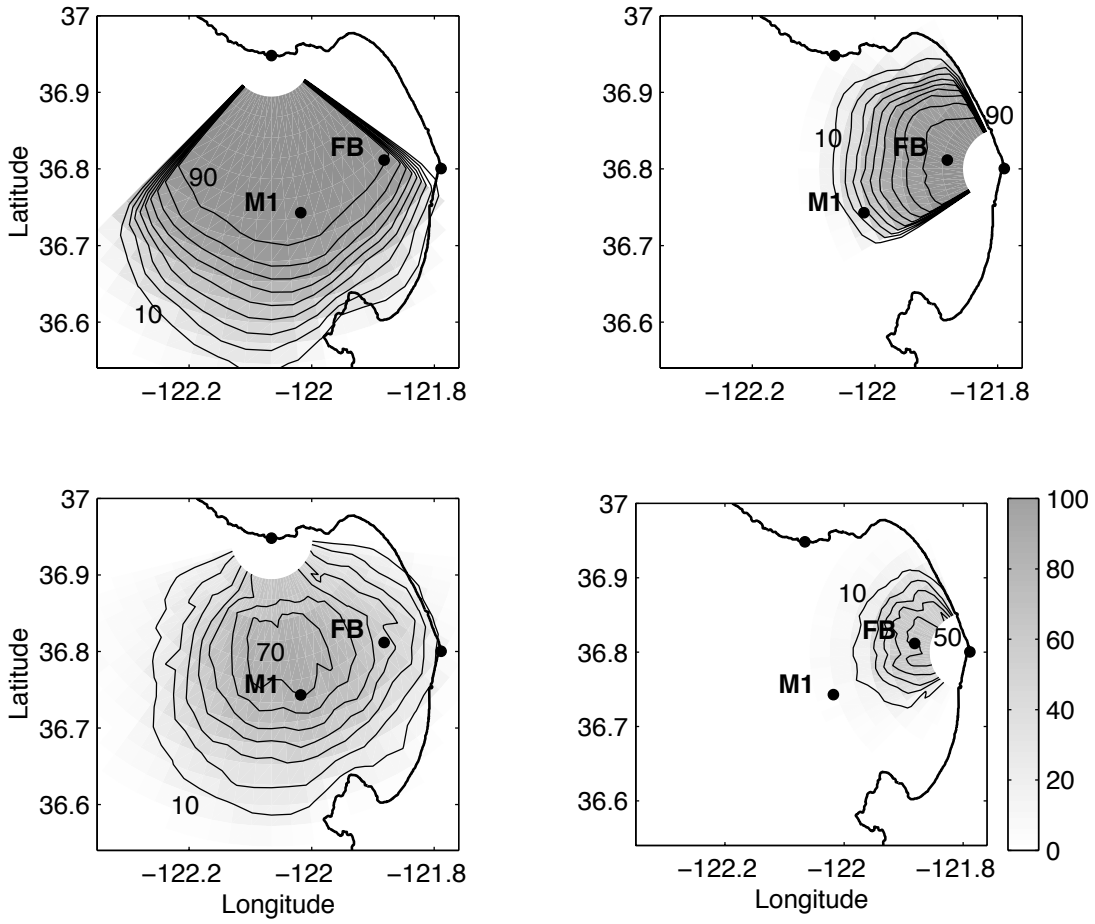

Figure 5.2: Plots of Monterey Bay showing the radar coverage obtained as a percentage of hours for which HF radar ocean current measurement data was available for the month of September 1999, for the highest radar frequency of operation (21.8 MHz). Location of the moorings MBARI M1 (M1) and the Flux Buoy (FB) are indicated by the solid circles in the coverage area. Coverage for the northern site at Long Marine Lab (LML) is shown in the left column, and coverage from the southern site at Moss Landing Marine Lab (MLML) in the right column. The top two plots show the coverage obtained using beam forming processing and the bottom two plots show the coverage obtained using MUSIC. The site locations are indicated by the dots on the coastline. Percent coverage is indicated both by the shading and by contour lines at intervals of 10 %. Numbers placed near the contour lines denote the percent coverage indicated by the corresponding line.

variations in coverage over the region are apparent.

Due to equipment problems that led to poor SNR during the period of interest, the coverage obtained from the MLML site using MUSIC processing was very poor. Because of the poor temporal and spatial coverage at MLML, it was not possible to combine the radial currents measured from the two sites and produce a useful full vector data set. In the case of the beam forming processed data, full vector solutions could be computed, but because of the large beam width, the result would be difficult to interpret at the lower frequencies. For both processing methods, the coverage at the furthest range bins was reduced relative to the lower frequency results due to greater propagation losses at the higher frequency. Because of the lack of data from the MCR system located at MLML, the results discussed throughout the rest of this work rely solely on the radial current measurements from the MCR deployment at LML for the radar-derived ocean current measurements.

Gaps in coverage and limitations in range for both beam forming and MUSIC processing methods occur due to limitations in SNR. During processing, SNR criteria were applied to prevent derivation of current measurements from noise-dominated spectral regions. To compute the SNR during beam forming processing, the power of each of the approaching and receding Bragg peaks was measured by taking the mean of the power spectral density over five frequency bins centered about the previously determined centroid of each of the Bragg peaks in the Doppler spectrum. If the results were within three dB of each other for the two peaks, the mean of the two results was used for the power of the measurement and the measured current was taken to be the average of the current derived from the position of each of the peaks. If the

difference was greater than 3 dB, then the SNR of the larger of the two peaks was taken to be the SNR of the measurement and the smaller peak was not used to estimate the current magnitude. The noise power was measured by calculating the mean spectral power over a section of the spectrum one-eighth of the spectrum wide. The location of the section was swept across the total width of the spectrum and the lowest result was taken as the noise level. If the SNR of a given measurement was below six dB, the measurement was rejected.

During MUSIC processing, the determination of the width and location (in frequency space) of the Bragg region was performed on the basis of SNR as described in section 4.5. In the case of a spectrum with low SNR, the width of the region of the spectrum determined to contain sufficient Bragg resonant energy for current processing is reduced, generally eliminating solutions for larger magnitude currents and resulting in sparser coverage. In addition, if the spectral power density of a point inside the Bragg region was less than five dB above the noise level, then the point was not processed. Figure 5.3 shows the MCR data coverage time-lines of available data for the period September through November, 1999. Also shown in the figure are the periods of available ADCP data from the MBARI M1 mooring and high resolution directional wave spectral energy data from the NPS flux buoy. Gaps in the time-lines indicate 24 hour periods for which less than 50 % of the hourly data were available. In the case of the MCR radial current measurements, the time-lines correspond to data from a region of the ocean surface surrounding the M1 Buoy where the ADCP was located. For the LML site, this region was at a range of 21 km and an angle of 170° true north. For the MLML site, the range was approximately the same and the angle was 257°. In both cases the angle was within 30°

of the receive antenna's broadside direction. The time period for which ADCP data from the mooring M1 and high resolution wave energy directional spectra from the flux buoy mooring were available is of greatest interest. It is clear from the time-lines that, of the radar data, the LML data set is the most complete and that, although the temporal coverage is more consistent with beam forming, there are gaps in both the beam forming and MUSIC processed data.

5.2 Consistency of Radar Measurements and Comparison with ADCP Measurements

5.2.1 Comparisons of HF Radar Current Measurements at Different Radar Frequencies

Although the different radar frequencies sample the current at different depths, we expect that the differences in radial current magnitude between current measurements obtained using different radar frequencies should be small relative to the variations in the currents themselves. We also expect currents due to forcing at the surface to decay with depth. The measurements of the currents at different frequencies should therefore be correlated, and since the higher frequencies sense the current over a region closer to the surface, current measurements from the higher frequencies are expected to be stronger in magnitude than those from the lower frequencies. Time series of the current measurements from the MCR system located at the LML site, corresponding to the region surrounding the mooring M1 and derived using MUSIC processing, are shown in Figure 5.4. It can be seen from the time series that the major features

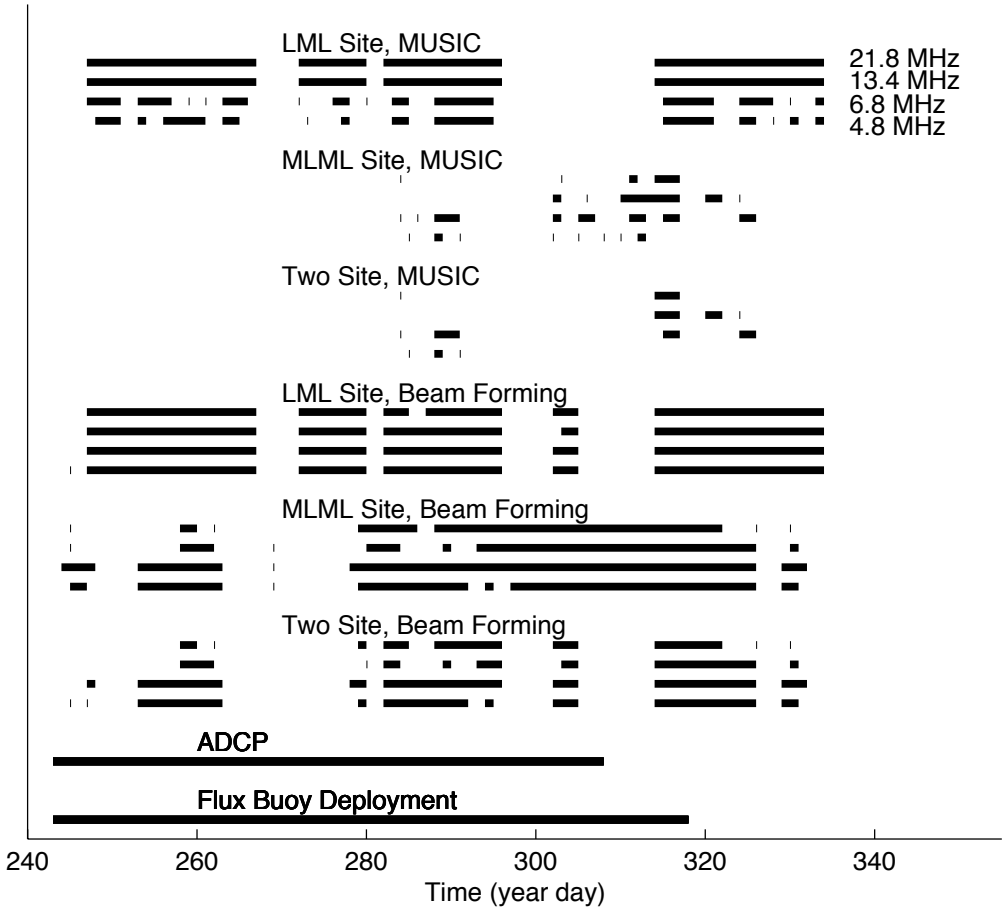

Figure 5.3: Times during the period of interest for which HF radar data was collected and had sufficient signal-to-noise ratio for current processing. MCR data correspond to the region surrounding the MBARI M1 buoy, approximately equidistant from the two radar sites, at a range of about 21 km. Each set of four lines correspond to the same four frequencies of operation as indicated for the top set. Availability of high resolution directional wave spectral energy data recorded by a flux buoy and ocean current measurement data from an ADCP are included near the bottom of the plot.

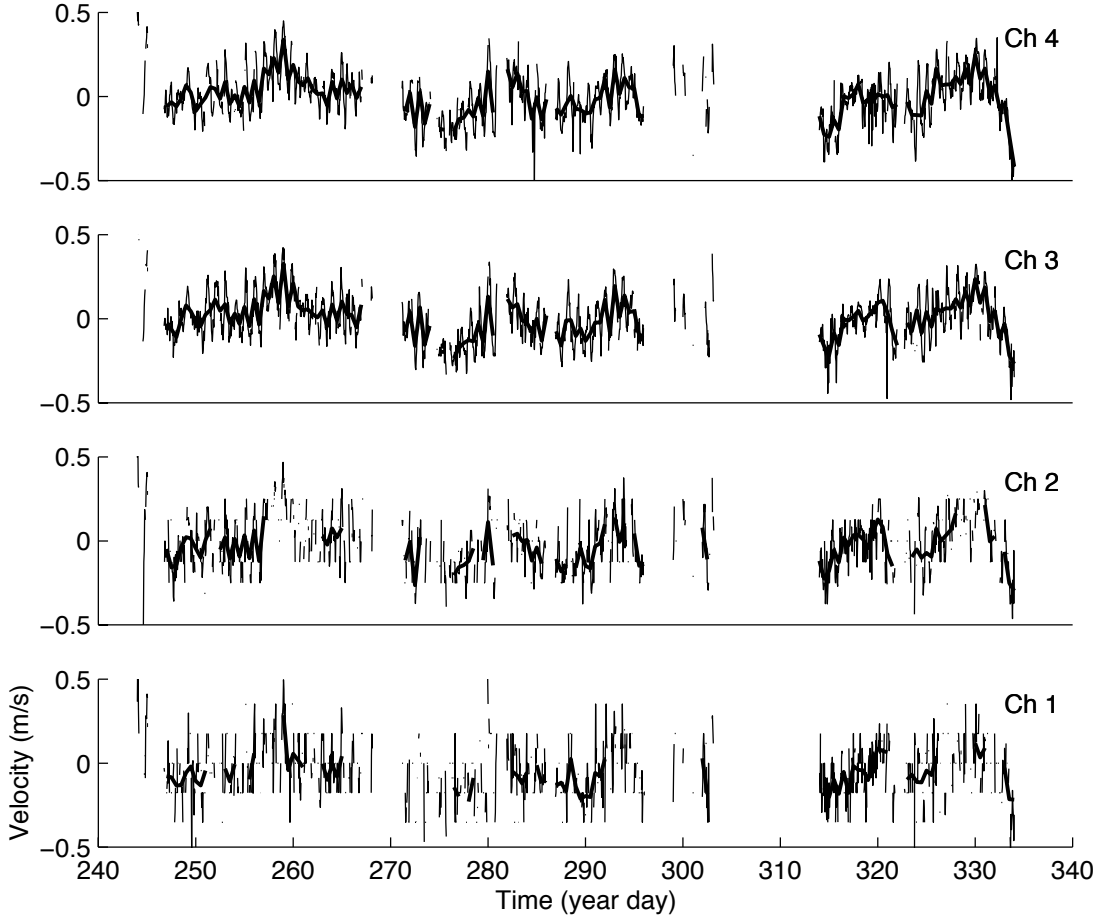

Figure 5.4: Time series of radial currents measured from the MCR deployment site located at LML. Results were obtained using MUSIC processing. Hourly recorded measurements (thin line) and 12 hour averages (thick line) are shown on the plots.

in the currents are similar for each of the different operating frequencies used. Spectral analysis of the time series was not performed because of the gaps in the data, but the dominant period of the variations in the hourly currents was estimated by visual inspection of about ten days of data to be approximately 23 hours, or roughly equal to the 24 hour period expected for the land sea breeze. Similar periodic signals have been observed before in the radar currents examined by Paduan and Rosenfeld (Paduan & Rosenfeld, 1996). Although the averaged data show a reduction in variance, averaging is expected to increase the accuracy of the radar current measurements by reducing random errors and random variations in the measured currents due to the variability in the currents themselves over the spatial extent of the measurement. A period of twelve hours was selected so as to help isolate the wind-induced and wave-induced currents from the tidal currents.

Plots of radial currents measured at radar operating frequency f_n verses radial currents measured at radar operating frequency f_4, where the frequencies, f_n, were the three lower operating frequencies of the MCR, $f_1 = 4.8, f_2 = 6.8, f_3 = 13.4$ and the frequency $f_4 = 21.8$ MHz, are shown in Figure 5.5, for both MUSIC and beam forming processing methods, using 12 hour averaged data. In the case of the MUSIC processed results, the radials have been spatially averaged over 10 degrees of azimuth to reduce the incidence of gaps in the times series and to reduce random errors and variations. The beam formed results are effectively averaged over the beam width corresponding to the given frequency.

A linear regression analysis using the method of least squares was performed assum-

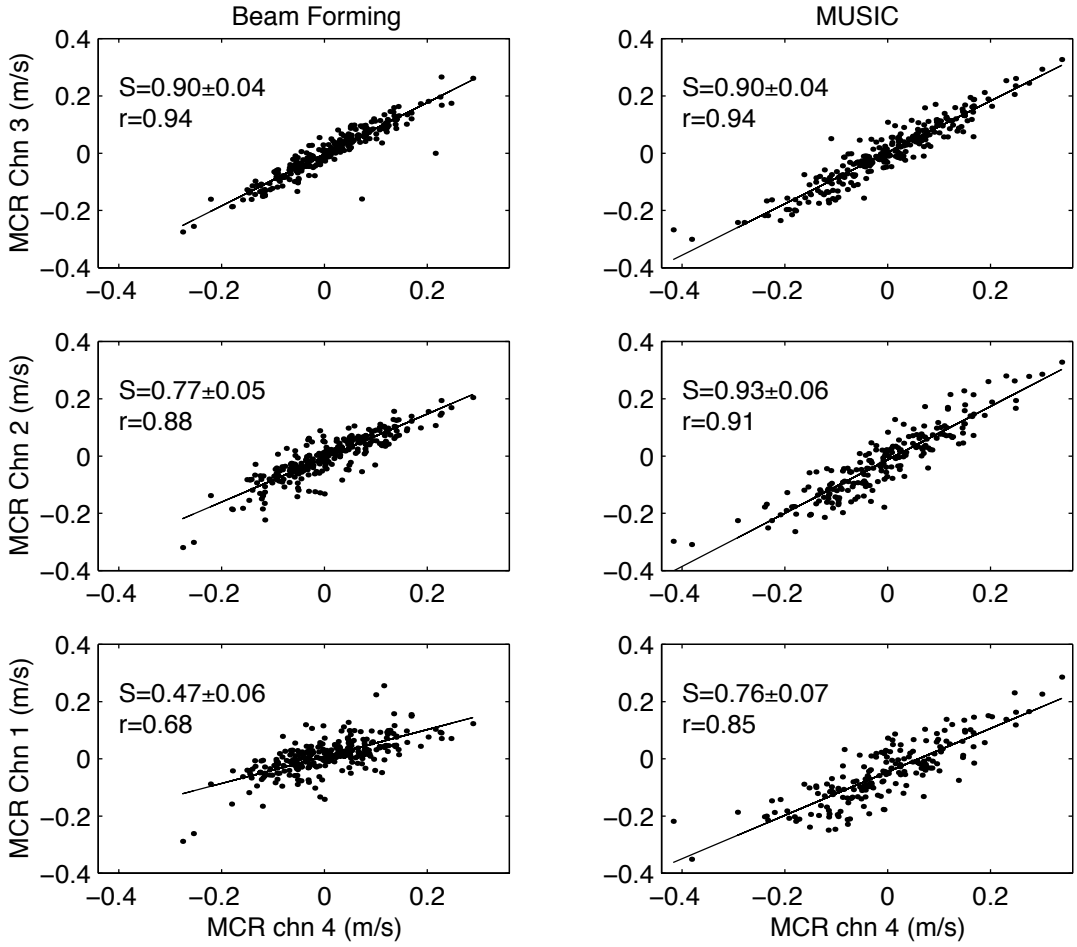

Figure 5.5: Plots of HF radar radial ocean current measurements corresponding to pairs of radar frequencies. From top to bottom, radial currents from radar channels 1 (4.8 MHz), 2 (6.8 MHz) and 3 (13.4 MHz) are plotted against radial currents from radar channel 4 (21.8 MHz). Beam forming processed results are in the left column and MUSIC results in the right column. A linear best fit to the data (solid line) along with the correlation coefficient (r) and the slope of a linear fit to the data (S) are included on each plot.

ing the functional form,

$$\hat{u}_n = b_1 u_4 + b_0, \tag{5.1}$$

where $\hat{u}_n$ is the model for the current measured at the three lower frequencies, f_n, and u_4 is the current measured at the 21.8 MHz frequency. The slope b_1, along with the uncertainty in the slope, were computed for each plot. The uncertainty in the slope was taken to be the 95 % confidence level assuming normally distributed random errors, $2s_b$, computed by

$$s_b^2 = \frac{s_{xy}^2}{\sum x^2} \tag{5.2}$$

and

$$s_{xy} = \left(\frac{1}{N-2}\right) \sum_{i=1}^{N} (y - \hat{y})^2, \tag{5.3}$$

where $y = u_n$, $x = u_k$ and $\hat{y} = \hat{u}_j$. In the case of the comparisons involving the highest two frequencies (13.4 MHz results plotted as a function of 21.8 MHz results) the beam forming and MUSIC processed results are very similar. The random variations about the linear fit are larger with MUSIC, but the total variation in measured currents is also larger and the correlations are equal. Both the larger magnitude of the measured currents and the higher random variation observed are in agreement with the predictions of the simulation results of Chapter 4.

With the beam formed results, both the correlation coefficient and the slope of the linear fit decrease with frequency. This is consistent with the expected effect of a reduction in current magnitudes with depth, but it is also consistent with the effect of a reduction in measured current magnitude due to averaging over larger beam widths at lower frequencies. In the MUSIC processed results, a decrease in correlation coefficient with frequency is observed but it is not as rapid as the decrease seen in the beam formed results. The lowest value of the

f_n (MHz)	Processing method	$\Delta\theta$ (deg)	N	r	δ_n (cm/s)	Slope
13.38	Beam Forming	24	267	0.94	2.96	0.90 ± 0.04
13.38	MUSIC	24	255	0.95	3.45	0.877 ± 0.037
13.38	MUSIC	10	257	0.94	3.57	0.90 ± 0.04
6.78	Beam Forming	44	268	0.88	3.82	0.77 ± 0.05
6.78	MUSIC	44	248	0.90	4.56	0.824 ± 0.050
6.78	MUSIC	10	206	0.91	4.84	0.93 ± 0.06
4.80	Beam Forming	56	268	0.68	4.54	0.47 ± 0.06
4.80	MUSIC	56	247	0.78	4.82	0.508 ± 0.053
4.80	MUSIC	10	182	0.85	5.77	0.76 ± 0.07

Table 5.1: Statistical results of the comparison between HF radar derived currents measured using different frequencies and processing methods. The column labels indicate the following: f_n, the radar frequency used for computing currents for the y axis of the plots in Figure 5.5, $\Delta\theta$, the beam widths, in the case of beam forming, or the selected averaging widths, in the case of MUSIC processing, N, the number of data points, r, the correlation coefficient, δ_n, the error relative to the linear fit and Slope, the slope of the linear fit.

slope of the linear fit is seen with the lowest frequency, but the highest slope value is actually seen with the middle frequency result, 6.8 MHz, and the slopes of both the 6.8 and the 4.8 MHz frequency results are higher than those observed with beam forming at the same frequencies.

If the relationship between the actual currents at the depths corresponding to the radar current measurement depth for the various pairs of radar frequencies is well represented by a linear dependence as assumed, then the correlation coefficients indicate that MUSIC processing gives a more accurate measurement of the current for the pairs of frequencies examined. The results also suggest that the decrease in slope with frequency that is observed in the beam forming results is primarily due to increased beam width at the lower frequencies rather than an actual reduction of current with depth. A summary of the correlation coefficients and the slope values and their estimated uncertainties are given in Table 5.1.

The error estimate, δ_n, given in table 5.1, is derived from the deviation of the mea-

sured values used for the dependent variable from the linear best fit to the data. With the assumption that the deviations from the linear fit are independent, normally distributed random values with constant variance, 50 % of the time values are expected to fall within $\pm\delta_n$ of the linear fit. Estimation of error in current measurement at a given radar operating frequency, f_n, from these results is complicated by the fact that both quantities being plotted contain error. The quantity δ_n, given the assumptions on the statistics of the random errors, can be expressed in terms of the the root mean square (RMS) errors in the current measurement σ_n and σ_4, made at frequencies f_n and f_4, respectively, by

$$\delta_n = \sqrt{\sigma_n^2 + \sigma_4^2}\,. \tag{5.4}$$

We expect that the error is lowest for the highest radar frequency and so solve for σ_n by making the simplifying assumption that σ_4 can be related to σ_n by

$$\sigma_4 = \sigma_n \frac{f_n}{f_4}. \tag{5.5}$$

This relation is somewhat empirical but supported by the simulation results of Section 4.6.4 that showed rough agreement with a linear increase in RMS error in current measurement with radar operating frequency. It is also consistent with the reduced current speed resolution expected at lower frequencies. Combining the two equations above, the value of σ_n was computed for each of the plots in Figure 5.5 and the values are tabulated in Table 5.2. Since actual variations in the currents measured at the different frequencies may have accounted for some of the measured variation from the linear fit, the error estimates obtained using this method are an upper bound on the random errors in the measurements. The estimates, however, may not include systematic errors in the measurements that are common to pairs of frequencies.

Frequency (MHz)	Error Estimate (σ_n) Beam Forming cm/sec	MUSIC cm/sec
21.8	1.55	1.87
13.4	2.52	3.04
6.8	3.65	4.62
4.8	4.65	5.63

Table 5.2: Estimates of RMS random errors for beam forming and MUSIC processed current measurements corresponding to the region surrounding the M1 buoy, from the radar site at Long Marine Lab. Estimates are based on deviations from a linear fit to plots of currents measured using pairs of frequencies and do not include systematic errors. Current measurements were averaged over 12 hour periods.

To test the hypothesis that the decrease in slope observed in the plots of the beam forming processed results was due to averaging over beam width, we averaged the MUSIC processed currents spatially over an angular width equal to the expected beam forming beam width for each frequency. The results are plotted in Figure 5.6. For the lower two frequencies, the slope values found with the averaged MUSIC results agreed with the results with beam forming within the statistical uncertainty of the slope estimation. Exact agreement was not expected since the averaging window in the beam forming case is only approximated by the boxcar averaging window used for the MUSIC results. The results support the hypothesis that the variation in the slope in the beam formed results is due, at least in part, to averaging over beam width.

5.2.2 Comparison of HF Radar Ocean Current Measurements Obtained using Beam Forming and MUSIC Processing

To complete our inter-comparisons of radar-derived current measurements we now compare results between beam forming and MUSIC processed currents. In this analysis we

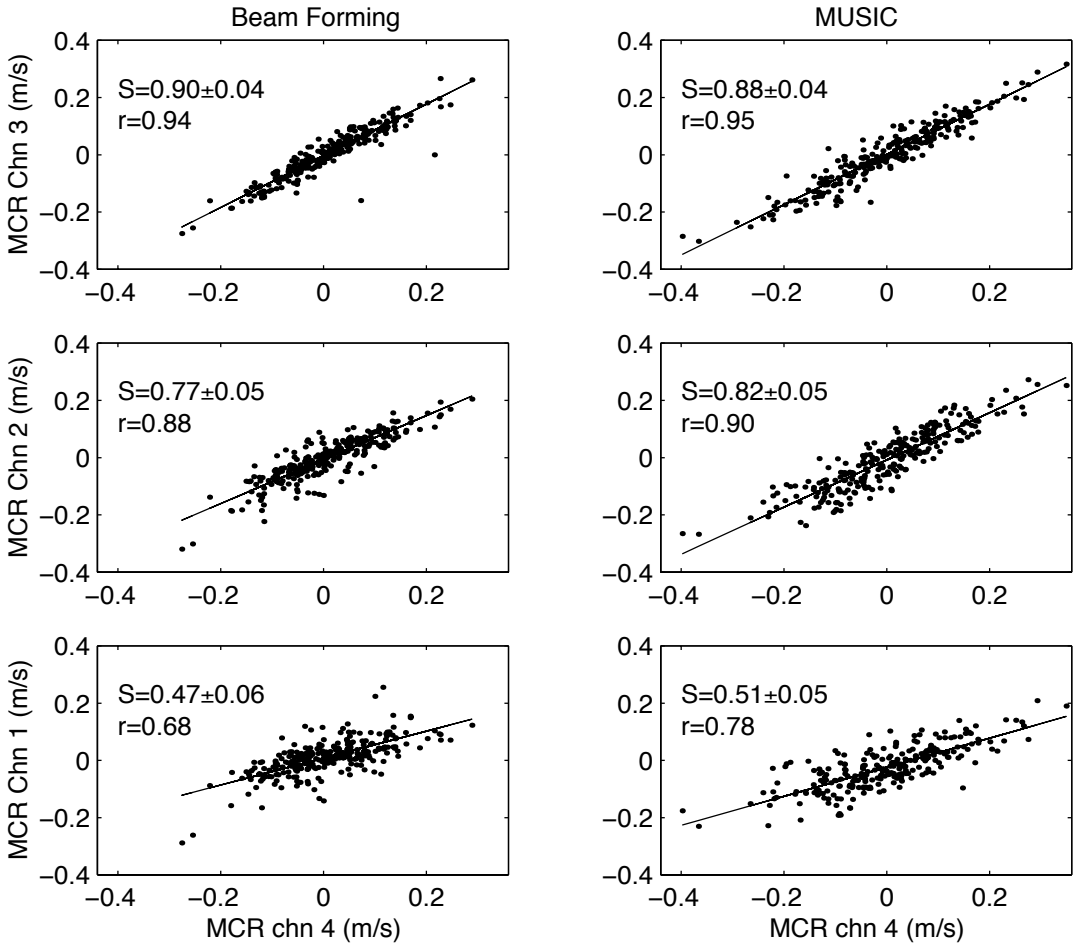

Figure 5.6: Plots of HF radar radial ocean current measurements corresponding to pairs of radar frequencies, where the azimuthal averaging of the MUSIC results (right column) was varied to match the expected averaging over beam width of the beam formed results (left column). From top to bottom, radial currents from radar channels 1 (4.8 MHz), 2 (6.8 MHz) and 3 (13.4 MHz) are plotted against radial currents from radar channel 4 (21.8 MHz). Beam forming processed results are in the left column and MUSIC results in the right column. A linear best fit to the data (solid line) along with the correlation coefficient (r) and the slope of a linear fit to the data (S) are included on each plot.

f (MHz)	N	r	δ (cm/s)	Slope
21.77	258	0.97	2.34	0.75 ± 0.02
13.38	256	0.95	2.60	0.76 ± 0.03
6.78	207	0.79	4.98	0.54 ± 0.06
4.80	183	0.53	5.18	0.30 ± 0.06

Table 5.3: Results of the comparison between 12 hour averaged, beam forming and MUSIC processed ocean current measurements. The column labels indicate the following: f, the radar frequency used for computing currents N, the number of data points, r, the correlation coefficient, δ, the error relative to the linear fit and Slope, the slope of the linear fit.

use 12 hour averaged current measurements and plot the results obtained using beam forming against those obtained using MUSIC processing. Plots for each radar frequency are shown in Figure 5.7 and results of the linear regression analysis are tabulated in Table 5.3. For the 13.4 and 21.8 MHz frequencies the results are very similar. The correlation coefficients are high, about 0.95, and the slope of the linear fit is seen to be about 0.75 in both cases, indicating that beam forming processed currents are about 25 % smaller than currents obtained using MUSIC processing under the conditions observed here. Over the full range of frequency the correlation coefficient is seen to decreases with frequency, as does the slope of the linear fit. At the 6.8 and 4.8 MHz frequencies, the currents obtained using beam forming are 46 % and 70 % smaller in magnitude than those obtained using MUSIC, respectively. Results for the RMS random error estimate, δ, show fairly good agreement with the results obtained from comparing measurements at pairs of frequencies, σ_n, (given in table 5.2) for all four frequencies.

5.2.3 Comparison of HF Radar and ADCP Ocean Current Measurements

In the preceding section we made internal comparisons between the MCR radial current measurements obtained using the four radar frequencies and processed with beam forming

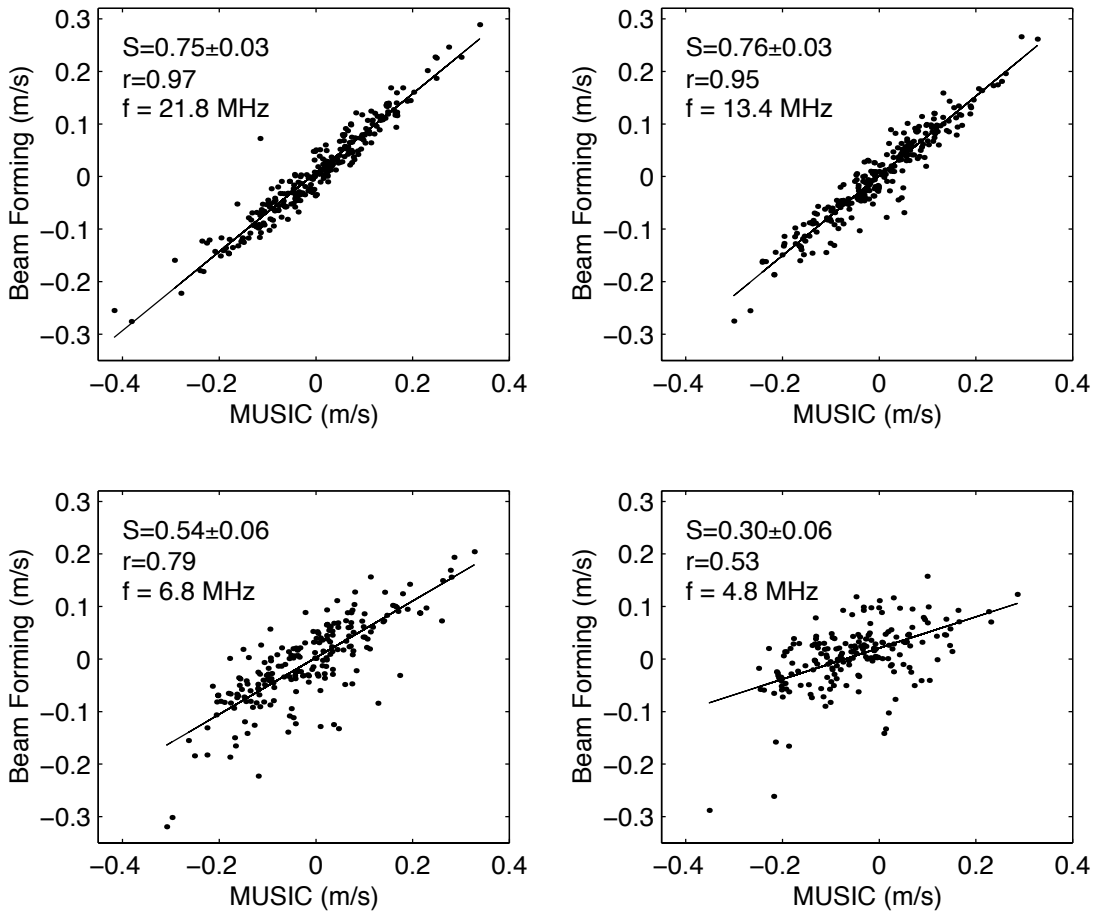

Figure 5.7: Comparison between beam forming and MUSIC processed HF radar ocean current measurements obtained using the MCR's four radar operating frequencies. Measurements correspond to the region surrounding the M1 buoy and were averaged over a 12 hour period. The MUSIC results were spatially averaged over 10° of azimuth. The beam formed results were effectively averaged over the width of the formed beam.

and MUSIC. All of the above comparisons were performed on measurements from a patch of ocean surface located in the vicinity of MBARI buoy M1 and averaged over 12 hours. We now compare the MCR radial currents with the current measurements from the top bin of the ADCP located at M1. Differences between ADCP current measurements and the radar current measurements are expected because of the differences in the spatial scales inherent in the measurement methods and the difference in the depth of the measurements. The radar measurement typically averages over tens of square kilometers and the measurement depth is estimated to be within the top few meters. In the case of the ADCP at M1, the depth of the top bin was 15.4 m and, relative to the scale of the radar measurement, the ADCP measurement is effectively at a point. In spite of these differences the ADCP measurements provide the best source of in-situ ground truth available.

The analysis used for this comparison is similar to that used for the inter-channel comparison of the preceding section. In this case, analysis is complicated by the fact that the ADCP measurements are full vector currents, whereas the radar data is limited to the radial component of the current. Since there may be a rotation of the current direction with depth, the component of the ADCP current measurement parallel to the direction of the radial current measurement may not be the proper component to correlate with the radar current measurement. To address this problem we computed the correlation coefficient between the radar-measured radial currents and the component of the ADCP current measurement parallel to an arbitrary reference angle. This was repeated for all angles, in one degree increments, and thereby the angle of greatest correlation, denoted θ_c, was determined. After obtaining the angle of the maximally

correlated component, we then performed a linear regression analysis using the maximally correlated component of the ADCP-derived currents and the radar-derived radial currents. With the MUSIC processed data, some spatial averaging was required to avoid excessive gaps in the temporal coverage. The MUSIC data were averaged over $\pm 10^o$. Since the beam forming results are averaged over the width of the beam, no additional spatial averaging was performed on the beam formed data. A time series of the MUSIC and beam forming processed radial currents, along with the correlated component of the ADCP current, for each of the four MCR operating frequencies is shown in Figure 5.8. The MCR data are averaged over 12 hr periods and correspond to the region surrounding the M1 buoy. It can be seen from the time series that, particularly for the higher frequencies, the radar-derived currents track the major features in the ADCP current measurements and that, particularly for the beam forming processed measurements, agreement worsens as the radar frequency decreases. Plots of the radar-derived currents verses the ADCP measured currents are shown in Figure 5.9 for the four radar operating frequencies and two processing methods.

In the 0 to 15 m depth regime we expect the currents to either be constant (barotropic, such as tides and density-driven currents) or to decay with depth (wind stress-driven or Stokes currents). The depth of the ADCP current measurement, about 15 m, is much deeper than the effective depths (0 to 3 m) of the MCR current measurements. The wind stress-driven currents and the Stokes currents are expected to be very small at the depth of the ADCP measurements and further reduced by the 12 hour averaging. They are not expected to play a significant role in the correlation between the ADCP and the MCR current measurements, aside from causing

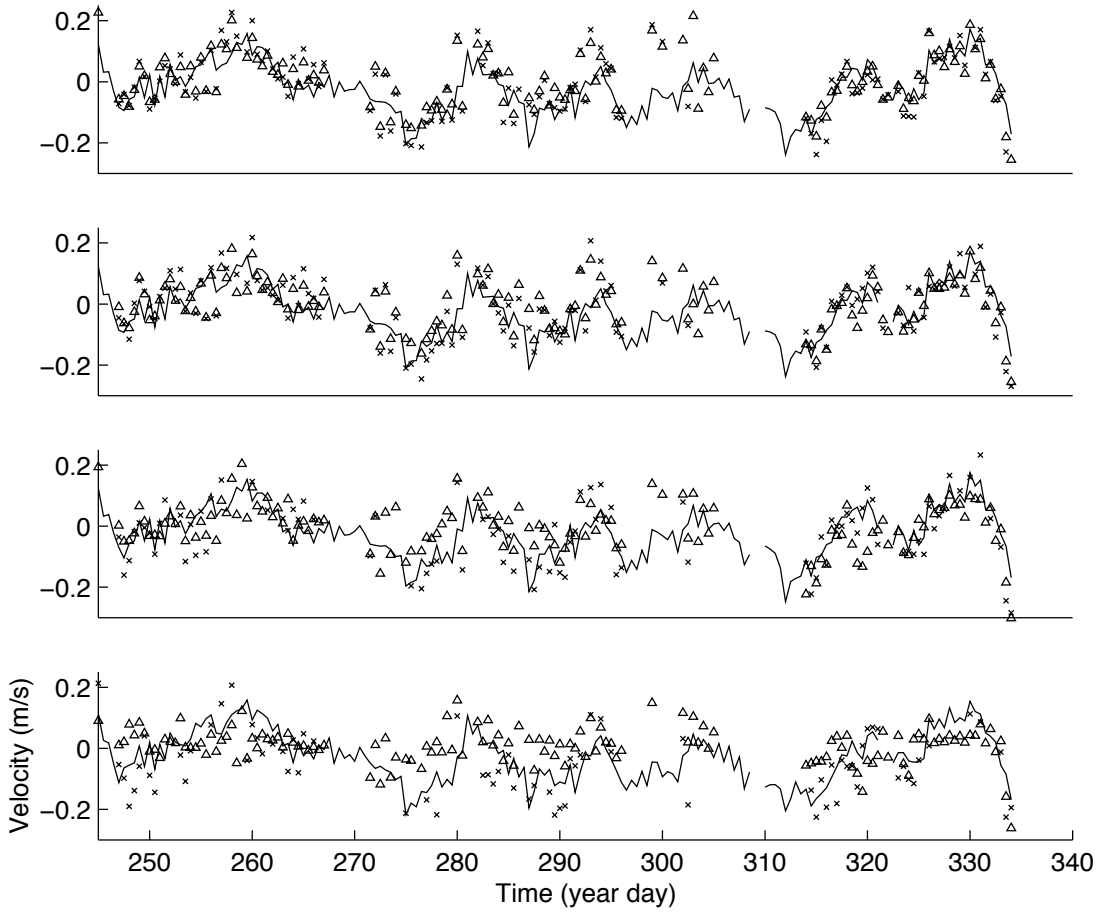

Figure 5.8: Time series of ADCP (solid line) and HF radar 12 hour averaged ocean current measurements. The radar measurements correspond to the region surrounding the location of the ADCP at the M1 mooring. From top to bottom the radar operating frequency used to obtain the measurements was 21.8, 13.4, 6.8 and 4.8 MHz. Results from both MUSIC (x) and beam forming (triangle) processing are shown.

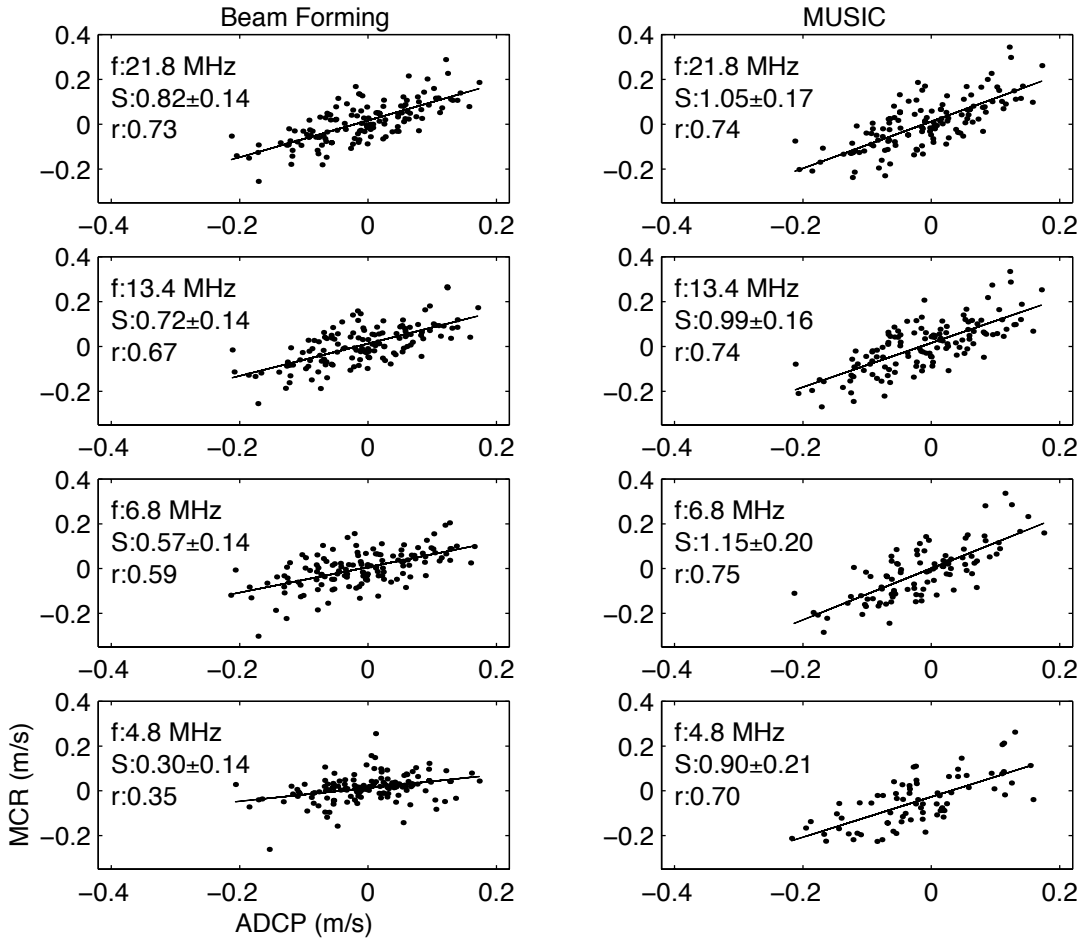

Figure 5.9: Plots of 12 hour averaged radar-derived ocean current measurements obtained using beam forming and MUSIC processing at each of the four radar operating frequencies as a function of the correlated component of 15 m depth, 12 hour averaged, ADCP currents from the M1 mooring. The linear best fit (solid line) along with the frequency (f), the slope of the best fit (S), and the correlation coefficient (r) are included on the plots.

scatter of the data points around the regression line.

In the beam forming results, the slope values decrease with radar frequency. This is apparently due to the averaging over the very large beam widths at the lower frequencies. Within the uncertainty of the slope estimation, the value of the slope is equal to one, for all four frequencies. For the highest frequency, the correlation coefficient calculated for the MUSIC results is about equal to that found for the beam forming results. In the beam forming results the correlations decrease sharply with radar operating frequency while in the MUSIC results they remain approximately constant. In both the beam forming and MUSIC results, the scatter about the linear fit is larger than that observed in the comparisons involving only radar data. Although there are differences between the ADCP and HF radar current measurement methods, in terms of the effective depth and spatial extent of the measurement, the data do support a proportionality between the MCR and the ADCP current measurements.

A summary of the statistical analysis of the results relating to the plots in Figure 5.9 is given in Table 5.4. The values for the rotation angle, θ_{rot}, defined by

$$\theta_{rot} = \theta_c - \theta_r, \tag{5.6}$$

where θ_r is the radar look angle that determines the direction of the radial component of the MCR current measurement, and θ_c is the angle of the maximally correlated ADCP current component, are listed in the table. The results for this rotation angle were positive, indicating a clockwise rotation between the radial current direction and the direction of the maximally correlated ADCP current component. In the beam forming results, the angle ranged from 11° to 20° for the three highest radar frequencies and showed a trend of decreasing angle with radar

frequency, possibly indicating a clockwise rotation in the near-surface region probed by the radar. The value corresponding to the lowest frequency was anomalously high but the correlation coefficient for that frequency was also lowest. In the MUSIC results, for the two highest frequencies, the results are in close agreement with the beam forming results and, with the exception of the 6.8 MHz frequency results, an overall trend of decreasing rotation angle with frequency is in evidence. Although these observations are interesting, we do not claim to have conclusively shown a clockwise rotation with depth in the near-surface currents or between the near-surface MCR measured currents and the deeper ADCP currents. The radial data available for this analysis are not as well suited for this purpose as full vector current measurements derived from two site radar data, and we have not evaluated the uncertainty in the determination of the angle of maximum correlation. We merely state that the results obtained are roughly consistent with the expectations of clockwise rotation of the current with depth, as observed in (Fernandez et al., 1996)

f_n (MHz)	Processing Method	N	r	$\theta_r - \theta_c$ (deg)	δ (cm/s)	Slope
4.80	bf	134	0.35	41.0	5.86	0.30 ± 0.14
6.78	bf	134	0.59	11.0	6.56	0.57 ± 0.14
13.38	bf	134	0.67	17.0	6.56	0.72 ± 0.14
21.77	bf	133	0.73	20.0	6.36	0.82 ± 0.14
4.80	mu	76	0.70	2.0	8.04	0.90 ± 0.21
6.78	mu	95	0.75	26.0	7.96	1.2 ± 0.20
13.38	mu	127	0.74	18.0	7.58	0.99 ± 0.16
21.77	mu	128	0.74	19.0	7.89	1.05 ± 0.17

Table 5.4: Results of the comparison between, 12 hour averaged, HF radar and ADCP-derived current measurements. The column labels indicate the following: f, the radar frequency used for computing currents, N, the number of data points, r, the correlation coefficient between the radar-derived radial current measurement and the correlated component of the ADCP current measurement, $\theta_r - \theta_c$, the difference between the direction of the radial current sensed by the radar and the angle of the maximally correlated ADCP component, δ, the RMS error estimate derived from the difference between the radar-derived currents and the linear fit and Slope, the slope of the linear fit.

Chapter 6

HF Radar Observation of Surface Currents: Relationship to Wind and Wave-Driven Currents

6.1 Introduction

One of the key advantages of HF radar over other current measurement methods is the proximity of the measurement to the surface. Although some near-surface current measurements have been made in laboratory wind-wave tanks by Wu (Wu, 1983), Shemdin (Shemdin, 1972) and Cheung and Street (Cheung & Street, 1988), measurements of near-surface current velocities in the open ocean are very difficult to make and are correspondingly rare. The problem is complicated by the role of waves on the ocean surface and the fact that the orbital

velocities of the water particles themselves are, in general, much larger than the net drift (Kraus & Businger, 1994). Due to the proximity to the surface and the large inherent spatial averaging, radar measurements, and in particular multi-frequency HF radar measurements, are ideally suited to examine this problem.

The ability to probe this near-surface region, the top few meters of the water column, is leading to new information about the air sea interface, in particular, the momentum transfer between winds, waves and the surface current (Fernandez et al., 1996). Multi-frequency radars, such as the MCR system, have the additional advantage of being able to sense the surface current over different depths, depending on the frequency used, and thereby provide information relating to the near-surface current shear. The effective depth of the radar measurement at a given frequency depends on the vertical profile of the horizontal current and is therefore not known precisely. However, estimates of the radar depths can be made by assuming a theoretical form for the current profile. Two possible forms for the current profile due to wind forcing, linear and logarithmic profiles, have been discussed in Section 2.6. The theoretical formulation for the effect of wave-induced transport, or Stokes drift, on HF radar current measurement and the resulting contribution to the vertical profile of the horizontal current have been discussed in Section 2.3. Experimental evidence for the form of the current profile, the dependence of the radar current measurements on wind forcing and the effect of Stokes drift are investigated here.

The effect of Stokes drift on HF radar current measurement is the subject of some interest in the interpretation of the radar measurements. Stokes drift is inherently a Lagrangian process and there has been some question as to whether its effect can be seen by ADCP or HF

radar measurement methods. Whether or not Stokes drift affects radar measurements at all, or whether its effect is significant relative to the uncertainty in radar measurements, is a question of particular interest to ocean circulation modelers. Because HF radar current measurements provide synoptic measurements over relatively large areas of the coastal region, they have potential utility for constraining model predictions. If the effect due to Stokes drift is a significant component of the HF measurements, those who would use the data to improve model predictions would like to either include Stokes drift in their models, or remove the effect from the measurements.

Following the position of Teague (Teague, 1986) we have treated the effect of Stokes drift, in Section 2.3, as a shift of the still water phase speed of the Bragg waves, and suggest, in agreement with Barrick and Weber (Barrick & Weber, 1977) that there should be an effect on HF radar ocean current measurements. Experimental confirmation of the presence of Stokes drift, however, is a complicated problem. For the experiments discussed here, the predicted Stokes current magnitudes are near the expected resolution limits of the radar measurements and are significantly correlated with the local wind. It is therefore expected to be difficult both to detect the Stokes shift and to isolate it from the presence of wind- driven currents. Although the wind-driven currents complicate the problem of isolating the Stokes drift effect, the relationship between the wind forcing and the MCR current measurements are of interest in and of themselves for air-sea interaction investigations. We compare MCR current measurements at different radar operating frequencies with wind speed measurements and friction velocity estimates. We use the assumptions about the form of the current profile and depth of the radar

measurement discussed in Section 2.4 to estimate the near-surface shear and the surface drift from the radar measurements and relate these quantities to the wind and wave forcing from idealized vertical current profiles. We also use the data to contrast the performance of the MUSIC and beam forming data processing algorithms and compare the results to the predictions of the simulation experiments in Chapter 4.

6.2 Comparison Between Radial Surface Current Measurements and Wind Measurements in the Vicinity of the NPS Flux Buoy Deployed in Monterey Bay

Wind measurements, collected from 3-September to 11-November, 1999, from a Flux Buoy, described in Section 3.3.2, included measurements of the bulk wind properties (wind speed and direction) from a propeller-vane anemometer and estimates of the friction velocity computed directly from wind speed measurements from a three dimensional sonic anemometer. Plots of the wind speed, the wind speed squared and the friction velocity estimates are shown in Figure 6.1. It can be seen from the plots that there was a periodic signal in the wind and the wind speed squared. To a lesser extent it is also visible in the friction velocity. This signal is commonly observed in the Monterey Bay region, has a period close to 24 hours and is related to the diurnal temperature variation of California's Salinas valley. A corresponding periodic variation in the MCR radial current measurements is seen in Figure 5.4. The wind speed over the period was generally between 3 and 10 m/s, with a few larger short-term events. The 12 hour

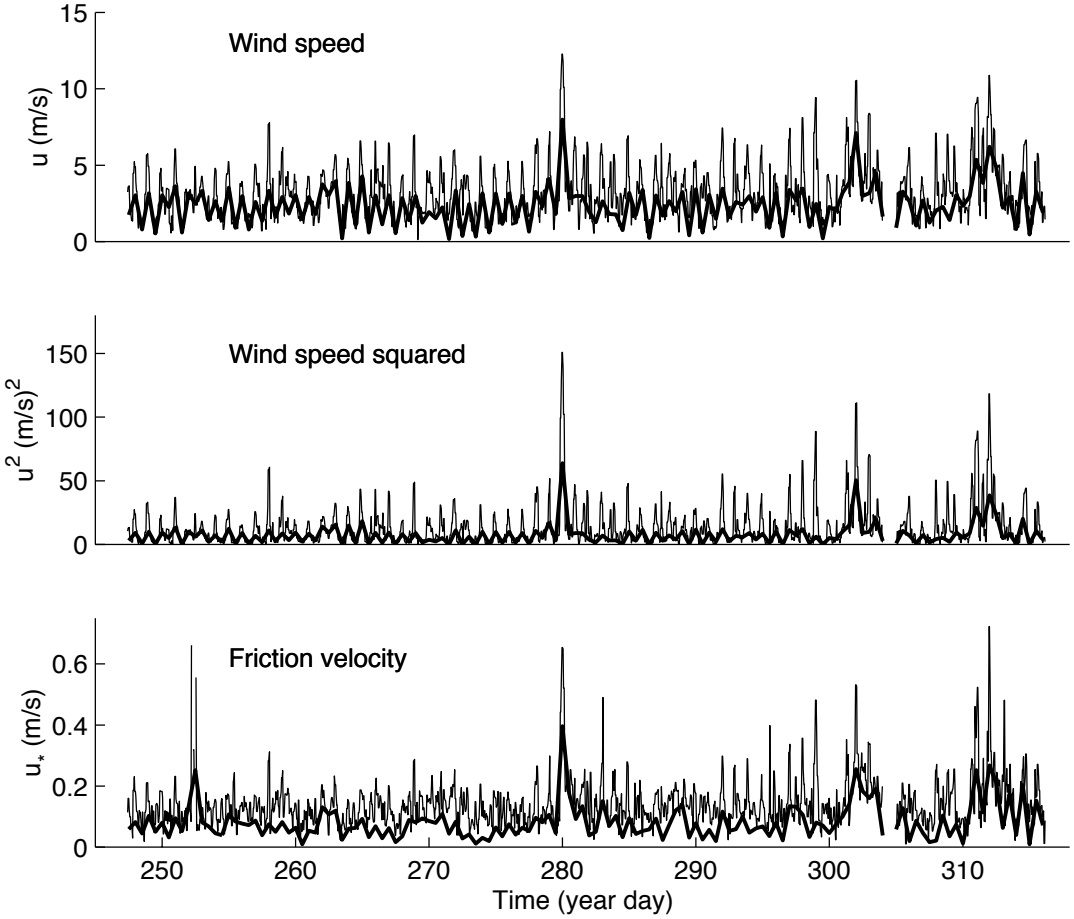

Figure 6.1: Plots of hourly and 12 hour averaged wind measurements from the NPS flux buoy. Friction velocity estimates were made directly from turbulence measurements from a three dimensional sonic anemometer.

averaged winds, also shown on the plot, clearly have lower variance, as do the 12 hour averaged friction velocity measurements, but the disadvantage of this reduction in a signal of interest is more than offset by the reduction in apparently random variations in the MCR current measurements. A few anomalously large events appear in the friction velocity measurements and one anomalously large event appears in the wind speed measurements. While these points may not have been in error, it was decided that they had too much influence on the slope determination of the linear regression analysis and were therefore removed from the data set for subsequent analysis. The wind measurements were used to examine the effect of wind forcing on the surface currents. The radar data were collected from the MCR system at the northern deployment site at Long Marine Lab (LML), see Figure 1.1. To prevent unequal weighting of the radar data due to varying coverage over the 12 hour averaging periods, a check was performed to insure that data were available at least two-thirds of the time from each interval. The measurements referred to here were selected from a region 10° wide in angle, centered at 134° true north, or 39° counter-clockwise from the antenna array broadside direction and a single range bin (3 km) in radius. The radial component of the currents measured by the MCR for each angle in the 10° window were first resolved into their northward and eastward propagating components. The components were then averaged over space and time to form the 12 hour, 10° averaged current data. In order to evaluate the relationship between the measured radial component of the ocean currents and the vector measurements of the wind quantities, we used the same procedure as in the previous section to determine the angle of the maximally correlated component of the wind vector quantities. After determining the correlation coefficients and correlation angle, we plotted the

radial current measurements as a function of the correlated component of the wind parameters and performed linear regression analysis similar to that of the previous section. Plots of the MCR radial current data as a function of the wind speed are shown in Figure 6.2. Although the analysis in Chapter 5 indicated that, at the higher frequencies, beam forming and MUSIC results were very similar in terms of their correlations with each other and their correlations with the ADCP measurements, for the region under consideration here, the region surrounding the NPS flux buoy, the results are different even for the highest frequency. The correlation coefficient between the maximally correlated component of the wind and the MCR radial current measurement and the value obtained for the slope, was higher for the MUSIC processed results. In fact the slope and correlation coefficient values were higher for the MUSIC processed results on all four frequencies. In all cases, however, (except for the 4.8 MHz beam forming case) the correlation was higher in the comparison between the MCR and the ADCP measurements than the correlations observed here between the MCR measurements and the wind speed. This may be explained by the presence of strong currents that are not due to local wind forcing and do not vary significantly over the depth difference between the depth of the radar measurement depth and the top bin of the ADCP, such as tidal or geostrophic currents. Although, in general, larger currents are seen to be associated with higher wind speeds, it appears that the results are not well correlated enough for predictive purposes. Since we expect that the wind-driven currents should decay in magnitude with depth, we expect that the slope of the linear best fit should decrease with frequency. This is observed between the 21.8 and the 4.8 MHz MUSIC results, but not in the other MUSIC or beam forming results.

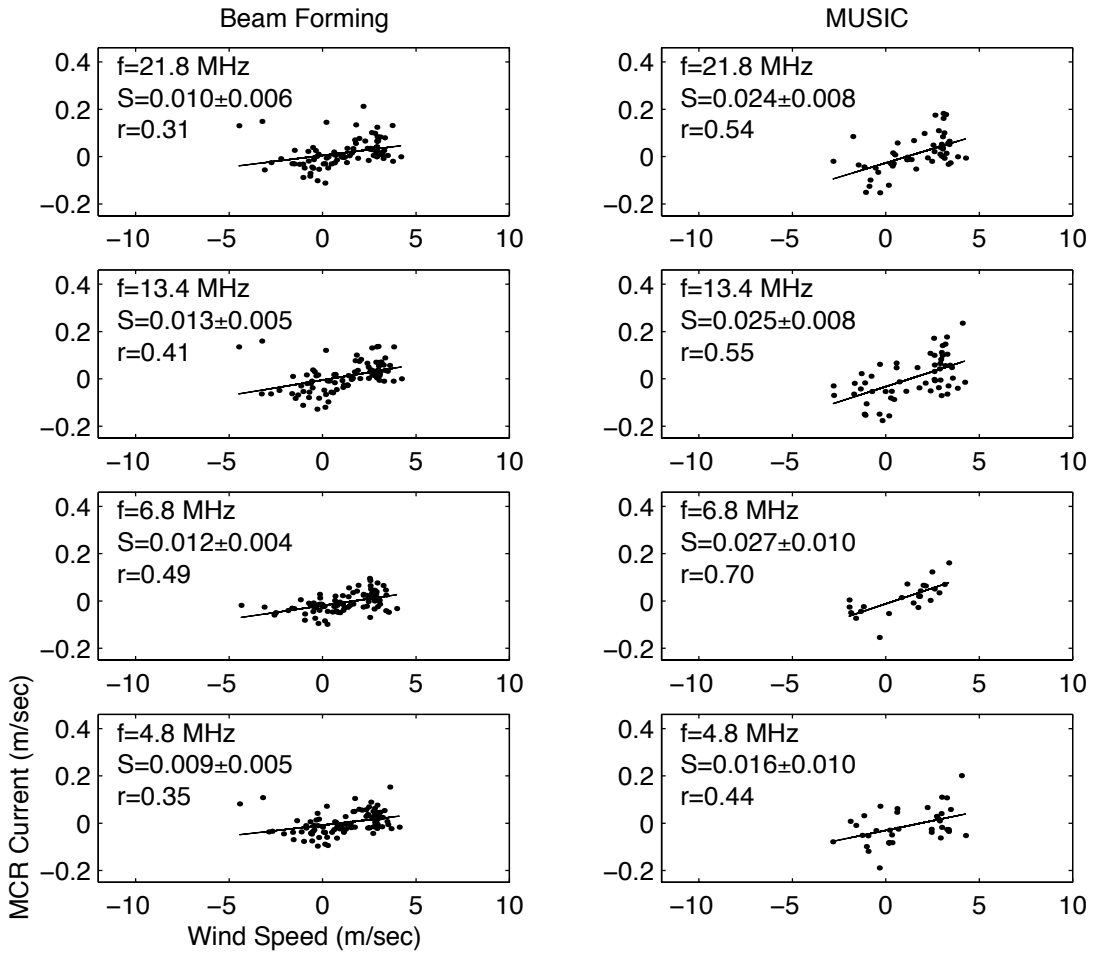

Figure 6.2: Plots of 12 hour averaged radial current measurements from the vicinity of the NPS Flux Buoy, obtained using both beam forming and MUSIC processing, as a function of the maximally correlated component of the wind velocity. The result of a linear best fit (solid line) is shown on the plots. The radar operating frequency, f, the slope of the linear fit, S, and the magnitude of the correlation coefficient, r, are also included for each plot.

The MCR current measurements were also compared with the wind speed squared. Since we expect that the wind stress is proportional to wind speed squared we attempted to determine whether a higher correlation exists between the currents and this quantity. The results are shown in Figure 6.3. The results obtained were inconclusive. In some cases the correlation was increased and in some cases decreased. While results show a dependency of the MCR radial currents on the wind, the results are not adequate to determine the value of the exponent relating the near-surface current to the wind speed.

As described briefly in Section 3.3.2, direct estimates of the friction velocity of the air (the square root of the shear stress per unit mass) were computed from turbulence measurements available from a 3-dimensional sonic anemometer located on the NPS flux buoy (Frederickson et al., 2000). Plots of the MCR radial current measurements as a function of the wind friction velocity estimates are shown in Figure 6.4. In the case of the beam forming results, the correlations at the four MCR frequencies were about the same as those observed in the comparisons with wind speed and wind speed squared. In the case of the MUSIC results, however, the observed correlations were slightly higher than they were in the comparison with wind speed and wind speed squared, for the 4.8, 13.4 and 21.8 MHz radar frequencies. For all three wind parameters, the slope of the linear best fit and the correlation coefficients were generally higher with the MUSIC results. One possible explanation for the higher observed correlations may be the effect of the large radar look angle (about 40° from broadside) required to measure the current in the vicinity of the flux buoy. The MCR receive array is less sensitive at large look angles due to the ideal cosine sensitivity patterns of the loop elements directed with the maxima

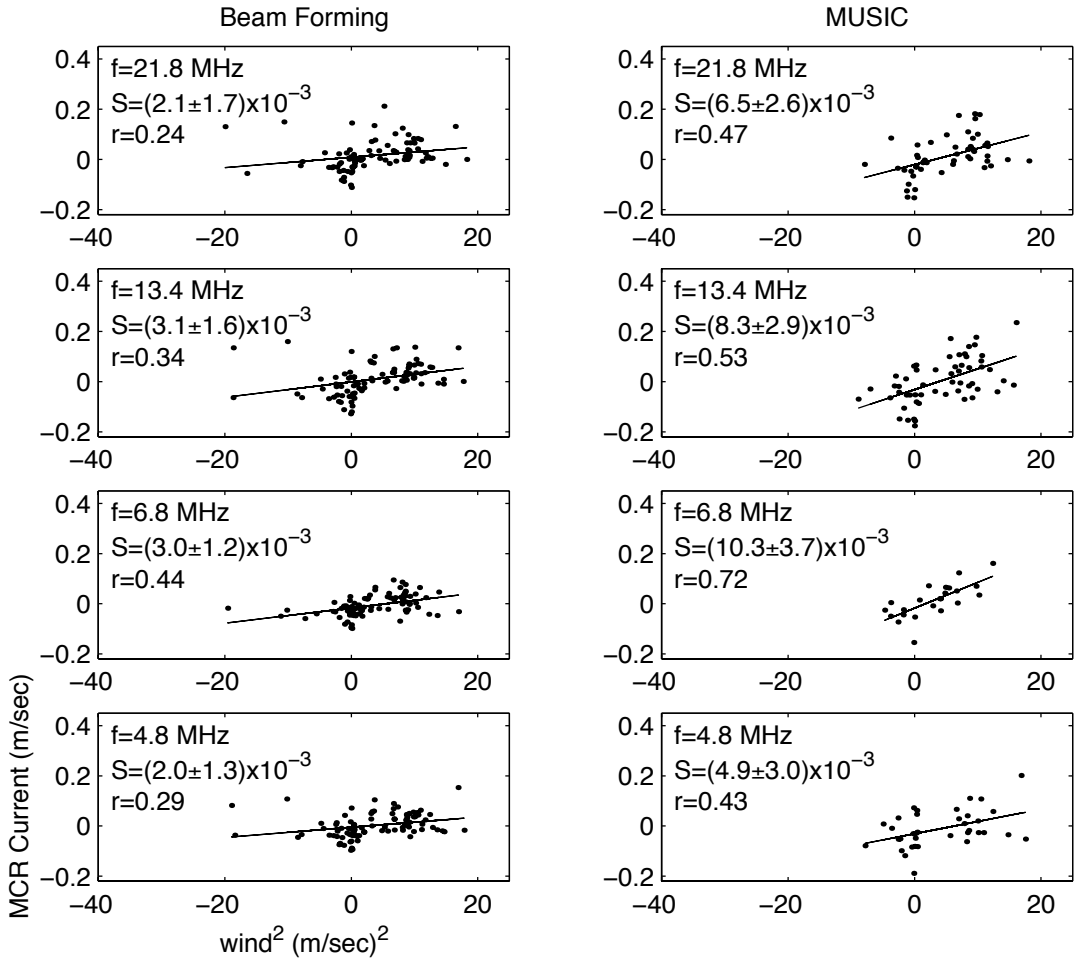

Figure 6.3: Plots of radial current measurements from the vicinity of a Flux Buoy, obtained using both beam forming and MUSIC processing, and the magnitude squared of the maximally correlated component of the wind velocity. The result of a linear best fit (solid line) is shown on the plots. The radar operating frequency, f, the slope of the linear fit, S, and the magnitude of the correlation coefficient, r, are also included for each plot.

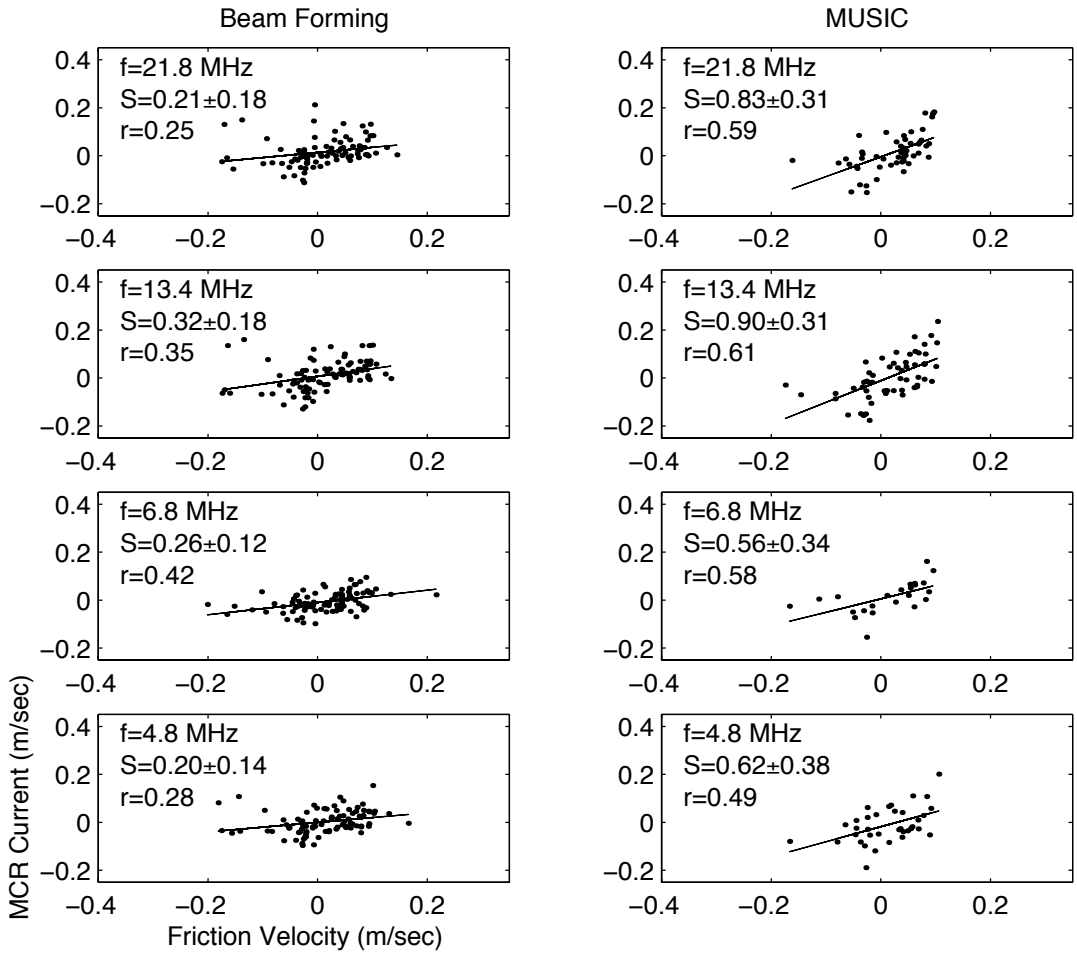

Figure 6.4: Plots of radial current measurements from the vicinity of a Flux Buoy, obtained using both beam forming and MUSIC processing, and the maximally correlated component of the friction velocity. The result of a linear best fit (solid line) is shown on the plots. The radar operating frequency, f, the slope of the linear fit, S, and the magnitude of the complex correlation, r, are also included for each plot.

parallel to broadside. As shown by the simulation results in Section 4.6.1, errors in current measurements obtained using MUSIC processing are less dependent on SNR than errors with beam forming. The characteristics of the formed beam may also play a part. As seen in the simulation results in Figure 4.1, the beam width for the higher frequencies, and the side-lobes for all frequencies, grow with large steering angles. Possibly because of the beam patterns, the simulation experiments in Section 4.6.2 predict a sharp increase in error for beam forming results at 21.8 MHz, and beam steering angles greater than about 25°, with no similar effect seen in the MUSIC results.

The significance of the correlation coefficients was evaluated in each case by examining the auto-correlation of both the wind and MCR measurements to determine the number of statistically independent points in the 12 hour averaged data set. The time lag for the auto-correlation coefficient to decay to $1/e$ was measured for each of the wind parameters, for each radar frequency and processing method and for the shift in the phase speed of the Bragg resonant waves due to Stokes drift (discussed in Section 6.3). Plots of the auto-correlation functions are shown in Figure 6.5. For the wind measurements and the radar-derived ocean current measurements, consecutive points in the 12 hour averaged data were sufficiently uncorrelated to be considered independent. For the Stokes shift, however, correlations were seen to persist for about 60 hours, or about five 12 hour averaged measurements. We therefore assume that, for the Stokes shift estimates, the number of independent points in the 12 hour averaged time series is $N/5$, where N is the total number of points in the series. The number of degrees of freedom (DOF) is then given by $N/5 - 2$. From the number of DOF we compute the 95 % significance

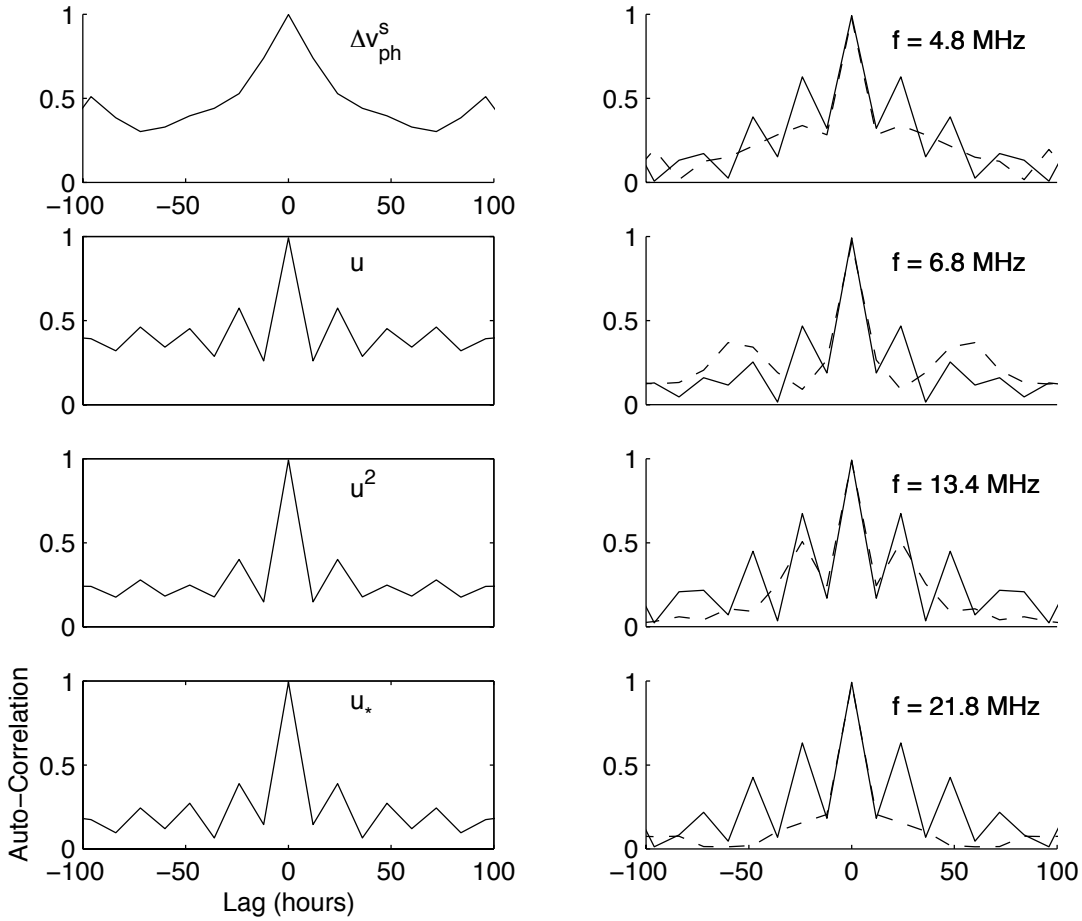

Figure 6.5: Plots of the time-lagged auto-correlation function for the 12 hour averaged Stokes shift, Δv^s_{ph}, wind speed, u, wind speed squared, u^2, and the wind friction velocity, u_*, (left column) and for the MCR current measurements at the four radar operating frequencies (right column). The auto-correlation for both the beam forming processed currents (solid line) and the MUSIC processed currents (dashed line) are shown.

levels for the correlation coefficients (Emery & Thomson, 1997). The values of N, DOF and the 95 % significance levels are given in Table 6.1.

The angle between the radial current and the maximally correlated component of a given wind parameter is also included in the table. Negative values correspond to the correlated component of the wind being rotated counter clockwise relative to the radial direction. In other words, the negative values for the correlation angle observed here correspond to the radial surface current being rotated to clockwise relative to the correlated component of the wind stress. Correlation angles between HF surface current measurements and winds have previously been observed by Paduan and Rosenfeld (Paduan & Rosenfeld, 1996) who used two site HF radar radial current data, from CODAR SeaSonde radar systems, to construct full vector surface current measurements. They found a phase angle of 45.3 degrees for the complex correlation between the surface current and the wind stress, with the surface current to the right of the wind stress. Although only radial data has been used here and the meaning of a direct comparison with the results of Paduan and Rosenfeld is uncertain, it appears that the results here are at least in qualitative agreement with theirs and with the 45 degree clockwise rotation between the equilibrium surface current and the wind stress predicted from Ekman theory.

6.3 Comparison Between Radial Surface Current Measurements and Estimates of the Predicted Effect Due to Stokes Drift

The high resolution directional wave spectral energy data available from the Flux Buoy, described in Section 3.3.2, provided the basis for our examination of Stokes drift in rela-

f (MHz)	Processing method	N	r	95 % Sig.	ϕ (deg)	Slope
Radial Current VS Wind Speed						
21.8	bf	85	0.31	0.22	-25.0	0.010 ± 0.006
13.4	bf	88	0.41	0.22	-28.0	0.013 ± 0.005
6.8	bf	88	0.49	0.22	-15.0	0.012 ± 0.004
4.8	bf	88	0.35	0.22	-21.0	0.009 ± 0.005
21.8	mu	50	0.54	0.27	-34.0	0.024 ± 0.008
13.4	mu	56	0.55	0.27	-46.0	0.025 ± 0.008
6.8	mu	23	0.70	0.40	-85.0	0.027 ± 0.010
4.8	mu	36	0.44	0.33	-40.0	0.016 ± 0.010
Radial Current VS Wind Speed Squared						
21.8	bf	85	0.24	0.22	-37.0	$(2.1 \pm 1.7) \times 10^{-3}$
13.4	bf	88	0.34	0.22	-51.0	$(3.1 \pm 1.6) \times 10^{-3}$
6.8	bf	88	0.44	0.22	-15.0	$(3.0 \pm 1.2) \times 10^{-3}$
4.8	bf	88	0.29	0.22	-49.0	$(2.0 \pm 1.3) \times 10^{-3}$
21.8	mu	50	0.47	0.27	-29.0	$(6.5 \pm 2.6) \times 10^{-3}$
13.4	mu	56	0.53	0.27	-68.0	$(8.3 \pm 2.9) \times 10^{-3}$
6.8	mu	23	0.72	0.40	-93.0	$(10 \pm 3.7) \times 10^{-3}$
4.8	mu	36	0.43	0.33	-53.0	$(4.9 \pm 3.0) \times 10^{-3}$
Radial Current VS Friction Velocity						
21.8	bf	85	0.25	0.22	-78.0	0.21 ± 0.18
13.4	bf	88	0.35	0.22	-81.0	0.32 ± 0.18
6.8	bf	88	0.42	0.22	-54.0	0.26 ± 0.12
4.8	bf	88	0.28	0.22	-72.0	0.20 ± 0.14
21.8	mu	50	0.59	0.27	-51.0	0.83 ± 0.31
13.4	mu	56	0.61	0.27	-66.0	0.90 ± 0.31
6.8	mu	23	0.58	0.40	-92.0	0.56 ± 0.34
4.8	mu	36	0.49	0.33	-55.0	0.62 ± 0.38

Table 6.1: Results of linear regression and correlation analysis of radar-derived radial ocean surface currents and wind speed, wind speed squared and friction velocity as a function of radial current processing method and radar operating frequency. Radar data were collected from the LML site MCR system and correspond to the vicinity of the NPS flux buoy. Under processing method, (bf) indicates beam forming and (mu) indicates MUSIC processing was used to obtain the radial current measurements. Wind measurements and friction velocity estimates were obtained from sensors located at the Flux Buoy.

tion to its effect on HF radar surface current measurements. An example of a directional wave energy spectrum obtained from the NPS flux buoy measurements is shown in Figure 6.6. The spectral wave data are used to make estimates of the Stokes drift current at a given depth, and to estimate the shift of the phase speed of the Bragg resonant waves due to the effect of Stokes drift (Stokes shift) corresponding the radar system's operating frequencies. The formalism for computing the Stokes shift and Stokes drift currents is outlined in Section 2.3. To compute the Stokes shift from the directional wave spectral energy data, we begin with the expression given by Equation 2.21, and make the substitutions, $\omega = 2\pi f$ and $E(\nu, \theta) = (2\pi/\rho g)F(\omega, \theta)$. We then approximate the double integral by the sum over direction and frequency and obtain

$$c_s(k_r, \theta_r) = \frac{32 k_r \pi^3}{g} \sum_i \cos(\theta_r - \theta_i) \Delta\theta \sum_j \frac{E(\nu_j, \theta_i)\nu_j^3}{2k_r + \omega^2/g} \Delta\nu, \tag{6.1}$$

where k_r is the radar operating wavenumber, and θ_r is the radar look angle (parallel to the propagation direction of the Bragg resonant waves) referenced to true north. Instead of computing the above, which is effectively the component of the Stokes shift parallel to the radar look direction, it is equivalent and more efficient in terms of analyzing the data, to compute the vector Stokes shift,

$$\mathbf{c}_s(k_r) = \frac{32 k_r \pi^3}{g} \sum_i [\sin\theta_i \hat{\mathbf{x}} + \cos\theta_i \hat{\mathbf{y}}] \Delta\theta \sum_j \frac{E(\nu_j, \theta_i)\nu_j^3}{2k_r + \omega^2/g} \Delta\nu \tag{6.2}$$

and then take the component parallel to the desired radar look direction. We computed the time series of the vector Stokes shift by inserting the spectral energy data from the Flux Buoy $E(\nu, \theta)$ into 6.2 for all available hourly spectral data. A time series of the Stokes shift corresponding to the highest radar frequency of operation, 21.8 MHz, is shown in Figure 6.7. The computation of the Stokes current as a function of depth, as opposed to a function of frequency, from the

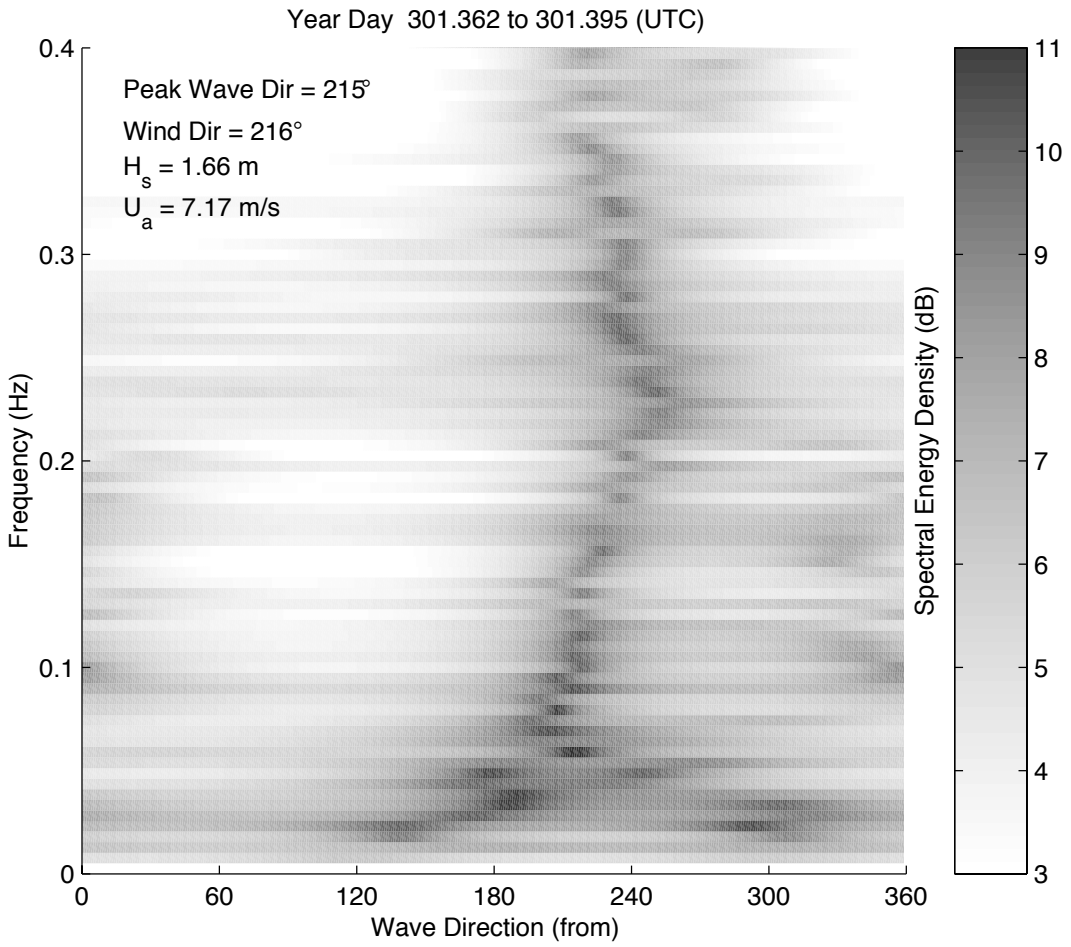

Figure 6.6: Example of directional wave spectral energy data from a flux buoy located inside Monterey Bay. This particular sample was taken during relatively high winds for the period. The direction (from) of the maximal spectral energy, the wind direction, the significant wave height, H_s, and the wind speed at 3.96 m, u_a, corresponding to the time of the spectral measurement, are shown on the figure.

directional wave spectral energy data, involves similar treatment beginning with equation 2.17. As seen in the figure, the magnitude of the expected shift in wave speed was generally less than 4 cm/s for the radar operating frequency of 21.8 MHz. Stokes shift predicted for the lower frequencies was even smaller. The variance of the Stokes shift was only 0.09 to 0.38 percent of the variance in the radial current measurements for the lowest to highest radar operating frequencies, respectively. Since the larger magnitude events seen in the figure (4 to 7 cm/s) were of short duration, averaging to reduce random variations in the MCR measurements had the effect of reducing the variations in the signal being investigated. The RMS magnitude of 12 hour averaged Stokes shift corresponding to the 21.8 MHz radar frequency was only about 1.4 cm/sec, or similar to the RMS error estimates of 1.55 and 1.87 cm/s for beam forming and MUSIC processed results, respectively, obtained from the inter-channel comparisons in Section 5.2.1. We expect that this signal of the Stokes shift will be difficult to detect given the expected errors in current measurement. For the lower frequencies the difficulty is compounded. The Stokes drift signal is expected to decay with depth while the error in the radar measurements increases with the radar wavelength. In terms of concerns about the effect of Stokes drift on the radar measurements and the application of these measurements to constraining ocean circulation models, however, these conclusions are encouraging. If our estimation of the effect of Stokes currents found in Monterey Bay on HF radar measurements is fairly typical for HF radar deployments and our error estimates for the MCR are typical for HF radar systems in general, then the expected contribution of Stokes drift on the radar-derived ocean currents is roughly equal to, or smaller than, the expected uncertainty in the radar derived ocean current measurements themselves, and the

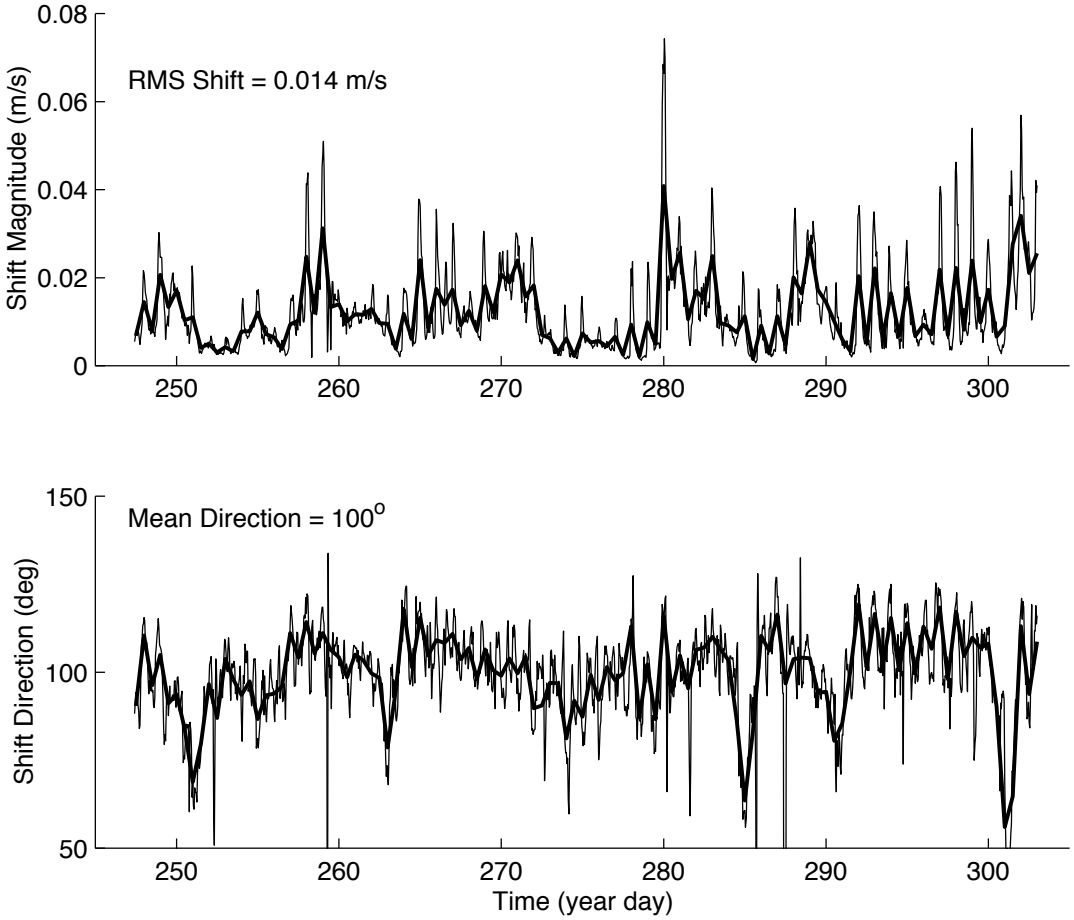

Figure 6.7: Time series of the magnitude and direction of the expected shift in phase speed for Bragg resonant wave-trains corresponding to 21.8 MHz radar frequency, due to Stokes drift. The shift was calculated from directional wave spectral energy measurements from the NPS flux buoy inside Monterey Bay. The thick line on the plots shows the 12 hr averaged data.

effect of Stokes drift can be neglected.

To gain insight into the range of wave frequencies that make up the most significant contribution to the Stokes shift, we examined the predicted Stokes shift as a function of the upper limit on the sum over wave frequency in Equation 6.2. A plot showing the results, along with a plot of the peak spectral wave energy as a function of frequency, for the sample wave energy spectrum (Figure 6.6) are shown in Figure 6.8. It is interesting to note that although the sample spectral data has much higher energy at the lower wave frequencies (less than 0.15 Hz) the Stokes shift is dominated by the higher wave frequencies (0.2 to 0.5 Hz). This demonstrates that even when there is a strong swell component, the Stokes drift is dominated by the wind-wave contribution.

Plots of the radial current and the component of the predicted Stokes shift parallel to the correlation angle are shown in Figure 6.9. Measurements were spatially averaged over a region ten degrees wide centered on the bearing from the MCR deployment site at LML to the location of the NPS flux buoy, 134° true north, at a range of about 21 km from the radar. The temporal averaging is consistent with the averaging period used in the previous section and was found to improve the observed correlations over unaveraged results. In contrast to most of the results obtained in the previous sections, the correlations observed between the Stokes shift estimates and the MCR radial current measurements were slightly higher for beam forming processed results, even on the lowest frequency. However, due to the lower number of independent data points in the Stokes shift data, as discussed in Section 6.2, the significance of all of the correlation coefficients was also reduced, and the differences in the observed correlation

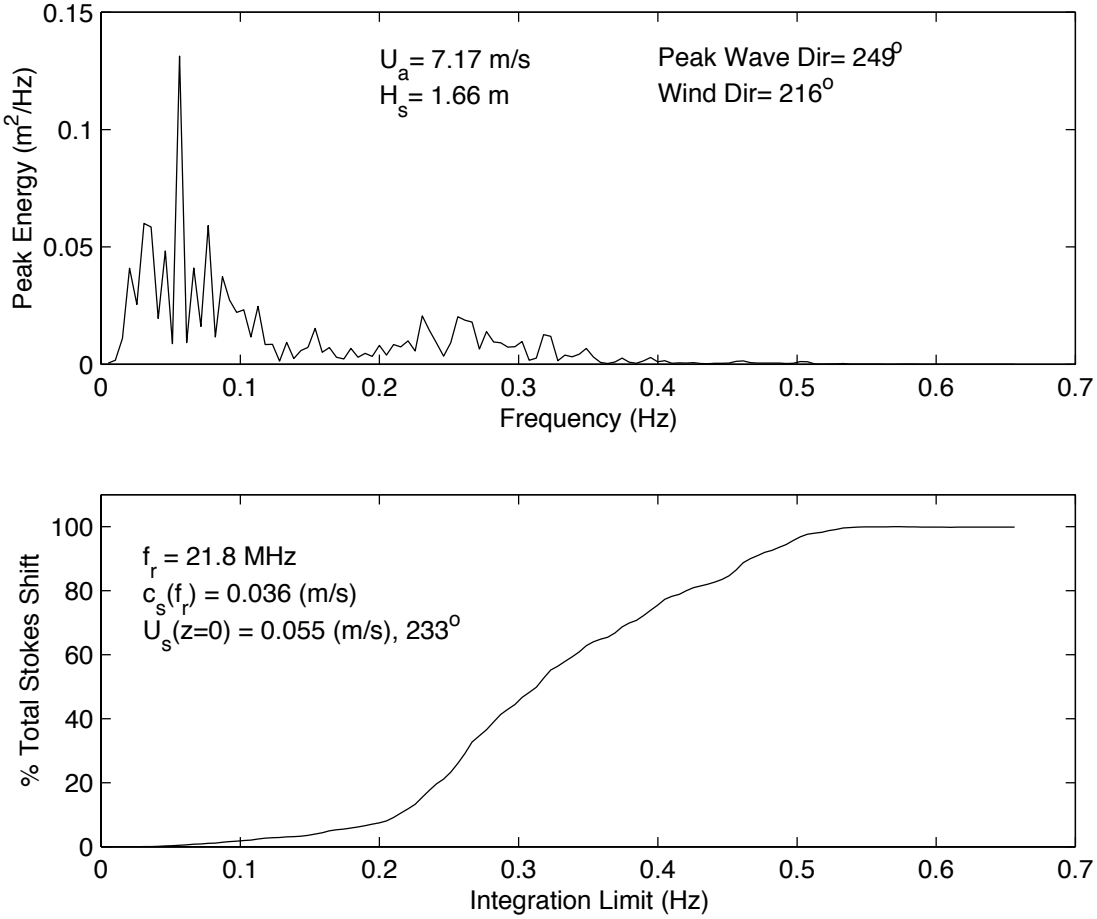

Figure 6.8: Peak spectral wave energy density as a function of wave frequency (upper plot) and the fraction of the total shift due to Stokes drift expected for a Bragg wave resonant with a radar frequency of 21.8 MHz as a function of the upper limit on the wave frequencies included in the sum used to calculate the Stokes shift. The wind speed, u_a, the significant wave height, H_s, the peak wave direction and the wind direction are included on the upper plot. The total expected shift due to Stokes drift, c_s, and the surface drift due to Stokes drift, $U_s(z=0)$ are included on lower plot.

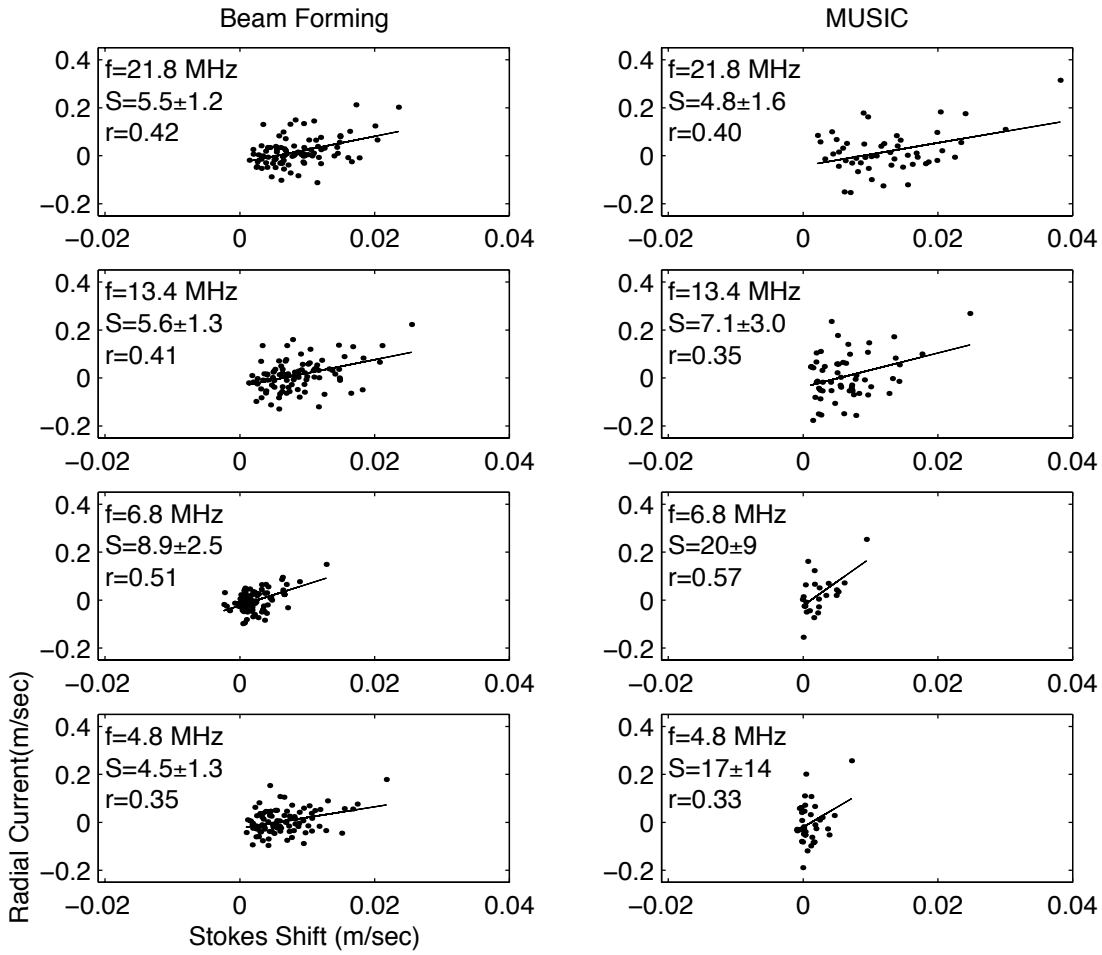

Figure 6.9: Plots of radial current measurements from the vicinity of the NPS Flux Buoy, obtained using both beam forming and MUSIC processing, as a function of the component of the Stokes shift parallel to the correlation angle. The result of a linear best fit (solid line) is shown on the plots. The radar operating frequency, f, the slope of the linear fit, S, and the correlation coefficient, r, are also included for each plot.

coefficients may not be significant. The 95 % significance levels for the correlation coefficients were determined based on the estimated number of degrees of freedom. The values of N, the number of degrees of freedom and the 95 % significance levels, are given in Table 6.2. From analysis of the significance of the correlation coefficient, we see that only the correlation coefficient for the 6.8 MHz beam forming processed result is significantly different from zero at the 95 % confidence level. The correlations observed given the number of independent data points available may simply be too low to draw much in the way of conclusions. Although the scatter seen in the plots is very large, trends do appear in the slope values. With the exception of the lowest frequency in the MUSIC processed results, there appears to be an increase in the slope with radar wavelength used and therefore with the expected depth of the radar-derived current measurements. Also, at the two higher frequencies, the results obtained using beam forming and MUSIC processing agree fairly well and give a value of about 5. In other words, the near-surface measured currents that correlate with the predicted effect of Stokes drift are about 5 times larger in magnitude than the predicted effect of Stokes drift on the radar measurements. As the depth increases, the ratio also increases. Therefore, if the currents observed are due to Stokes drift, then their magnitudes near the surface are greater than those predicted by the Stokes drift formulation and they do not decay with depth as rapidly as Stokes drift currents are predicted to. The slope values are given in Table 6.2 and are plotted as a function of radar wavelength in Figure 6.10. The differences between the directions of the maximally correlated Stokes Shift and the radar look angle, listed in Table 6.2, are erratic. This is not surprising given the low confidence levels associated with the correlation coefficients.

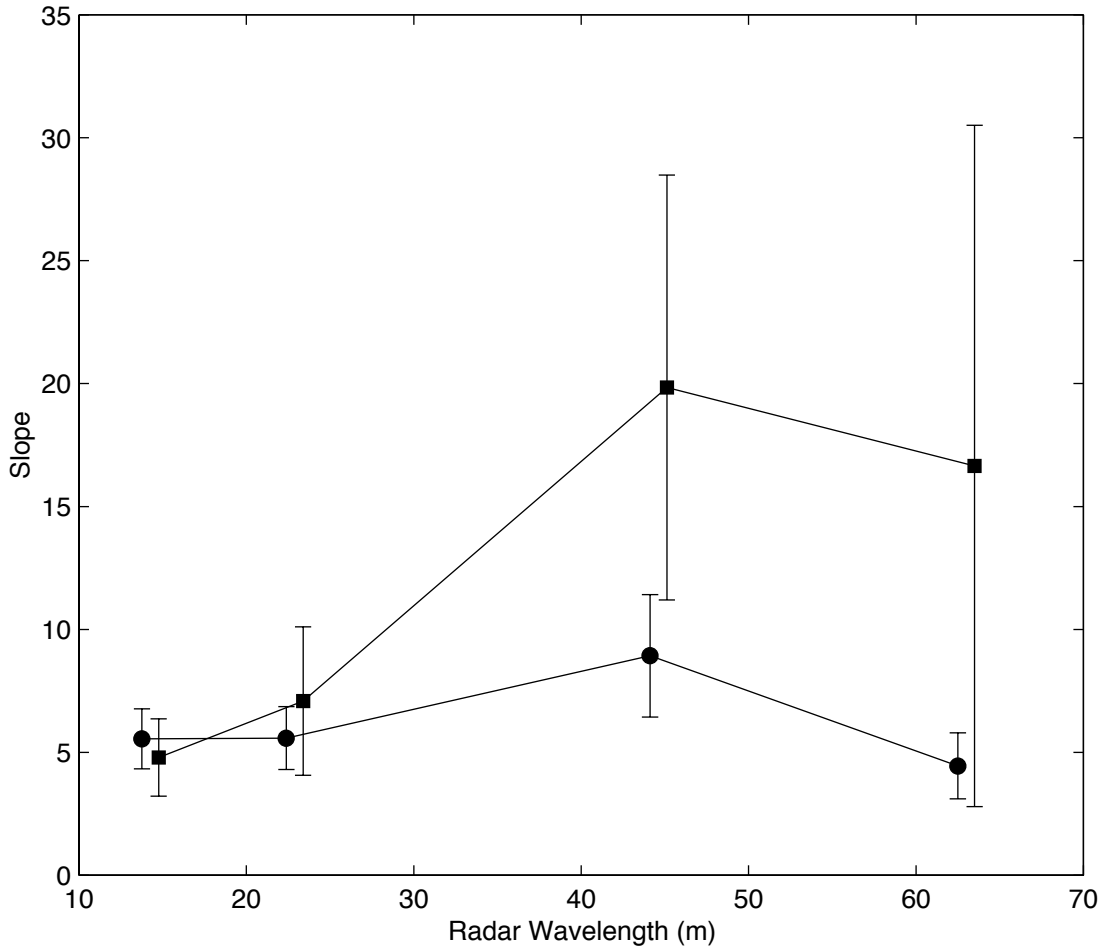

Figure 6.10: Slope values as a function of radar wavelength. The slope values indicate the ratio of the apparent Stokes drift effect in currents measured by the MCR to the predicted effect estimated from wave spectral energy data. The results obtained using MUSIC (square) processing have been shifted slightly to the right of the results from beam forming (circle) so that the point markers and error bars may be distinguished. Values for the plot are listed in Table 6.2.

f (MHz)	Processing method	DOF	N	r	95 % Sig.	ϕ (deg)	S
21.8	bf	88	0.42	0.48	-73.0	5.6 ± 1.2	
13.4	bf	91	0.41	0.47	-62.0	5.6 ± 1.3	
6.8	bf	91	0.51	0.47	43.0	8.9 ± 2.5	
4.8	bf	91	0.35	0.47	-37.0	4.4 ± 1.3	
21.8	mu	51	0.40	0.63	-39.0	4.8 ± 1.6	
13.4	mu	57	0.35	0.60	27.0	7.1 ± 3.0	
6.8	mu	24	0.57	0.88	51.0	20 ± 8.6	
4.8	mu	37	0.33	0.75	53.0	17 ± 14	

Table 6.2: Results of the comparison between 12 hour averaged HF radar current measurements and the predicted shift due to Stokes drift. Stokes shift predictions were based on calculations from directional wave spectral data obtained from the NPS flux buoy. The column labels indicate the following: f, the radar frequency used for computing currents, N, the number of data points, r, the correlation coefficient between the radar derived radial current measurement and the correlated component of the ADCP current measurement, $\theta_r - \theta_c$, the difference between the direction of the radial current sensed by the radar and the angle of the maximally correlated ADCP component, δ, the rms error estimate derived from the difference between the radar-derived currents and the linear fit.

6.4 Comparison Between Estimates of Stokes Drift and Measurements of the Wind Speed

As demonstrated by the results in Figure 6.8, the Stokes drift currents are strongly influenced by the higher-frequency, wind-driven ocean waves. These waves are expected to be correlated with the local winds as are the wind-induced drift currents. Correlations observed between HF radar ocean current measurements and Stokes shift predictions may therefore be due to the presence of wind-induced near-surface currents and the correlation between the wind forcing and the Stokes drift. The plot of the predicted Stokes shift corresponding to the 21.8 MHz radar operating frequency and the wind speed (shown Figure 6.11) confirms this expectation. The correlation between the predicted Stokes shift corresponding to the 21.8 MHz radar fre-

quency and the wind speed (r = 0.70) is found to be larger than the highest correlation observed between the MCR radial current measurements and the Stokes shift. Shown in Figure 6.11 is a plot of the predicted Stokes current at the surface ($z = 0$) and the wind speed. The slope of the linear fit to the estimated Stokes current at the surface as a function of the wind speed gives an estimate of the surface drift due to Stokes drift of 0.50 ± 0.08 % of the wind speed. This result is about a factor of 3 smaller than the smallest value predicted by Kenyon (Kenyon, 1969) for the case of an ideal uni-directional wind-wave spectrum. Kenyon predicted a surface drift due to Stokes drift of 1.57 to 3.58 % of the wind speed depending on the assumed form of the wind-wave spectrum. The smallest value corresponds to the form of the wind-wave spectrum that best fit the wave data of Pierson and Moskowitz (Pierson & Moskowitz, 1964).

The discrepancy in these results may be an indication that the wave energy spectra measured at the NPS flux buoy are not well approximated by the form of ideal wind-wave spectra assumed by Kenyon.

6.5 Radial Surface Current Difference Measurements Compared With Estimates of the Predicted Effect Due to Stokes Drift and Wind Forcing

The ability to measure the change in the near-surface horizontal current with depth has great importance to the understanding of the momentum transfer between the atmosphere and the ocean. Some of the theories for functional approximations of a wind and wave-driven

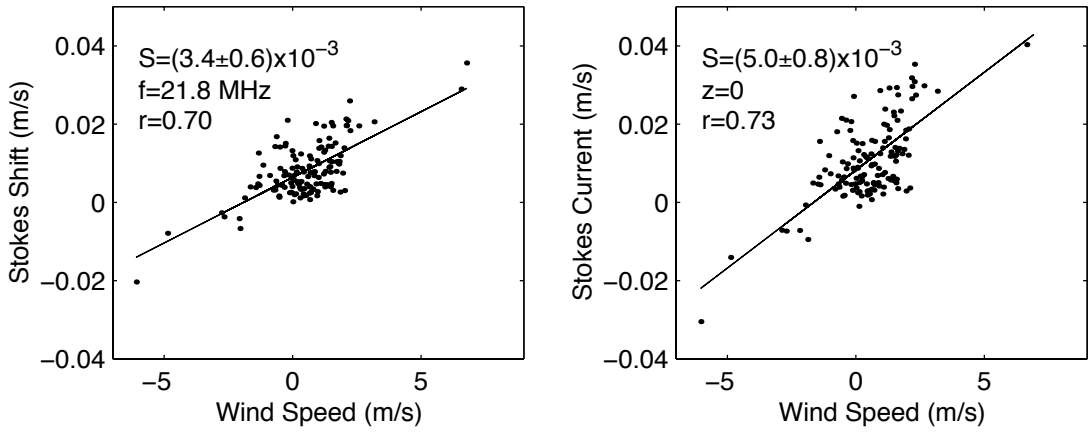

Figure 6.11: Plots of the expected Stokes shift of the Bragg resonant wave corresponding to 21.8 MHz radar frequency (left) and Stokes drift current at $z = 0$ (right) as a function of the wind speed. The Stokes drift calculations were made using the directional wave spectral energy measurements from a flux buoy inside Monterey Bay. The wind speed measurements were collected at the buoy. The magnitude of the complex correlation coefficient, r, and the slope of the linear best fit, S, are given on the plots. The result of a linear best fit (solid line) is shown on the plots. The radar operating frequency, f, the slope of the linear fit, S, and the magnitude of the complex correlation, r, are also included for each plot.

profile are discussed in Section 2.6, but there are dissenting opinions about which profile is more likely to apply to the open ocean. Although efforts have been made to investigate the form of the vertical current profile and its relationship to the wind in wind-wave tanks, the results of the experiments do not necessarily translate to the open ocean and the exact form of the vertical current profile is unknown.

In order to examine the variation in the near surface currents with depth and, at the same time, separate currents that are constant with depth, for example tidal currents, from the wind and wave-induced currents, we take advantage of the fact that the MCR can measure the surface current at different effective depths depending on the selected transmit frequency. As discussed in Section 2.2, the depth over which HF radar systems sense the surface current increases as the radar operating frequency decreases. To obtain the radar-derived current difference measurements we subtracted the current measured using the three lowest radar frequencies from the current measured using the highest frequency. We thus computed measurements for three depth differences.

An important disadvantage of the current difference measurements is that the fractional error in the measurement is increased while the magnitude of the quantity we are trying to examine is decreased. Because of the level of uncertainty in the radar current measurements and the MCR system's limitations on beam width (about 50° at the lowest frequency, 4.8 MHz), current difference measurements obtained using beam forming processing with the MCR system are difficult to interpret. Because results of the simulation experiments and the experiments in this and the previous chapter indicate, particularly for the lower MCR frequencies, that the

MUSIC processed measurements better characterize the ocean currents, in this work only MUSIC processed currents have been used for the current difference measurement analysis.

Current difference measurements were used to examine the correlation between the radar-derived near-surface currents and the Stokes drift predictions. Plots of the magnitude of the predicted Stokes shift for the Bragg waves corresponding to the MCR's four operating frequencies are shown in Figure 6.12. Correlations between the difference in current measured at the 21.8 and 4.8 MHz radar operating frequencies and the difference in the expected Stokes shift for those two frequencies are examined. In the case of the MUSIC processed measurements, spatial averaging over 10° of azimuth and Temporal averaging over 12 hour segments was used to decrease gaps in the data and random variations.

Correlations between the predicted Stokes shift difference and the current difference measurements were examined over a range of the angle defining the center of the spatial averaging region. A relatively high correlation coefficient was found for regions centered on radar look angles that range from about 145° to 155° and a lower correlation coefficient was found for the region centered on a radar look angle of 134° true north, the true bearing from the MCR to the NPS flux buoy. For the results used in this analysis, the MCR current measurements were obtained by averaging spatially over a region centered on 146°. It is not clear why the correlations were higher for the regions centered 10 to 20° to the right of the NPS flux buoy. It is possible that the results are due to a systematic pointing error in the MCR deployment at LML, but experiments in Section 5.2.3 comparing the MCR current measurements with the ADCP current measurements, although involving a different mooring and radar look angle, did

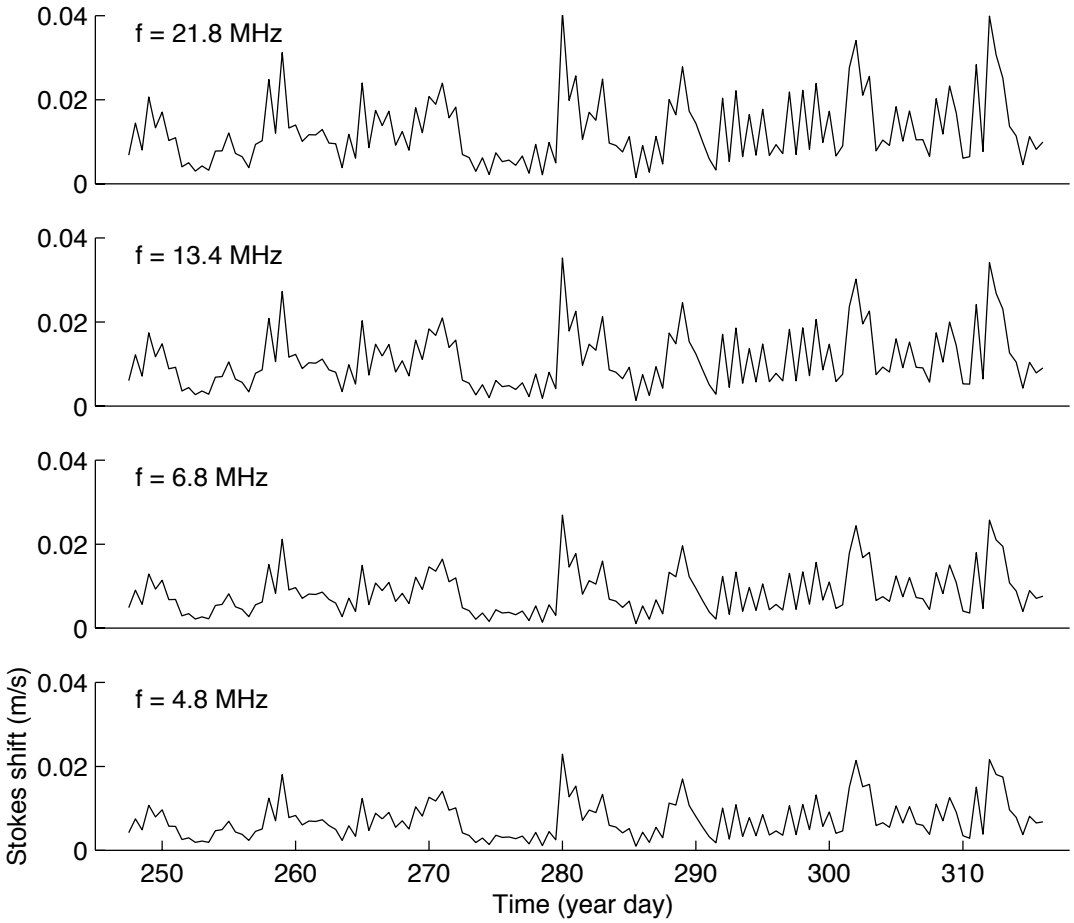

Figure 6.12: Time series of the estimated Stokes shift magnitudes corresponding to the four MCR frequencies of operation. The corresponding radar frequency, f, is given on each plot.

	N	DOF	r	95 % Sig.	ϕ (deg)	Slope
Δv^s_{ph}	45	9	0.56	0.60	-10	8.9 ± 2.5
u	45	45	0.60	0.29	-42	0.017 ± 0.006
u^2	45	45	0.59	0.29	-84	$(5.2 \pm 1.9) \times 10^{-3}$
u_{*a}	45	45	0.65	0.29	-73	0.58 ± 0.20

Table 6.3: Results of comparison between radial current difference measurements and predicted Stokes shift difference (Δv^s_{ph}), wind speed (u), wind speed squared (u^2) and wind friction velocity estimates (u_{*a}). The number of points (N), degrees of freedom (DOF) assumed, correlation coefficient (r) and correlation coefficient at the 95 % significance level, the angle between the direction of the measured radial current component and the correlated component of the quantity being compared and the slope of linear fit, are included in the table.

not give any indication of a similar systematic bias. It is also possible that the variation in the correlation coefficient is related to the difficulty in obtaining current measurements at large angles relative to the broadside direction of the receive array. Measurements at large angles are more difficult to obtain due to the cosine sensitivity patterns of the antenna elements.

The current difference, measured by subtracting the current measured at the lowest radar frequency from the current measured at the highest radar frequency, is plotted as a function of the wind speed, wind speed squared, friction velocity and expected effect of Stokes shift, in Figure 6.13. In spite of the larger errors expected in the difference measurement, the magnitudes of the correlation coefficients between the MCR difference measurements and the wind, wind speed squared, friction velocity and the Stokes shift are all similar in magnitude and are comparable to those found in the comparisons involving single frequency measurements. The results of the analysis including the number of points, degrees of freedom, correlation angles and slope values are summarized in table 6.3. The correlation angles are all seen to be negative, indicating that the radar look angle is greater than the angle of the maximally correlated com-

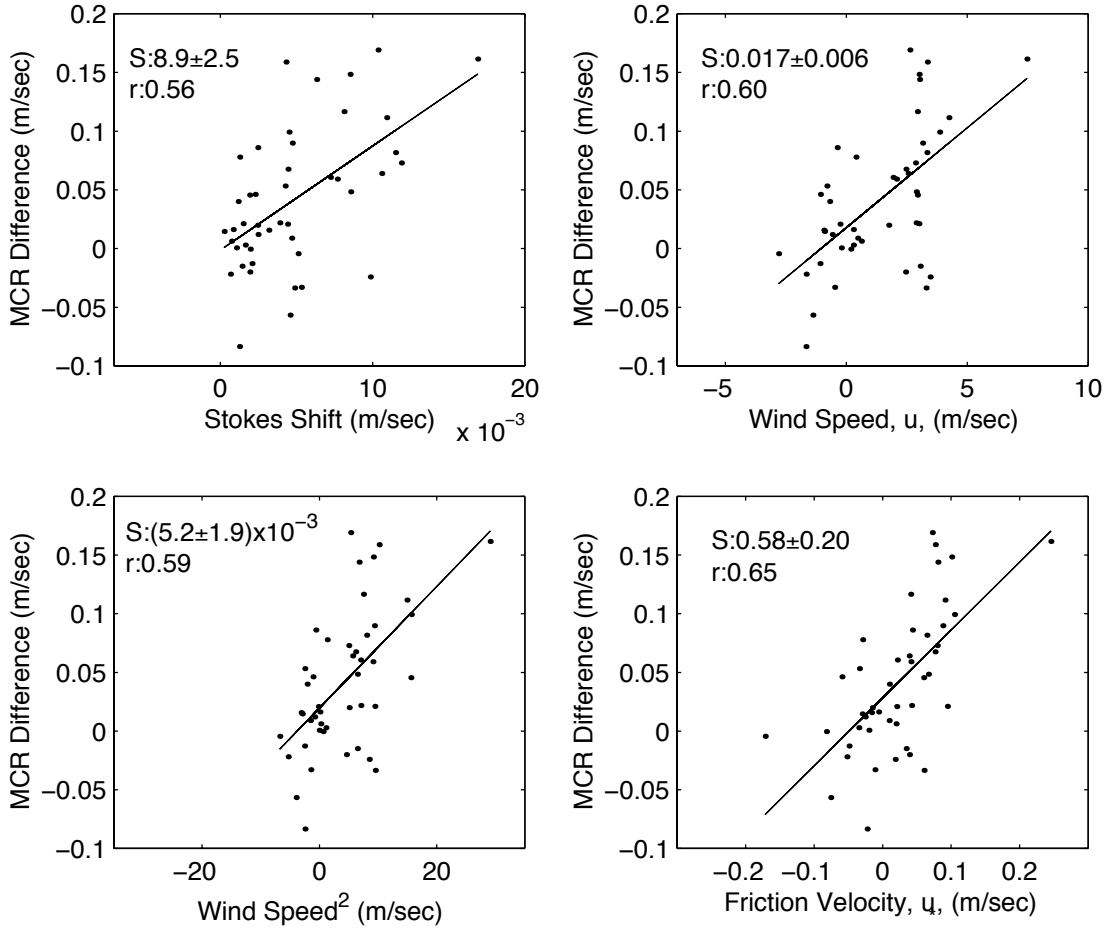

Figure 6.13: Plots of the difference in radial current, measured at 21.8 and 4.8 MHz, and processed using MUSIC, as a function of the maximally correlated component of the expected difference in Stokes shift, the wind speed, the wind speed squared and the friction velocity. The result of a linear best fit (solid line) is shown on the plots. The slope of the linear fit, S, and the magnitude of the complex correlation, r, are also included for each plot.

ponent of the vector quantity being compared or, in other words, they may indicate clockwise rotation between the quantities measured above or at the surface and the currents measured under the surface. Given the lack of knowledge of the uncertainty in the correlation angle it would be a mistake to read too much into these values. It may, however, be significant that the correlation angle for the Stokes shift comparison is less than that of the three wind quantities.

The slope of the linear fit to the MCR radial current difference measurements plotted as a function of the predicted Stokes shift difference gives us an idea of the relative contribution of the Stokes drift to the vertical shear in the near-surface current. If the radial current difference measured by the radar were dominated by Stokes drift, we would expect a value of, at most, one, for the slope. In our analysis, however, the measured slope had a value of 8.9 ± 2.5. This would indicate that the component of the predicted current difference due to Stokes drift that we found to be correlated with the observed difference in radial current measurements between 21.8 and 4.8 MHz accounted for only about one-ninth of the total measured current difference.

Since there exists considerable uncertainty as to the form of the vertical current profile with depth (discussed in Section 2.6), the effective depth of the radar current measurement is also not precisely known. If we assume that the vertical current profile is best described by a logarithmic form, restated here as

$$U(z) = U_s - \frac{u_{*w}}{K} ln\left(\frac{z}{z_o}\right), \tag{6.3}$$

where U_s is the magnitude of the current at the surface, $K = 0.4$ is von Kármán's constant, and z_o is the roughness length, then the difference in the current at two depths, z_1 and z_2, corresponding to the effective measurement depths for two radar operating frequencies, f_1 and

f_2, is

$$U_{z_2} - U_{z_1} = \frac{u_{*w}}{K} ln\left(\frac{f_2}{f_1}\right). \tag{6.4}$$

As seen by the above equation, the current difference is expected to be proportional to the friction velocity in the water. The corresponding plot in Figure 6.13 shows rough agreement with this expectation. If the shear stress, given by

$$\tau = \frac{1}{2}\rho u_*^2 \tag{6.5}$$

is constant across the boundary, then the friction velocity in the air and the friction velocity in the water are related by $\rho_w u_{*w}^2 = \rho_a u_{*a}^2$ or $u_{*w} = \beta\, u_{*a}$, $\beta \approx 0.035$. The experimental results of Wu (Wu, 1983) indicate that $\rho_w u_{*w}^2 < \rho_a u_{*a}^2$ and from his results $\beta = 0.53/22 \approx 0.024$. From Equation 6.4 we expect that the slope of the linear best fit to the MCR difference current measurement as a function of the friction velocity (Figure 6.13) should be given by

$$S = \frac{\beta}{K} \ln\left(\frac{f_2}{f_1}\right), \tag{6.6}$$

where, from our data, $f_2 = 21.8$ and $f_1 = 4.8$ MHz. Using the measured slope value given in Table 6.3, and solving for β, we find $\beta = 0.153 \pm 0.052$, not in agreement with either of the above results. Provided that this result is not due to a systematic bias in the MCR measurements or in the estimation of the friction velocity from the wind measurements, the result could be an indication that the log profile does not accurately describe the near-surface vertical current profile in the open ocean, under the conditions observed here.

If the vertical profile of the near-surface horizontal current is assumed to be well characterized by a linear profile, as described in Section 2.6, then the current as a function of

depth is given by

$$U(z) = U_s - \frac{U_1}{z_o} z, \tag{6.7}$$

where U_1/z_o is a constant representing the current shear. Taking the difference in the current corresponding to two effective radar current measurement depths, z_1 and z_2, gives

$$U_{z_2} - U_{z_1} = -\frac{U_1}{z_o}(z_2 - z_1). \tag{6.8}$$

Under the linear profile assumption, the effective depth of the radar current measurement, as discussed in Section 2.6, is about 0.08 times the wavelength of the Bragg resonant wave. Therefore the difference in the effective depths of the current measurement for two radar frequencies, f_1 and f_2 is

$$d = (z_2 - z_1) = 0.08(\lambda_2 - \lambda_1), \tag{6.9}$$

where λ_1 and λ_2 refer to the wavelengths of the Bragg resonant ocean waves, or half the radar wavelengths. For the frequencies used in this analysis, the highest and lowest MCR operating frequencies, $d = 1.95$ m. If we assume a linear relationship exists between the current shear and the wind speed, we can then write

$$\frac{U_1}{z_o} = \frac{A}{z_o} u_a \tag{6.10}$$

and inserting into 6.8 obtain

$$U_{z_2} - U_{z_1} = \frac{Ad}{z_o} u_a. \tag{6.11}$$

The ratio Ad/z_0 is then estimated from the slope of the MCR difference current measurement as a function of the wind speed, shown in figure 6.13. The slope value obtained (also given on the figure and in Table 6.3) is $S = 0.017 \pm 0.006$. Using $d = 1.95$ m, we find for the constant

shear that $A/z_0 = (7.2 \pm 3.1) \times 10^{-3}$ m^{-1}. Due to the form of the linear profile assumption, the roughness length, z_o, is not eliminated from the expression for the current difference (Equation 6.8) as it was for the logarithmic profile case (Equation 6.4). For this reason, it is not possible to perform an analogous analysis to the logarithmic case to determine whether the linear profile assumption leads to better agreement with physical expectations concerning the shear stress above and below the air-sea boundary.

We can, however, use the value for the shear thus obtained, combined with the single frequency results of the comparison between the MCR current measurement and the wind speed (shown in Figure 6.2) to estimate the surface current ($z = 0$) as a fraction of the wind speed. Rewriting 6.7 in terms of the quantity A/z_o, we have

$$U_s = U(z_i) + \frac{A}{z_o} u_a z_i. \tag{6.12}$$

We then substitute, for the current measured at one of the radar measurement depths z_i,

$$U(z_i) = S_i \cdot u_a, \tag{6.13}$$

where S_i is the slope determined from experiment, and write

$$U_s = \left(S_i + \frac{A}{z_0} z_i \right) u_a. \tag{6.14}$$

We have, from the radial current measurement for which we obtained the highest correlation with the wind speed (21.8 MHz results processed using MUSIC) the slope value from Table 6.1, $S_i = 0.033 \pm 0.007$. For the linear profile $z_i = 0.08\lambda = 0.55$ m and combined with the value for A/z_0 obtained above, we use Equation 6.14, to find for the surface drift ($z = 0$),

$U_s = (0.037 \pm 0.0072)u_a$ or about 3.7 % of the wind speed. (We have assumed that errors in slope determination are independent.)

It may be useful to note that, within the uncertainty of the measurement, the current measured at 21.8 MHz ($z = -0.55$ m) is approximately equal to the surface drift ($z = 0$ m). This result for the surface drift velocity is in agreement with the results of Wu (Wu, 1983) who estimated the total surface drift for very large fetches to be 3.1 % of the wind speed and Shemdin (Shemdin, 1972) who estimated the drift at 3 % of the wind speed. Other results are also in agreement, such as the results of Hughes (Hughes, 1956) who measured the drift velocity of floating plastic envelopes and arrived at 3.3 % and observations of the drift of floating oil (Smith, 1968) that indicated 3.4 %. Recent experiments involving MCR current measurements during the Chesapeake outflow plume experiment (COPE-3) have indicated a near-surface current, measured with a 21.8 MHz radar operating frequency, of 1.5 to 2.5 % of the wind speed.

6.6 Conclusion

From multi-frequency HF radar, near-surface radial current measurements averaged over a region of the ocean surface near a flux buoy inside Monterey Bay, comparisons were made with wind and wave measurements. High resolution directional wave spectral energy measurements were used to estimate the expected effect of Stokes drift on the radar measurements, and measurements of the wind speed and direction along with estimates of the friction velocity obtained from three dimensional sonic anemometer measurements were used to inves-

tigate the effect of wind forcing on the near-surface currents. Different radar frequencies and processing methods were examined. Correlations at greater than the 95 % significance level were observed between the averaged radial current measurements and the wind and wave quantities for most of the radar frequencies and processing methods used. The best results using the single frequency radar current measurements came from the highest radar frequency and the MUSIC processing method. This result was in agreement with the results of simulation experiments of chapter 4. The results of the calculation of Stokes drift from the wave measurements were compared with the wind speed. The resulting correlation was found to be significant and approximately equal to the correlations observed between the current measurements and the wind and the current measurements and the expected effect on the radar measurement due to Stokes drift. The magnitude of the Stokes drift current at the surface was found to be about 0.5 % of the wind speed. This result is about a factor of three smaller than that predicted by Kenyon, assuming fully developed seas and a uni-directional spectrum.

Comparisons between the measured surface current and the expected effect due to Stokes drift show a significant correlation, but the magnitude of the Stokes shift as calculated from the directional wave spectral energy measurements obtained during the deployment of the Flux buoy was small enough relative to the surface currents measured by the MCR and correlated with the local wind to a sufficient degree, to make the effects of Stokes drift on the MCR measurements inseparable from the influence of the local wind, given the current state of accuracy of the MCR measurements and the limitations of the data set examined here. Analysis of the data, or the data itself are insufficient to suggest that the observed correlations could not

be due completely to the presence of wind-shear driven currents and the correlation between local wind and the Stokes drift.

Observations using the difference in the radial current measured at the highest and lowest radar frequencies were examined. In spite of the increased relative error in the measurement, significant correlations are again observed between the wind measurements and the current difference, and the predicted effect due to Stokes drift and the current difference measurement. The slope of the linear regression of the radial current difference on the predicted Stokes drift effect indicates that Stokes drift accounts for, at most, about one seventh of the shear in the near-surface region probed by the radar.

Finally, using the results of the current difference measurements along with assumptions on the form of the vertical current profile, we evaluated the agreement with physical expectations on the variation of the shear stress across the air-sea boundary. Results using a logarithmic current profile assumption cast doubt on the validity of the logarithmic vertical profile for near-surface currents in the open ocean. Results obtained assuming a linear vertical current profile did not lend themselves to an analogous analysis but did yield an estimate of the current at the surface as a function of the wind speed from the radar current measurements that was in agreement with the commonly accepted value of 3 % of the wind speed.

Chapter 7

Conclusion

The focus of this work can be separated into two categories; first, the estimation and analysis of errors in data processing algorithms for the extraction of ocean current measurements from HF radar data and second, investigation into the nature of the near-surface ocean current and the functional form of the vertical current profile, its relation to wind and wave forcing and the effect of the the vertical current profile on the depth of the HF radar current measurements.

To begin the investigation of the data processing, a simulation (described in Chapter 4) was created to evaluate the performance of beam forming and MUSIC direction finding algorithms and to estimate the errors in current determination as a function of the sea-state and radar system parameters. This work represents the first comprehensive comparison between beam forming and MUSIC direction finding methods. Errors for both beam forming and MUSIC processing methods as a function of sea state and radar operating parameters are examined.

Errors in MUSIC processed currents (seen in Figures 4.4 and 4.7) from simulated

data led to modifications in the MUSIC algorithm that significantly reduced the errors observed with simulated data, and appeared to improve the performance in experiments involving real data as well. The process of designing the modifications (described in Section 4.5) was guided by analysis of results with simulated data.

Simulation experiments were valuable both for comparing the beam forming and MUSIC data processing algorithms and for estimating the magnitude of errors. The results in Figure 4.9 indicate that errors with beam forming have a greater dependence on SNR than MUSIC processed results and increase rapidly for a SNR of less than 15 dB. Errors in MUSIC results are seen to be flat with respect to SNR from about 10 to 20 dB for all four of the MCR frequencies of operation. With the exception of the lowest radar frequency, the results for the case of a uniform current parallel to shore indicate similar performance from the two algorithms above about 25 dB SNR. The errors are seen to increase with a decrease in radar operating frequency and to fall between about 2 to 5 cm/s depending on frequency. For the lowest radar frequency, the error is seen to be greater by about a factor of two for the MUSIC processed data. Errors with beam forming, as indicated by Figure 4.10, are more systematic in nature and errors with MUSIC, more random in nature.

In Section 4.6.4 it is seen that the degree of sharpness in changes in the radial current component as a function of radar look angle and the frequency dependent angular resolution of the radar measurements are in a sense equivalent in terms of their effect on errors in the current measurements. The simulation was used to evaluate the error as a function of a combination of these parameters and in so doing characterize a wide range of the parameter space pertinent

to errors in HF radar measurements. The results show that MUSIC performs better than beam forming over most of the operating frequency and current profile sharpness space probed.

Overall the results of simulation comparisons indicate that MUSIC is a good alternative to beam forming for all four of the MCR's operating frequencies. The only situation where beam forming clearly performed better than MUSIC was for cases where both of the following conditions are met: 1. a smooth radial current profile where the systematic errors due to averaging over a large beam width are small, and 2. the lowest operating frequency where random errors with MUSIC are apparently about a factor of two larger than errors with beam forming.

The experiments involving real data used data from the MCR radar deployed at Long Marine Lab in Santa Cruz, from the time period of September 3, 1999 to November 11, 1999. Because of equipment problems with the MCR deployment site at Moss Landing, full vector current measurements were not available. The time period of interest overlapped the NPS deployment of a flux buoy capable of three dimensional wind turbulence measurements and high resolution directional wave energy measurements. Additionally, both ADCP and standard meteorological data were available, during the time period of interest, from the MBARI buoy, M1.

Chapter 5 involves radar-derived measurements of near-surface ocean currents from a region of the ocean surface located at a range of about 21 km along a radial nearly perpendicular to the shore. This region corresponded to the location of the MBARI buoy, M1. Radar-derived current measurements obtained using different frequencies and processing methods are compared in order to evaluate the performance of the beam forming and MUSIC algorithms over

the range of MCR operating frequencies and derive estimates of uncertainties in the measurements. Similar comparisons are made between the radar-derived current measurements and the current measurements from the top bin of the ADCP.

In Section 5.2.1, current measurements at each of the four MCR frequencies are compared in order to estimate the RMS errors in the measurements as a function of the radar operating frequency. As with the simulation results, the error estimates (Table 5.2) show an increase in error with decrease in radar frequency. Error estimates range from 1.5 to 5.6 cm/s depending on radar frequency and processing method. The error estimates, as deduced by this method, are lower for beam forming than for MUSIC. The slope of the inter-frequency comparisons in the beam formed results decreased with frequency faster than for the MUSIC results. This indicates that part of the decrease in slope with radar frequency seen with beam forming is not due to a real decrease in current magnitude with measurement depth, but rather due to the increased beam width. Averaging MUSIC processed current measurements spatially to simulate the effect of averaging over beam width corresponding to the given frequency caused the results with MUSIC to approach the beam formed results.

The comparisons between beam forming and MUSIC processing in Figure 5.7 show that the two methods produce very similar results for the highest two radar frequencies but that the similarity decreases with the frequency and that, for the lower two frequencies, the measured current magnitude is, in general, greater with MUSIC processed results. Error estimates from comparing processing methods range from about 2 to 5 cm/s for the highest to lowest radar operating frequencies, respectively.

Error estimates from comparisons with ADCP measurements (Table 5.4) range from about 6 to 8 cm/s and do not show a clear increase in error with a decrease in frequency. The error estimates are higher with MUSIC but the correlation coefficients between the MUSIC processed results and the correlated component of the ADCP measurements are also higher, ranging from 0.70 to 0.74.

Chapter 6 involves radar-derived measurements of the ocean current from a patch of ocean surface located at a range of about 21 km and at an angle of about 40° counter clockwise relative to the direction perpendicular to the shore. This location corresponded to the location of the NPS flux buoy.

Section 6.2 compares the MCR current measurements with the wind speed, wind speed squared and direct estimates of the wind friction velocity. For most of the comparisons, the correlations are greater than the 95 % significance levels. The highest correlations are found with the results of MUSIC processing.

The effect of Stokes drift on the phase speed of the Bragg resonant ocean waves, and hence, the radar-derived current measurements, is examined in Section 2.3. We take the approach that the net currents due to Stokes drift, arising from all of the waves present on the ocean surface, can be treated, in terms of their effect on HF radar current measurements, in the same manner as currents from any other source. With this assumption, we show that a modification to the phase speed of a given wave-train can be calculated given the directional wave energy spectrum and that this modification is in agreement (within a factor of two) with the modification to the dispersion relation for deep water gravity waves predicted by Weber and

Barrick from basic principles using a perturbation approach.

In Section 2.4 we examine a theoretical model for the vertical current profile and, in Section 2.6, the corresponding effective depth of the radar-derived current measurements. We consider both the most commonly accepted form of the vertical current profile, the logarithmic profile, and a profile that is dominated by wave-induced currents (Stokes drift) from an ideal wind-wave spectrum. This investigation represents the first estimation of the effective depth of the radar-derived current measurement based on a Stokes drift dominated vertical current profile, a situation that has been suggested to be the case for the open ocean or where the fetch is effectively infinite. In contrast to the results for the logarithmic and linear profile assumptions where the depth of the radar-derived current measurement depends only on the radar wavelength, we find that, in the case of a Stokes drift dominated current profile, the effective depth of the measurement depends on the wave energy spectrum as well.

In Section 6.3 we estimate the effect of the Stokes drift currents on the MCR current measurements based on the high resolution directional wave energy spectra recorded by the NPS flux buoy. Over the buoy deployment period, the predicted RMS shift in the radar-derived current measurements due to Stokes drift was 1.6 cm/s for the highest radar frequency. This is roughly equal to the estimated RMS error in the current measurements. For the lower radar frequencies, the predicted Stokes drift effect decreases and the RMS error in the radar measurements increases. These results imply that the predicted Stokes drift effect is not significant for the data we recorded. Figure 6.8 indicates that even in cases where the energy in the wave spectrum is dominated by the lower frequencies, the Stokes drift is dominated by the

high frequencies and therefore expected to be correlated with the local wind. This prediction is supported by the high correlation in Figure 6.11 between the measured wind speed and the predicted Stokes drift. Figure 6.11 also gives an estimate of the Stokes drift at the surface as a function of the wind speed. The value obtained, 0.50 % of the wind speed, is lower than expected for fully developed seas.

The correlations found in the comparison between the MCR measurements and the predicted effect due to Stokes drift (in Figure 6.9) were, on average, lower than the correlations seen between the MCR current measurements and the wind parameters and lower than the correlation found between the Stokes drift and the wind. This result coupled with small magnitude of the predicted Stokes drift effect relative to the estimates of the error in the MCR measurements indicate that it is unlikely that, through analysis of this data set, the Stokes drift effect can be distinguished from the wind. Figure 6.10 indicates that the currents measured by the MCR do show an increasing trend with an increase in the predicted Stokes drift effect, but the MCR currents were from 5 to almost 20 times larger than the expected result due to Stokes drift currents alone. The possibility that the observed currents were due purely to wind forcing cannot be ruled out here.

In Section 6.5, current difference measurements using the highest and lowest radar frequencies are examined. The results show correlations with the wind speed, the wind speed squared, the wind friction velocity and the expected difference due to Stokes drift. The correlation coefficients are surprisingly high considering the increase in error and decrease in signal due to taking the difference. Analysis of the current difference measurements, along with the

assumption of a logarithmic vertical current profile, enabled estimation of the ratio of the shear stress above and below the air-sea interface. Results are not consistent with the physical expectations and may be an indication that the logarithmic form does not describe the near-surface vertical current profile in the open ocean. With the assumption of a linear vertical current profile, current difference measurements are not applicable to a similar analysis, without knowledge of the appropriate value of the roughness length, but do provide a means to estimate the wind-defendant surface current. A surface drift of 3.7 ± 0.8 % of the wind speed is estimated from the radar-derived ocean current measurements, in agreement with the commonly accepted value of roughly 3 % of the wind speed.

Overall, through analysis of simulation experiments and experiments using real data, this work improves our understanding of the application of MUSIC to HF radar current measurement and the relative performance of the MUSIC and beam forming algorithms. It provides estimates of the magnitude of the uncertainties in the measurements and their dependence on sea-state parameters. Results indicate that MUSIC may be an improvement over beam forming, particularly in multi-frequency or other aperture-limited situations, and for the MCR system, using MUSIC improves the angular resolution of the lower frequency measurements and thereby improves the capability to obtain information about the near-surface dynamics through analysis of multi-frequency measurements of the ocean currents.

Though HF radar investigations into the properties of the ocean surface go back to Crombie's observations in the 1950's, radar systems are still under development and improving. Most continuous data sets are rather short and errors and limitations are still not well understood.

Future study involving the nature of HF radar measurements will continue to be important to understanding the capabilities and limitations of the measurements. Some areas for future work include:

1. Repeat some of the experiments discussed here with full vector radar-derived current measurements. In particular, the analysis of the angles between the radar measured currents and the other measured quantities (wind stress, Stokes current and ADCP measured currents) was hampered by the lack of full vector radar-derived current data. Analysis of these angles may turn out to be a way to separate the wind-induced currents from the Stokes currents.

2. Expand experiments to longer time series. Correlations seen here between successive points in the Stokes drift current time series indicate the need for longer data sets, particularly for investigations involving Stokes drift.

3. Investigate the current profile in more detail, in particular the effects of wave breaking may be important. It would be interesting to look for an indication in the radar-derived currents of a transition associated with the onset of white-capping over Monterey Bay, and examine the possibility that the form of the current profile is affected by that transition.

4. Future multi-frequency HF radar experiments would benefit from using longer sampling periods for the lower frequency measurements. Investigations into the use of MUSIC processing here have made it apparent that the limitation that each radar frequency be sampled for the same length of time is not optimal.

5. Use simulations to investigate further improvements to the MUSIC algorithm. Simulation experiments could also be used to evaluate the performance of different antenna

geometries, combinations of beam forming and direction finding and other direction finding algorithms.

Bibliography

Barrick, D. E. 1972a, *IEEE Trans. Antennas Propag.*, **AP-20**, 2

Barrick, D. E. 1972b, in *Remote sensing of the Troposphere*, NOAA/Enviromental Research Laboratories, Boulder, Co

Barrick, D. E. 1986, *Journal of Oceanic Engineering*, **OE-11, NO. 2**, 286

Barrick, D. E., Evans, M. W., & Weber, B. L. 1977, *Science*, **198**, 138

Barrick, D. E., Headrick, J. M., Bogle, R. W., & Crombie, D. D. 1974, *Proc. IEEE*, **62**, 673

Barrick, D. E. & Lipa, B. J. 1996, *A Comparison of Direction-Finding and Beam-Forming in HF Radar Ocean Surface Current Mapping*, Phase 1 SBIR final report, unpublished, Codar Ocean Sensors, 1000 Fremont Avenue, Suite K Los Altos, Ca 94024

Barrick, D. E. & Lipa, B. J. 1997, *Oceanography*, **10 NO. 2**, 72

Barrick, D. E. & Snider, J. B. 1977, *IEEE Transactions on Antennas and Propagation*, **AP-25, NO. 1**, 19

Barrick, D. E. & Weber, B. L. 1977, *Journal of Physical Oceanography*, **7, NO. 1**, 11

Bowditch, N. 1982, *Waves, Winds and Weather*, David McKay Co.

Charnock, H. 1955, *Quart. J. Roy. Meteor. Soc.*, **81**, 639

Cheung, T. K. & Street, R. L. 1988, *Journal of Fluid Mechanics*, **194**, 133

Craig, P. D. 1996, *Journal of Geophysical Research*, **101 NO.C1**, 1265

Craig, P. D. & Banner, M. L. 1994, *Journal of Physical Oceanography*, **24**, 2546

Crombie, D. D. 1955, *Nature*, **175**, 681

Emery, W. J. & Thomson, R. E. 1997, *Data Analysis Methods in Physical Oceanography*, Pergamon

Fernandez, D. M. 1993, *Ph.D. thesis*, Stanford Univ., Stanford, Calif.

Fernandez, D. M. 1997, *The Oceanography Scociety*, **10(2)**, 93

Fernandez, D. M., Meadows, L. A., Vesecy, J. F., Teague, C. C., Paduan, J. D., & Hanson, P. 1999, *Journal of Oeanic Engineering*, 25

Fernandez, D. M., Vesecky, J. F., & Teague, C. C. 1996, *Journal of Geophysical Research*, **101**, 28615

Frederickson, P. A., Davidson, K. L., Jones, K., & Neta, T. 2000, *Flux Buoy Data Report ICON September - November 1999 Deployment, Monterey Bay, California*, Unpublished, Boundary Layer Studies Group, Department of Meteorology Naval Postgraduate School, Monterey, Ca

Graber, H. C., Haus, B. K., Chapman, R. D., & Shay, L. K. 1997, *Journal of Geophysical Research*, **102**, 18749

Ha, E. C. 1979, *Ph.D. thesis*, Stanford Univ., Stanford, Calif., Tech. Rep. D415-1

Hughes, P. 1956, *Quart. J. Roy. Meteor. Soc.*, **82**, 494

Kenyon, K. E. 1969, *Journal of Geophysical Research*, **74**, 6991

Kitaigorodskii, S. A., Donelan, M. A., Lumley, J. L., & Terray, E. A. 1983, *Journal of Physical Oceanography*, **13**, 1988

Kraus, E. B. & Businger, J. A. 1994, *Atmosphere-Ocean Interaction*, Oxford University Press, Inc.

Laws, K. E., Fernandez, D. M., & Paduan, J. D. 2000, *Journal of Oceanic Engineering*, **25(4)**, 481

Lipa, B. J. 1978, *Journal of Geophysical Research*, **83**, 959

Longuet-Higgins, M. S., Cartwright, D. E., & Smith, N. D. 1963, in *Ocean Wave Spectra*, pp 111–136, Prentice-Hall, Englewood Cliffs, NJ

Longuet-Higgins, M. S. & Phillips, O. M. 1962, *Journal of Fluid Mechanics*, **12**, 333

Melton, D. C. 1995, *Master's thesis*, Naval Postgraduate School, Monterey, Calif.

Paduan, J. D. & Cook, Michael, S. 1996, *The Oceanography Scociety*, **10(2)**, 49

Paduan, J. D. & Rosenfeld, Leslie, K. 1996, *Journal of Geophysical Research*, **101(C9)**, 20,669

Pierson, W. J. & Moskowitz, L. 1964, *Journal of Geophysical Research*, **69(24)**, 5181

Schmidt, R. O. 1981, *Ph.D. thesis*, Stanford University

Schmidt, R. O. 1986, *IEEE Trans. on Antennas and Propagation*, **AP-34**, 276

Shemdin, O. H. 1972, *Journal of Physical Oceanography*, **2**, 411

Smith, J. E. 1968, *"Torrey Canyon" Pollution and Marine Life*, Cambridge University Press

Stewart, R. H. & Joy, J. W. 1974, *Deep-Sea Research*, **21**, 1039

Stokes, G. G. 1847, *Trans. Cambridge Phil. Soc.*, **8**, 441

Teague, C. C. 1986, *Journal of Oceanic Engineering*, **OE-11(2)**, 258

Teague, C. C., Vesecky, J. F., & Hallock, Z. R. 2001, *A comparison of Multifrequency HF Radar and ADCP measurements of near-surface currents during COPE-3*, Accepted for publication in the Journal of Oceanic Engineering

The Oceanography Society 1997, *Oceanography*, **10**(**2**), Special Issue on High Frequency Radars for Coastal Oceanograpy

Tyler, G. L., Teague, C. C., Stewart, R. H., Peterson, A. M., Munk, W. H., & Joy, J. W. 1974, *Deep Sea Research*, **21**, 989

Weber, B. L. & Barrick, D. E. 1977, *Journal of Physical Oceanography*, **7, NO. 1**, 3

Wu, J. 1975, *Journal of Fluid Mechanics*, **68**, 49

Wu, J. 1983, *Journal of Physical Oceanography*, **13**, 1441

Wyatt, L. R. 1997, *The Oceanography Scociety*, **10(2)**, 85